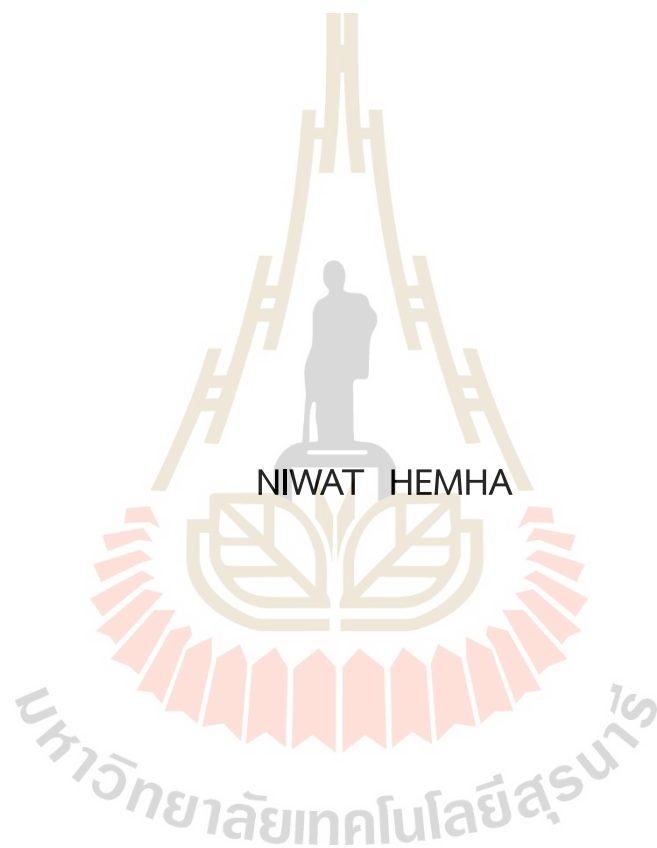


FABRICATION OF CARBON-BASED NANOCOMPOSITE
SUPERCAPACITOR ELECTRODES BY PNEUMATIC DISPENSING
3D PRINTING



A Thesis Submitted in Partial Fulfillment of the Requirements for the
Degree of Doctor of Philosophy in Physics
Suranaree University of Technology
Academic Year 2022

การทำขั้วตัวเก็บประจุไฟฟ้าเคมียิ่งยวดจากวัสดุคาร์บอนนาโนคอมโพสิต
โดยวิธีการพิมพ์สามมิติแบบนิวแมติก



วิทยานิพนธ์นี้เป็นส่วนหนึ่งของการศึกษาตามหลักสูตรปริญญาวิทยาศาสตรดุษฎีบัณฑิต
สาขาวิชาฟิสิกส์
มหาวิทยาลัยเทคโนโลยีสุรนารี
ปีการศึกษา 2565

FABRICATION OF CARBON-BASED NANOCOMPOSITE SUPERCAPACITOR
ELECTRODES BY PNEUMATIC DISPENSING 3D PRINTING

Suranaree University of Technology has approved this thesis submitted in
partial fulfillment of the requirements for the Degree of Doctor of Philosophy.

Thesis Examining Committee



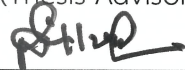
(Dr. Adisorn Tuantranont)

Chairperson




(Dr. Wiwat Nuansing)

Member (Thesis Advisor)



(Prof. Dr. Santi Maensiri)

Member



(Assoc. Prof. Dr. Panomsak Meemon)

Member



(Asst. Prof. Dr. Wittawat Saenrang)

Member



(Assoc. Prof. Dr. Yupaporn Raksakulpiwat)

Vice Rector for Academic Affairs
and Quality Assurance



(Prof. Dr. Santi Maensiri)

Dean of Institute of Science

นิวัฒน์ เหมหา : การทำขั้วตัวเก็บประจุไฟฟ้าเคมียิ่งยวดจากวัสดุคาร์บอนนาโนคอมโพสิต
โดยวิธีการพิมพ์สามมิติแบบนิวแมติก (FABRICATION OF CARBON-BASED
NANOCOMPOSITE SUPERCAPACITOR ELECTRODES BY PNEUMATIC DISPENSING
3D PRINTING) อาจารย์ที่ปรึกษา : อาจารย์ ดร.วิวัฒน์ นวลสิงห์, 161 หน้า

คำสำคัญ: การกักเก็บพลังงาน/ขั้วตัวเก็บประจุไฟฟ้าเคมียิ่งยวด/การพิมพ์สามมิติ/การฉีควัสดุ
โดยตรง/นาโนคอมโพสิต

ในปัจจุบันมีความต้องการใช้พลังงานไฟฟ้าสูงมากขึ้น เนื่องจากการพัฒนาเทคโนโลยีดิจิทัล
และประชากรของโลกที่เพิ่มจำนวนขึ้น ส่งผลให้แหล่งพลังงานที่มีอยู่อย่างจำกัด เช่น ถ่านหิน น้ำมัน
และก๊าซธรรมชาติ ลดลงตามไปด้วย อีกทั้งแหล่งพลังงานจากฟอสซิลเหล่านี้ยังส่งผลกระทบต่อสภาวะ
โลกร้อน ดังนั้นเพื่อเป็นการแก้ไขปัญหาดังกล่าว แหล่งพลังงานสะอาด เช่น พลังงานแสงอาทิตย์ และ
พลังงานลม จึงได้รับความสนใจมากขึ้น อย่างไรก็ตามพลังงานสะอาดเหล่านี้สามารถผลิตได้แค่บาง
ช่วงเวลา ดังนั้นการกักเก็บพลังงานจึงเข้ามามีบทบาทสำคัญ ซึ่งตัวเก็บประจุไฟฟ้าเคมียิ่งยวดนั้น
สามารถตอบโจทย์ความต้องการนี้ได้ เนื่องจากสมบัติการอัดและคายประจุที่รวดเร็ว แต่การผลิตตัว
เก็บประจุไฟฟ้าเคมียิ่งยวดให้มีประสิทธิภาพสูงยังมีข้อจำกัด เช่น ความหนาแน่นพลังงานที่ยังต่ำเมื่อ
เทียบกับแบตเตอรี่ ดังนั้นจึงเริ่มมีการพัฒนาขั้วตัวเก็บประจุไฟฟ้าเคมียิ่งยวดให้มีพื้นที่ผิวมากขึ้นโดย
การขึ้นรูปขั้วแบบสามมิติ เพื่อเป็นแนวทางการเพิ่มประสิทธิภาพของขั้วแบบเดิมที่มีลักษณะเป็นฟิล์ม
แบบสองมิติ

ในงานวิจัยนี้ได้พัฒนาระบบการพิมพ์สามมิติแบบนิวแมติกด้วยเทคนิคการฉีควัสดุโดยตรง
(direct ink writing, DIW) เพื่อใช้ในการขึ้นรูปขั้วตัวเก็บประจุแบบสามมิติ หมึกพิมพ์ที่ใช้ในงานวิจัยนี้
ผลิตขึ้นโดยผสมวัสดุคาร์บอนนาโนคอมโพสิต เช่น รีดิวซ์กราฟีนออกไซด์ (reduced graphene
oxide, rGO) เข้ากับวัสดุประสานในกลุ่มเซลลูโลส (cellulose) จากการทดลองพบว่า ชิ้นงานที่พิมพ์
ได้มีขนาดและรูปร่างตามที่ออกแบบไว้ แต่เมื่อชิ้นงานแห้งตัวแล้วจะมีขนาดลดลงประมาณ 25%
ดังนั้นการออกแบบชิ้นงานจะต้องคำนึงถึงค่าการหดตัวนี้ด้วย ทั้งนี้ยังได้ทดลองพิมพ์ชิ้นงานให้มีความ
หนาแตกต่างกันเพื่อศึกษาปัจจัยความหนาของขั้วไฟฟ้ากับค่าเก็บประจุจำเพาะเชิงผิว (areal
capacitance) ทั้งนี้ขั้วไฟฟ้ายังผ่านกระบวนการชุบด้วยพอลิอะนิลีน (polyaniline, PANI) ซึ่งเป็น
พอลิเมอร์ที่นำไฟฟ้า เพื่อช่วยให้ขั้วไฟฟ้ามีสมบัติการเป็นวัสดุตัวเก็บประจุแฝง (pseudocapacitive
material) วัสดุที่สังเคราะห์ขึ้นถูกนำไปวิเคราะห์สมบัติทางกายภาพโดยใช้เทคนิคการเลี้ยวเบนของ
รังสีเอ็กซ์ (X-ray diffraction, XRD) และกล้องจุลทรรศน์แบบส่องกราด (Scanning electron
microscope, SEM) นอกจากนี้ ตัวอย่างงานที่เตรียมขึ้นมาได้ถูกนำไปศึกษาคุณสมบัติเชิงเคมีไฟฟ้า

โดยใช้เทคนิคไซคลิกโวลแทมเมตรี (cyclic voltammetry, CV) การอัดและคายประจุด้วยกระแสคงที่ (galvano charge/discharge, GCD) และเทคนิคอิมพีแดนซ์สเปกโทรสโกปี (electrochemical impedance spectroscopy, EIS)

จากการทดลองพบว่าพอลิอะนิลีนที่สังเคราะห์ขึ้นมีรูปร่างเป็นโครงข่ายเส้นใยนาโนขนาดเส้นผ่านศูนย์กลาง 46.66 ± 5.50 นาโนเมตร และผลวิเคราะห์จากเทคนิค XRD สามารถระบุโครงสร้างผลึกของความเป็นพอลิอะนิลีน นอกจากนี้ สมบัติเคมีเชิงไฟฟ้าของขั้วที่ประดิษฐ์ขึ้น ได้ผ่านการศึกษาโดยทดสอบในสารละลายอิเล็กโทรไลต์โพแทสเซียมไฮดรอกไซด์ (potassium hydroxide, KOH) ความเข้มข้น 3 โมลาร์ โดยใช้ระบบสามขั้วไฟฟ้าพบว่า ปัจจัยการเพิ่มความหนาของขั้วไฟฟ้าสามมิติที่ยังไม่ชุบพอลิอะนิลีนมีผลโดยตรงต่อค่าความจุไฟฟ้าจำเพาะเชิงผิว โดยหากขั้วไฟฟ้ามีความหนามากขึ้นจะทำให้ค่าความจุไฟฟ้าสูงขึ้นเนื่องจากการเพิ่มขึ้นของพื้นผิวของขั้วไฟฟ้า แต่ในการทดลองที่ขั้วไฟฟ้าผ่านการชุบพอลิอะนิลีนพบว่า ค่าความจุไฟฟ้าจำเพาะเชิงผิวมีแนวโน้มลดลงตามจำนวนครั้งของการชุบ ซึ่งอาจมีสาเหตุจากการมีช่องว่างเกิดขึ้นระหว่างผิวของขั้วไฟฟ้าที่เป็นวัสดุคาร์บอนกับชั้นแรกของพอลิอะนิลีน ส่งผลกระทบต่อเนื่องถึงความต้านทานที่เพิ่มขึ้น และทำให้ค่าความจุไฟฟ้าจำเพาะเชิงผิวลดลง โดยค่าความจุไฟฟ้าจำเพาะเชิงผิวที่วัดได้สูงสุดในงานวิจัยนี้เท่ากับ 84.32 mF/cm^2 ที่ความหนาแน่นของกระแส 1 mA/cm^2 และมีความหนาแน่นของพลังงาน (energy density) เท่ากับ $19.79 \text{ } \mu\text{Wh/cm}^2$ และความหนาแน่นของกำลัง (power density) เท่ากับ $672.81 \text{ } \mu\text{W/cm}^2$ ซึ่งถือว่ามีความมากกว่าขั้วไฟฟ้าแบบสองมิติ และใกล้เคียงกับแบบสามมิติของกลุ่มวิจัยอื่น

จากผลการวิจัยนี้ทำให้ค้นพบและเกิดองค์ความรู้ว่า การเพิ่มขึ้นของพื้นผิวของขั้วไฟฟ้าตัวเก็บประจุยิ่งยวดสามมิตินั้น มีผลโดยตรงกับค่าความจุไฟฟ้าจำเพาะเชิงผิว แต่หากมีการชุบด้วยพอลิอะนิลีนจะส่งผลให้ค่าความจุไฟฟ้าจำเพาะเชิงผิวลดลง เนื่องจากมีช่องว่างเกิดขึ้นระหว่างชั้นรอยต่อของวัสดุคาร์บอนและชั้นพอลิอะนิลีน ซึ่งการค้นพบนี้ทำให้ได้แนวทางในการพัฒนางานวิจัยในลำดับถัดไป นอกจากนี้เครื่องพิมพ์สามมิติแบบนิวเมติกที่ถูกประดิษฐ์ขึ้นยังสามารถประยุกต์ใช้กับการพิมพ์สามมิติในวัสดุกลุ่มอื่นได้ เช่น วัสดุชีวภาพ (3D Bioprinting) อาหาร (Food 3D printing) และวัสดุเซรามิก (Ceramic 3D printing) ซึ่งจะทำให้สามารถขยายขอบเขตการประยุกต์ใช้ได้หลากหลายมากยิ่งขึ้น

สาขาวิชาฟิสิกส์

ปีการศึกษา 2565

ลายมือชื่อนักศึกษา

พิชญ์พงศ์ เขตตา

ลายมือชื่ออาจารย์ที่ปรึกษา

วิวัฒน์ ๒๐

NIWAT HEMHA: FABRICATION OF CARBON-BASED NANOCOMPOSITE
SUPERCAPACITOR ELECTRODES BY PNEUMATIC DISPENSING 3D PRINTING
THESIS ADVISOR : WIWAT NUANSING, Ph.D. 161 PP.

Keyword: energy storage/supercapacitor electrode/3D printing/direct ink writing/
nanocomposite

Currently, there is an increasing demand for energy due to the advancements in digital technologies. Additionally, the global population continues to grow each year, leading to the depletion of finite energy sources such as coal, oil, and natural gas. Moreover, these fossil energy sources are the dominant cause of global warming. As a result, clean energy sources have garnered more attention as a solution to these challenges. However, clean energy sources such as solar and wind power are only available during specific periods, such as daylight for solar energy. Therefore, energy storage has become crucial to prevent energy wastage and enable availability at different times. Supercapacitors have emerged as a promising solution for energy storage. Unlike batteries that store energy chemically, supercapacitors store energy electrostatically, allowing for rapid charging and discharging, making them ideal for high-power applications. Therefore, developing the supercapacitor with a more intricate and highly porous structure, resulting in an increased surface area, is an approach that helps enhance the efficiency of the energy storage device.

In this research, a 3D printing system utilizing the direct ink writing (DIW) technique was developed to fabricate 3D supercapacitor electrodes. The ink was prepared by mixing of carbon-based material such as reduced graphene oxide (rGO) and cellulose-based materials under appropriate conditions. Printing results show that the 3D printed electrodes underwent a 25% shrinkage. Consequently, the design of the objects incorporated considerations for the shrinkage factor. The fabricated samples were characterized using X-ray diffraction (XRD) and scanning electron microscopy (SEM) to examine physical properties. In addition, their electrochemical properties were evaluated

through cyclic voltammetry (CV), galvanostatic charge-discharge (GCD), and electrochemical impedance spectroscopy (EIS).

The results revealed that the synthesized polyaniline-coated on rGO had fibrous nanostructure with an average diameter of 46.66 ± 5.50 nm. The XRD measurement confirmed the crystalline structure of polyaniline. The electrochemical characterization of the printed electrodes in a potassium hydroxide (KOH) electrolyte with a concentration of 3 M, using a 3 electrodes system, demonstrated that the increasing thickness of the 3D electrodes without polyaniline coating directly influenced the specific areal capacitance. This increase was attributed to the expanded surface area of the electrodes. However, the polyaniline-coated electrodes exhibited a decrease in specific areal capacitance with an increasing number of coating layers. This phenomenon was attributed to the formation of gaps between the electrode surface and polyaniline in the initial coating layers, resulting in increased resistance and reduced the specific areal capacitance. The maximum specific areal capacitance measured in this study was 84.32 mF/cm^2 at a current density of 1 mA/cm^2 , with an energy density of $19.79 \text{ } \mu\text{Wh/cm}^2$ and a power density of $672.81 \text{ } \mu\text{W/cm}^2$, which are found to be higher than that of 2D electrodes and comparable to the 3D electrodes reported by other research groups.

The study indicated that increasing the surface area of the 3D electrode directly impacted the specific areal capacitance. Although the polyaniline coating led to a decrease in specific areal capacitance, this study provided valuable insights into the causes and would serve as a topic for further research. Moreover, the pneumatic 3D printer developed in this study holds potential for broader applications in various research areas, including 3D bioprinting, food 3D printing, and ceramic 3D printing, thereby expanding its versatility and potential impact.

School of Physics
Academic Year 2022

Student's Signature นิวัฒน์ เสงี่ยม
Advisor's Signature ดร. ชวณัฐ

ACKNOWLEDGEMENTS

This research would not have been successful without the help and support of everyone involved. Firstly, I would like to express my gratitude to my advisor, Dr. Wiwat Nuansing, for providing the opportunity to collaborate on this research and for guiding me throughout the project. Apart from the research work, Dr. Wiwat has been a source of motivation and support in various aspects of life. Additionally, I would like to thank the Science Achievement Scholarship of Thailand (SAST), the SUT-NANOTEC RNN, and SUT-Research Unit in Advanced Nanomaterials for their financial support towards my education.

I would also like to extend my thanks to the examination committee members, namely Prof. Dr. Santi Maensiri, Dr. Adisorn Tuantranont, Assoc. Prof. Dr. Panomsak Meemon, Asst. Prof. Dr. Wittawat Saenrang, and Dr. Wiwat Nuansing, for their guidance and valuable comments on this research. Furthermore, I am grateful to all the members of the AMP Lab who have supported and assisted me throughout this research, providing a warm and encouraging environment. I would like to thank Dr. Adisorn Tuantranont for allowing me to participate in a short-term research project at the National Security and Dual-Use Technology Center, NSTDA.

Lastly, I want to express my deepest gratitude to my family, especially my parents, for their unwavering support and encouragement throughout my life. Without them, pursuing a Ph.D. would not have been possible.

Niwat Hemha

CONTENTS

	Page
ABSTRACT IN THAI	I
ABSTRACT IN ENGLISH	III
ACKNOWLEDGEMENTS	V
CONTENTS	VI
LIST OF TABLES	XI
LIST OF FIGURES	XIII
LIST OF ABBREVIATIONS.....	XXII
CHAPTER	
I INTRODUCTION	1
1.1 Introduction and motivation	1
1.2 Research objectives	4
1.3 Scope and limitations of the study	5
1.4 Location of research	5
1.5 Instrumentation	6
1.6 Expected Output / Outcome	6
1.7 Overview of the research thesis	7
II LITERATURE REVIEW.....	8
2.1 Electrochemical capacitor	9
2.1.1 Electrochemical double layer capacitor (EDLC)	10
2.1.2 Pseudocapacitor	13
2.1.3 Asymmetric supercapacitor	15
2.2 Polyaniline (PANI)	16
2.2.1 The properties of polyaniline	16
2.2.2 Synthesis of PANI	17
2.3 3D printing development for supercapacitor	19

CONTENTS (Continued)

		Page
	2.3.1 The classification of Additive Manufacturing Technologies.....	23
	2.3.2 The fabrication of convention and 3D printing of supercapacitor electrode.....	31
	2.4 3D printing of supercapacitor electrode.....	34
	2.5 Electrochemical measurements.....	37
	2.5.1 Cyclic voltammetry (CV)	38
	2.5.2 Galvanostatic charge/discharge testing (GCD)	39
	2.5.3 Electrochemical impedance spectroscopy (EIS)	40
	2.6 Summary	42
III	METHODOLOGY.....	44
	3.1 3D printing development	44
	3.1.1 3D printer components	46
	3.1.2 General materials of building 3D printer	54
	3.1.3 The electronic wiring	56
	3.1.4 Firmware configuration	56
	3.1.5 The print accuracy testing	60
	3.1.6 The extruder development	61
	3.1.6.1 The extruder selection.....	63
	3.1.6.1.1 Pneumatic	63
	3.1.6.1.2 Piston-driven	64
	3.1.6.1.3 Screw-driven.....	65
	3.2 High viscous ink 3D-printed electrodes preparation.....	66
	3.2.1 Ink design	67
	3.2.1.1 Methyl cellulose (MC)	67
	3.2.1.2 Cellulose acetate.....	72
	3.3 3D-printed supercapacitor electrode	74

CONTENTS (Continued)

	Page
3.3.1 The ink preparation and printing	76
3.4 Polyaniline (PANI) synthesis and coating	77
3.4.1 Polyaniline synthesis.....	78
3.4.2 Polyaniline coating.....	79
3.5 Material characterization	80
3.5.1 X-ray diffraction (XRD)	80
3.5.2 Scanning electron microscopy (SEM)	81
3.6 Electrochemical properties measurement	81
3.6.1 Electrode preparation.....	81
3.6.2 Electrolyte preparation.....	81
3.6.3 Electrode setup	82
3.6.4 Cyclic voltammetry.....	83
3.6.5 Galvanostatic charge/discharge	84
3.6.6 Electrochemical impedance spectroscopy.....	84
IV METHODOLOGY.....	85
4.1 Developing a 3D printer for the fabrication of supercapacitor electrodes.....	85
4.1.1 3D printer.....	85
4.1.2 The extruder development system.....	86
4.1.3 Discussion	92
4.1.4 Summary.....	92
4.2 Studying and preparing high-viscosity ink for 3D-printed electrodes	92
4.2.1 Discussion	94
4.2.2 Summary.....	95
4.3 Investigating the printing parameters of 3D-printed supercapacitor electrodes.....	96

CONTENTS (Continued)

	Page
4.3.1 Discussion	101
4.3.2 Summary.....	101
4.4 Synthesizing and coating PANI on 3D-printed supercapacitor electrodes.....	102
4.4.1 X-ray diffraction (XRD) of polyaniline (PANI)	104
4.4.2 Scanning electron microscope (SEM) of polyaniline (PANI)	105
4.4.3 Discussion	111
4.4.4 Summary.....	111
4.5 Studying the electrochemical properties of 3D-printed supercapacitor electrodes.....	112
4.5.1 3D-printed rGO supercapacitor electrode at fixed electrolyte soaking time.....	112
4.5.1.1 Cyclic voltammetry measurement	112
4.5.1.2 Galvanostatic charge-discharge measurement	115
4.5.1.3 Electrochemical impedance spectroscopy Measurement	117
4.5.1.4 Discussion.....	118
4.5.1.5 Summary.....	118
4.5.2 3D-printed rGO supercapacitor electrode with vary electrolyte soaking time.....	119
4.5.2.1 Cyclic voltammetry measurement	119
4.5.2.2 Galvanostatic charge-discharge measurement	120
4.5.2.3 Electrochemical impedance spectroscopy Measurement	122
4.5.2.4 Discussion.....	123
4.5.2.5 Summary.....	124

CONTENTS (Continued)

	Page
4.5.3 PANI deposition on rGO 3D-printed supercapacitor Electrode.....	124
4.5.3.1 Maintain a consistent PANI deposition cycle and experiment with different electrode thicknesses.....	124
4.5.3.1.1 Cyclic voltammetry measurement.....	124
4.5.3.1.2 Galvanostatic charge-discharge measurement.....	126
4.5.3.1.3 Electrochemical impedance spectroscopy (EIS) measurement.....	127
4.5.3.1.4 Discussion.....	129
4.5.3.1.5 Summary	129
4.5.3.2 Maintain a consistent electrode thickness and experiment with different PANI deposition cycle.....	129
4.5.3.2.1 Cyclic voltammetry measurement.....	129
4.5.3.2.2 Galvanostatic charge-discharge measurement.....	131
4.5.3.2.3 Electrochemical impedance spectroscopy (EIS) measurement.....	132
4.5.3.2.4 Discussion.....	137
4.5.3.2.5 Summary	140
V CONCLUSION	141
REFERENCES.....	146
APPENDIX.....	155
CURRICULUM VITAE	159

LIST OF TABLES

Table	Page
2.1 Comparison EDLCs and pseudocapacitors capacitors (Zhang <i>et al.</i> , 2009)	8
2.2 Summary of the various metal oxide electrodes in supercapacitor application	15
2.3 Comparison of supercapacitor performance of the PANI-based materials reported earlier.....	19
2.4 The specification 3D printing techniques	29
2.5 The advantage/drawback comparison of 3D printing techniques.....	30
2.6 The comparison of 3D electrode performances	36
3.1 The aspect ratio of 3D-printed ink composite material	69
3.2 The printing parameter of 3D-printed supercapacitor.....	77
4.1 The specification of the developed DIW 3D printer supercapacitor that use in this work.....	86
4.2 The direct ink writing techniques comparison	88
4.3 The ink comparison between reduce graphene oxide (rGO)/Methyl cellulose (MC) and reduce graphene oxide (rGO)/Cellulose acetate (CA)	95
4.4 The optimized printing parameters.....	97
4.5 The observed value of the gap between line and diameter of line of 3D.....	99
4.6 The relationship between printed layer and mass of 3D-printed Electrode	100
4.7 PANI film thickness with deposition cycle number	109
4.8 The relation between 3D-printed electrode thickness and PANI mass in 1 deposition cycle.....	110

LIST OF TABLES (Continued)

Table	Page
4.9 The areal capacitance of rGO 3D-printed electrodes from CV measurement	114
4.10 The areal capacitance of rGO 3D-printed electrodes from GCD measurement.....	116
4.11 The solution resistance (R_s) of 4, 8, 12, 16, and 20-layers 3D printed rGO electrode	118
4.12 The areal capacitance of 8 layers rGO 3D-printed electrodes with varying soaking time from CV measurement	120
4.13 The areal capacitance of 8 layers rGO 3D-printed electrodes With varying soaking time from GCD measurement	121
4.14 The solution resistance (R_s) of 8 layers rGO 3D-printed electrode under the vary electrolyte soaking time	123
4.15 The solution resistance (R_s) of 8 layers rGO 3D-printed electrode under the varying printed layer.....	127
4.16 The solution resistance (R_s) of 8 layers rGO 3D-printed electrode under the varying PANI deposition cycle	133
4.17 Areal capacitance from CV measurement at scan rate 10 mV/S, window potential: -0.9V to 0.4V, 3M KOH.....	135
4.18 Areal capacitance from GCD measurement at 1 mA/ cm ² , window potential: -0.9V to 0.4V, 3M KOH	136

LIST OF FIGURES

Figure	Page
2.1 Ragone plot for significant energy storage and conversion devices (Kim <i>et al.</i> , 2015).	10
2.2 (a) The Helmholtz model, (b) the Gouy-Chapman model, and (c) the Stern model of the electrical double layer formed at an interface in an aqueous electrolyte. IHP refers to the distance of the closest approach of ions, and OHP refers to nonspecifically adsorbed ions. (Zhang <i>et al.</i> , 2009).	12
2.3 The charging of electrochemical double-layer capacitor (carbon) adapted from (Wang <i>et al.</i> , 2020).	13
2.4 The charging of pseudocapacitor (metal oxides) adapted from (Wang <i>et al.</i> , 2020).	14
2.5 Schematic showing the typical construction of an asymmetric supercapacitor. It is reproduced with permission of Copyright 2011, Cambridge University Press.	16
2.6 The explanation process of additive manufacturing technologies. Adapted from (Ullah <i>et al.</i> , 2020)	21
2.7 The classification of Additive Manufacturing Technologies	22
2.8 Schematic representation of vat photopolymerization.	23
2.9 Schematic representation of powder bed fusion.	24
2.10 Schematic representation of FDM.	25
2.11 Schematic representation of material jetting.	26
2.12 Schematic representation of direct energy deposition	27
2.13 Schematic representation of sheet laminate	28

LIST OF FIGURES (Continued)

Figure	Page
2.14 The flow chart of pouch cell supercapacitor fabrication: (a) electrode preparation and (b) pouch cell assembly (Safitri <i>et al.</i> , 2020).	31
2.15 The components layout of a pouch cell supercapacitor: (a) carbon-coated electrodes, (b) a separator, (c) a stack of electrodes and separators, (d) front-view (left) and side view (right) of a rolled cell, and (e) an assembled pouch cell (Safitri <i>et al.</i> , 2020).....	32
2.16 a) The illustration of 3D-printed graphene aerogel fabrication. b) SEM image of 3D-printed graphene aerogel, scale bar 1 mm. c) The magnified SEM image of the cylindrical rod highlighted in (b), scale bar 40 μm . d) SEM image of 3D-printed graphene aerogel electrodeposition with MnO_2 , scale bar 1 mm. e) The magnified SEM image of cylindrical rod highlighted in (d), scale bar 40 μm . f) SEM image of the edge of 3D-printed graphene aerogel at different electrodeposition times of MnO_2 , scale bar 2 μm . g) SEM image of MnO_2 nanosheet on 3D-printed graphene aerogel, scale bar 200 nm (Yao <i>et al.</i> , 2019).	35
2.17 Cyclic Voltammograms showing rectangular features for an EDLC System and superimposed reduction and oxidation peaks for a redox active pseudocapacitor (Achilleos <i>et al.</i> , 2014).....	39
2.18 Discharge curves for an EDLC and a pseudocapacitor. Note that the EDLC shows a constant rate of discharge, while the discharge rate for the pseudocapacitor depends on the potential-dependent redox reaction rate (Achilleos <i>et al.</i> , 2014)	40

LIST OF FIGURES (Continued)

Figure	Page
2.19 Nyquist plot of EDLC a) Ideal, b) Ordinary, and c) Basic equivalent circuit of EDLC.	42
3.1 Schematic of the conventional FDM 3D printer, which has main components consisting of (1) frame, (2) build platform/print bed, (3) extruder, (4) controller board, (5) stepper motor, (6) power supply, (7) cooling fan, and (8) LCD.	45
3.2 Schematic of conventional FDM 3D printer frame.	46
3.3 The MK2B dual power heat bed	48
3.4 The schematic of the E3D extruder, the most popular extruder for FDM 3D printers. (Image courtesy of E3D).	49
3.5 RAMPS 1.4 shield, 3D printer controller board (Credit: RepRap.org)	50
3.6 a) Nema 17 stepper motor. b) micro stepper motor driver TMC 2209	51
3.7 Meanwell RSP-500-24DC power supply	52
3.8 12864 LCD display for 3D printer (Credit: RepRap.org)	53
3.9 The flowchart of 3D printer for supercapacitor process	55
3.10 The electrical wiring diagrams for RAMPS 1.4 (Reference from reppap.org).	56
3.11 The illustration of Marlin firmware configuration	57
3.12 a) Shows the initial version of the constructed FDM 3D printer. This printer underwent testing for printing accuracy and calibration by printing a reference cube. b) Schematic of fused deposition modeling component (Jin <i>et al.</i> , 2015).....	59
3.13 The reference cube model for the movement calibration	60
3.14 The illustration of DIW extruder component	61

LIST OF FIGURES (Continued)

Figure	Page
3.15 Schematic diagram of the direct ink writing for aerogel material methods: (A) pneumatic, (B) Piston-driven, and (C) screw-driven dispensing method (Derakhshanfar et al., 2018).....	62
3.16 Pneumatic dispensing development.....	63
3.17 The illustration of piston-driven.....	64
3.18 Screw-driven dispensing development for aerogel and paste material.....	65
3.19 a) The 3D-printed object with a variable condition of the ink samples. b) The 3D-printed object with a MC < 7.5 wt%. c) The printed object with CA 7.5-10.0 wt%.....	68
3.20 The degradation of 3D-printed rGO occurs when cellulose acetate is used as the binder.....	71
3.21 The bridge material print testing of cellulose acetate	73
3.22 The test printing electrode by the pneumatic extruder. The material is 5 wt% of rGO, and cellulose acetate is used as a binder. The printing speed is 5 mm/s at an air pressure of 413 KPa (60 PSI).	73
3.23 The electrode design, the net shapes 10×10 mm ² , and thickness is varied from 0.6 mm (4 layers) to 3.6 mm (24 layers).....	74
3.24 The diagram showing the preparation of a 3D-printed supercapacitor electrode.	75
3.25 The experimental procedure for preparation of conductive polyaniline by the in situ chemical oxidative polymerization approach.	78
3.26 Diagram showing the PANI coating process	79
3.27 The diagram represents Bragg diffraction by crystal planes (Adapted from Leng <i>et al.</i> , 2009)	80

LIST OF FIGURES (Continued)

Figure	Page
3.28	3-electrode electrochemical cell set up.....82
3.29	An electrochemical measurement was set up with a 3-electrode Computer control system and a Metrohm Autolab PGSTAT302N potentiostat/galvanostat.....83
4.1	a) Screw driving dispensing b) the 3D-printed objects using clay as the material.....89
4.2	a) Piston-driven extruder b) the 3D printing object which material is hydroxyapatite.....90
4.3	Pneumatic dispensing extruder. The 3D printing object, whose material is rGO/cellulose acetate, was printed on different substrates: b) nickel foam, c) plastic sheet, d) glass, e) stand-alone, and f) glass slide.....91
4.4	The printing result of ink preparation a) The 3D-printed object with MC < 7.5 wt% with infill pattern of printing parameters 5% and b) 50%. c) the CA bridge material print testing by varying the gap from 2 mm to 10 mm, and d) the CA supercapacitor electrode 3D-printed.....94
4.5	The diagram of the rGO/cellulose acetate ink preparation.....96
4.6	a) Photograph images of optimized 3D printing parameters with the designed dimension of 15 mm × 30 mm × 3 mm (LWH) on a nickel foam substrate; the image was recorded after the 3D printing at less than 1 hour. b), c), and d) SEM images of the 3D-printed electrode recorded after the 3D printing of more than 1 day at 45, 180, and 5000 magnifications, respectively.....98
4.7	The histogram of the size distribution of 3D electrode.....99
4.8	Graph shows the relationship between printed layer and the mass of 3D-printed electrode.....100

LIST OF FIGURES (Continued)

Figure	Page
4.9 PANI synthesis by chemical oxidative polymerization (COP). Change of solution color of aniline polymerization at a) 0 second, b) 20 seconds, c) 80 seconds, and d) 180 seconds, and e) 360 seconds, f) PANI deposition on glass slide. g) The PANI resistive testing.....	102
4.10 XRD pattern of the synthesized PANI using COP method.	104
4.11 a) The top view SEM image of 3D-printed electrode. b) The cross section of 3D-printed electrode.....	105
4.12 The histogram of the gap size in 3D-printed electrode.....	106
4.13 a) SEM image of PANI Nano fibrous network. b) The histogram of PANI nanofiber diameter at 46.66 ± 5.50 nm.....	107
4.14 The cross section of 24 layers 3D-printed electrode with different deposition cycle. a-b) SEM cross section of rGO/PANI 3D-printed c) 1 deposition cycle, d) 3 deposition cycles, and e) 5 deposition cycles.	108
4.15 The graph shows the relationship between PANI deposition cycle number and film thickness.	109
4.16 The relationship between 3D-printed electrode thickness and PANI mass in 1 deposition cycle.	110
4.17 CV curve of 3D-printed rGO electrode of 4 layers, 8 layers, 12 layers, 16 layers, and 20 layers with potential -0.9V to 0.4V, scan rate 5 mV/s.	112
4.18 CV curve of 3D-printed rGO electrode of 4 layers and 20 layers with potential -0.9V to 0.4V, scan rate 5 mV/s.....	113
4.19 CV curve comparison capacitance of 3D-printed rGO electrode of 4 layers, 8 layers, 12 layers, 16 layers, and 20 layers with potential -0.9V to 0.4V, scan rate 5 mV/s.....	114

LIST OF FIGURES (Continued)

Figure	Page
4.20	GCD curve of 3D-printed rGO electrode of 4, 8, 12, 16, and 20 layers at current density 1 mA/cm ² and potential -0.9V to 0.4V..... 115
4.21	GCD curve comparison capacitance 3D-printed rGO electrode of 4, 8, 12, 16, and 20 layers at current density 1 mA/cm ² and potential -0.9V to 0.4V. 116
4.22	The Nyquist plot of a 3D-printed rGO electrode with 4, 8, 12, 16, and 20 layers that have been soaked in electrolyte for 1 day. The inset image shows this Nyquist at high frequency..... 117
4.23	CV curve of 3D-printed rGO electrode of 8 layers, which vary the electrolyte soaking time with potential -0.9V to 0.4V, scan rate 5 mV/s..... 119
4.24	Comparison of CV curves for the areal capacitance of 8 layer rGO 3D printed electrodes with varying electrolyte soaking times. 120
4.25	GCD curve of 8 layers 3D-printed electrodes was measured at a current density of 1 mA/cm ² under the condition of electrolyte soaking time 1, 2, 3, and 4 days and potential -0.9V to 0.4V 121
4.26	The comparison of GCD curves for the areal capacitance of 8 layers rGO 3D-printed electrodes with varying electrolyte soaking times. 122
4.27	Nyquist plot of an 8 layers rGO 3D-printed electrode with varying electrolyte soaking times. The inset image shows this Nyquist at high frequency. 123
4.28	The comparison CV curve of rGO/PANI 3D-printed electrode of 4 layers and 24 layers 2 PANI deposition cycles with potential -0.9V to 0.4V, scan rate 5 mV/s. 125
4.29	The comparison of CV curves for the areal capacitance of 2 PANI deposition cycles of rGO/PANI 3D-printed electrodes with varying the thickness. 125

LIST OF FIGURES (Continued)

Figure		Page
4.30	GCD curve of rGO/PANI 3D-printed electrode of 4-layers and 24 layers with 2 PANI deposition cycles were measured at a current density of 1 mA/cm ² under potential -0.9V to 0.4V.	126
4.31	The comparison of GCD curves for the areal capacitance of 2 PANI deposition cycle of rGO/PANI 3D-printed electrodes with varying the thickness.	126
4.32	Nyquist plot of 8 layers rGO 3D-printed electrode which varying printed layer.	127
4.33	The comparison of CV curves for the areal capacitance of rGO/PANI 3D-printed electrodes with varying printed layer.	128
4.34	The comparison of GCD curves for the areal capacitance of rGO/PANI 3D-printed electrodes with varying printed layer.	128
4.35	The comparison CV curve of an rGO/PANI 3D-printed electrode with 8 layers, 1, 3, and 5 PANI deposition cycles, potential -0.9V to 0.4V, and scan rate of 5 mV/s.	130
4.36	The comparison of CV curves for the areal capacitance of 8 layers rGO/PANI 3D-printed electrode with 1 to 5 PANI deposition cycles.	130
4.37	GCD curve of 8 layers rGO/PANI 3D-printed electrode with 1, 3, and 5 PANI deposition cycles was measured at a current density of 1 mA/cm ² under potential - 0.9V to 0.4V.	131
4.38	The comparison of GCD curves for the areal capacitance of 8 layers rGO/PANI 3D-printed electrode with 1, 2, 3, 4, and 5 PANI deposition cycles.	132
4.39	Nyquist plot of 8 layers rGO 3D-printed electrode with varying PANI deposition cycle.	133

LIST OF FIGURES (Continued)

Figure	Page
4.40	The comparison of CV curves for the areal capacitance of rGO/PANI 3D-printed electrodes. The 3D-printed electrode of 4 layers with deposition 1 cycle is not shown in the graph because this sample was cut and utilized for SEM cross-sectional analysis 134
4.41	The comparison of GCD curves for the areal capacitance of rGO/PANI 3D-printed electrodes. The 3D-printed electrode of 4 layers with deposition 1 cycle and of 24 layers with deposition 1, 3 cycles are not shown in the graph because these samples were cut and utilized for SEM cross-sectional analysis 134
4.42	SEM of rGO/PANI 3D-printed electrode which the synthesis PANI is a colloid solution in water a) cross section SEM of 16 layers rGO 3D-printed electrode with magnification of 30X b), c), and d) is cross section SEM image at differences area of 16 layers rGO 3D-printed electrode with magnification of 5000X. e) The illustration of water evaporation from rGO 3D-printed electrode..... 138
4.43	SEM of rGO/PANI 3D-printed electrode which the synthesis PANI is a colloid solution in NMP a) cross section SEM of 24 layers rGO 3D-printed electrode with magnification of 35X b), c), and d) is cross section SEM image at differences area of 16 layers rGO 3D-printed electrode with magnification of 15000X, 1500X, and 5000X, respectively. 139
5.1	Example of ink print testing on the various substrates a) nickel foam, b) plastic sheet, c) glass, d) stand-alone sample, and e) glass slide..... 143
5.2	Ragone plot, comparing the areal power density versus the areal energy density in this study with other works in supercapacitor research field. 144

LIST OF ABBREVIATIONS

NMP	N-methyl-2-pyrrolidone
3D	Three dimensional
PANI	Polyaniline
XRD	X-ray diffraction
SEM	Scanning electron microscope
CV	Cyclic voltammetry
GCD	Galvanostatic charge/discharge
EIS	Electrochemical impedance spectroscopy
rGO	Reduced graphene oxide
CA	Cellulose acetate
CB	Carbon black
CAD	Computer-aided design
EDLC	Electrochemical double-layer capacitance
COP	Chemical oxidative polymerization
STL	Standard Tessellation Language
G-code	Geometric code
NPJ	Nano particle jetting
DOD	Drop-on-demand
DED	Direct energy deposition
LENS	Laser engineered net shaping
EBAM	Electron beam additive manufacture
PVDF	Polyvinylidene fluoride
GPL	General public license
DIW	Direct ink writing
SLA	Stereolithography
DLP	Digital light processing

LIST OF ABBREVIATIONS (Continued)

DLS	Digital light synthesis
PBF	Powder bed fusion
FDM	Fused deposition modeling
MC	Methyl cellulose



CHAPTER I

INTRODUCTION

1.1 Introduction and motivation

In recent years, the world has witnessed an urgent and growing demand for clean and sustainable sources of energy. This pressing need is primarily driven by the escalating global energy demand, which has led to the rapid depletion of non-renewable energy sources such as coal, oil, and natural gas. Consequently, there has been a significant and immediate push towards finding alternative energy sources that are sustainable and environmentally friendly. While solar, wind, and thermal energy sources are considered clean, they are only available during specific daytime or nighttime periods and not consistently throughout the day. This is precisely why the implementation of energy storage solutions becomes crucial.

One energy storage technology that has emerged in recent years with the potential to revolutionize how we store and use energy is the supercapacitor. Supercapacitors are not just energy storage devices; they are game-changers. They store and release energy quickly, unlike batteries that store energy chemically. This unique electrostatic energy storage capability allows them to charge and discharge at lightning speed, making them ideal for applications where a high amount of power is needed quickly. They also boast a longer lifespan and are more environmentally friendly than traditional batteries.

Supercapacitors are particularly intriguing because they store large amounts of energy in a small space. This compactness makes them ideal for use in portable devices such as smartphones and laptops. They are also being studied for use in electric vehicles, where they could potentially replace traditional batteries and provide a more efficient and environmentally friendly source of energy. One of the critical advantages of supercapacitors over other types of energy storage is their high power

density 10^2 to 10^5 W/kg and energy density in the range 10^{-1} to 10^1 Wh/kg. This feature sets them apart and makes them a promising solution for the future. Normally, the typical capacitor has a power density of 10^4 to 10^7 W/kg and an energy density of 10^{-2} to 10^{-1} Wh/kg (Kim *et al.*, 2015). This refers to the amount of power that can be delivered from the device per unit of volume or weight. Supercapacitors have a very high power density compared to batteries, which means that they can provide a lot of power in a small package. This makes them ideal for use in applications where space and weight are small, such as the flexible and wearable strain sensor, biomedical health monitoring, and soft robotics (Manjunatha *et al.*, 2023).

The key performance factor of a supercapacitor is its capacitance, which refers to its ability to store energy. The higher the capacitance of a supercapacitor, the more energy it can store. Several factors can affect the capacitance of a supercapacitor, including the materials' properties and structure (Zenan *et al.*, 2014), the design of the electrode (Singh *et al.*, 2015), and the electrolyte used in the device (Bhupender *et al.*, 2019).

Supercapacitor's main components are electrodes, separators, and electrolytes. The electrodes play an important role in the capacitance, which allows the ion exchange between the surface electrode and the electrolyte. Supercapacitor electrodes are normally made from carbon base material and combined with a binder such as N-methyl-2-pyrrolidone (NMP); the mixed material is coated on a conductive substrate in the form of an electrode. Moreover, the high hierarchical structure and electrode shape can improve the surface active site, resulting in more performance of the supercapacitor (Ren *et al.*, 2022). The separator is an electrical insulator that prevents the two electrodes from contacting and causing a short circuit. The electrolyte contains ions that can move when the voltage is applied to the electrode. The electrolyte contains ions that can move when a voltage is applied to the electrode. Moreover, with a high electrolyte concentration, ion transport within the electrode layer becomes easier, resulting in improved supercapacitor performance (Balli *et al.*, 2019).

Materials structure of the electrode: Numerous studies have been conducted to investigate the shape and structure of supercapacitor electrodes with the aim of

enhancing their performance and achieving high efficiency. 3D flower-like CuCo_2O_4 as an electrode for supercapacitor shows highly mesoporous unique architecture plays an important role in achieving high capacity/capacitance with superior cycle life. The high surface area and mesoporous nature offer sufficient reaction sites and can accelerate the liquid electrolyte to penetrate the electrode and the ions to reach the reacting sites. (Jadhav *et al.*, 2016). The carbon foam, a macroporous structure containing a network of mesoporous channels filled with micropores, has a specific surface area of $2685 \text{ m}^2/\text{g}$ and achieves an outstanding capacitance of 402.5 F/g at 1 A/g (Peng *et al.*, 2019). A 3D hierarchical hybrid nanocomposite of $\text{NiO}/\text{Co}_3\text{O}_4@\text{C}/\text{CoS}_2$ hybrid electrode exhibits significant improvement in electrochemical performance, with a high capacity of 1025 F/g at 1 A/g (Xingxing *et al.*, 2020). Porous 3D graphene aerogel (GA) embedded with gold nanoparticles (3D Au/GA) has a high specific capacitance of 554 F/g at 5 mV/s (Sahoo *et al.*, 2021).

The shape of the electrodes: The limitations of the traditional bulk capacitor electrode are the surface mass ratio and the working area of the redox reaction because of the sluggish ion diffusion (Bin *et al.*, 2019). It is well known that the morphology of the active material is one cause of the performance of the high surface active electrode and high ion transport active site. 3D printing technology is one candidate for fabricating a hierarchical electrode. In order to improve the performance of supercapacitor electrodes, researchers have been investigating new materials and fabrication methods. One such method is 3D printing (Bin *et al.*, 2018), which has the potential to revolutionize the way that supercapacitor electrodes are made. 3D printing allows for the precise control of the shape and size of the supercapacitor electrodes, which can improve the performance of the device. The high hierarchical geometry electrode improves the performance of supercapacitor, such as the 3D graphene printed electrode with high MnO_2 loading, which demonstrated the areal capacitance increased with mass loading. The gravimetric and volume matrix capacitance remains unchanged with MnO_2 loading (Bin *et al.*, 2019).

Conclusion: This research aims to develop 3D-printed supercapacitor electrodes and investigate the 3D printing machine, the shape of electrodes, and material structures affecting the capacitance values. The extruder system of 3D printing

techniques is developed, and the active and carbon-based materials are prepared in gel solution with different conditions and printed on the substrate by varying the electrode thickness. The 3D-printed electrode is deposited by polyaniline (PANI) for the growth nanostructure on the surfaces. X-ray diffraction (XRD) and scanning electron microscope (SEM) are used to characterize the morphology, and the electrochemical was examined by cyclic voltammetry (CV), galvanostatic charge/discharge (GCD), electrochemical impedance spectroscopy (EIS), and electrochemical stability.

Ideas and hypothesis: The 3D nanoscale structure of active material in a supercapacitor electrode offers a high hierarchical surface area, enhancing the ion exchange between the electrode and electrolyte. This can improve the supercapacitor performance. If the parameters and material conditions are optimized, the 3D microstructure of the electrode can be fabricated using 3D printing methods and serve as a scaffold for the 3D nanoscale structure of the supercapacitor's active material.

Hypothesis 1 (H1): The extruded 3D printing method is suitable for the 3D-printed electrode because the materials must be prepared in high-viscosity ink. Three types of extruder 3D printing techniques are considered, pneumatic, piston-driven, and screw-driven dispensing.

Hypothesis 2 (H2): Carbon-based materials can be mixed with cellulose materials and are suitable candidates for 3D-printed supercapacitor electrodes.

Hypothesis 3 (H3): 3D printing parameters, including layer number, flow speed, and printing speed, affect the shape and capacitance values of the 3D-printed electrodes.

Hypothesis 4 (H4): PANI coating process (coating method and cycle numbers) affects the capacitance values of the 3D electrodes.

Hypothesis 5 (H5): Electrochemical measurement preparation (soaking time in electrolyte) affects to capacitance values of the 3D electrodes.

1.2 Research objectives

- 1.2.1 To design and develop a 3D printer for fabrication of supercapacitor electrodes.
- 1.2.2 To study and prepare the high viscous ink 3D-printed electrodes using

carbon and cellulose-based materials.

- 1.2.3 To study printing parameters of the 3D-printed supercapacitor electrodes.
- 1.2.4 To synthesis and coat PANI on 3D-printed supercapacitor electrode.
- 1.2.5 To study electrochemical properties of the 3D-printed supercapacitor electrodes.

1.3 Scope and limitations of the study

- 1.3.1 This study focuses on developing of 3D supercapacitor electrode by using extruded 3D printing technique.
- 1.3.2 The carbon-based materials used in this work are activated carbon (AC), carbon black (CB), and reduced graphene oxide (rGO).
- 1.3.3 Conductive polymer polyaniline (PANI) was used to improve the capacitance of the 3D electrode.
- 1.3.4 A one-pot solution of aniline synthesized by the self-assembly method was used for PANI deposition on 3D-printed electrodes.
- 1.3.5 The printing pattern of the 3D electrode used in this work is a square pattern.
- 1.3.6 Scanning electron microscope (SEM) and X-ray diffraction (XRD) are the main characterization techniques for the physical properties of 3D-printed electrodes.
- 1.3.7 The electrochemical performances of 3D-printed electrode was investigated by cyclic voltammetry (CV), galvanostatic current charge-discharge, and electrochemical impedance spectroscopy (EIS).

1.4 Location of research

- 1.4.1 Advanced Materials Physics Laboratory (AMP Lab), School of Physics, Institute of Science, Suranaree University of Technology, Nakhon Ratchasima, Thailand.
- 1.4.2 The Center for Scientific and Technological Equipment, Suranaree University of Technology, Nakhon Ratchasima, Thailand.
- 1.4.3 National Security and Dual-Use Technology Center: NSD, NSTDA, Bangkok,

Thailand.

1.5 Instrumentation

- 1.5.1 Home-built extruder-based 3D printing machine
- 1.5.2 High current potentiostat/galvanostat system (AUTOLAB PGSTAT302N, Netherlands)
- 1.5.3 X-ray diffractometer (XRD), D8 advance, Bruker.
- 1.5.4 Scanning electron microscope (SEM), Oxford instruments.
- 1.5.5 Hot plate and magnetic stirrer
- 1.5.6 Electronic balance
- 1.5.7 Fume hood
- 1.5.8 Micropipette
- 1.5.9 Ultrasonicate
- 1.5.10 Beaker
- 1.5.11 Plastic syringe 10 ml

1.6 Expected Output / Outcome

- 1.6.1 Achievable and skilled in fabricating and developing the new technology of 3D printing in laboratories and other applications.
- 1.6.2 Achievable in the high viscous ink 3D-printed electrode preparation.
- 1.6.3 The optimized printing parameters in this work are discovered.
- 1.6.4 Understanding of the PANI synthesis and used for supercapacitor applications.
- 1.6.5 Understanding of how the shape and morphology of the 3D electrode impact the properties of supercapacitors.

Apart from the thesis, the primary focus is developing a 3D printing system for energy storage electrodes, specifically supercapacitor electrodes. The advantage of this thesis lies in its potential to serve as a prototype for developing systems for various applications, including laboratory experiments, industrial settings, and real-life applications.

1.7 Overview of the research thesis

This thesis is divided into five chapters. The first chapter provides background information: introduction (Chapter I), theoretical background (Chapter II), methodology (Chapter III), results and discussion (Chapter IV), and finally, conclusion (Chapter V).

- **In Chapter II**, theoretical research delves into the intricacies of the supercapacitor and 3D printing technology. A description of the ink selected in this work is employed
- **Chapter III**, details the design and development of 3D printers for supercapacitors. The 3 types of candidates for the extruder system are considered the most suitable for this work. The ink selection and condition will be provided. The optimized ink condition is print tested as a design in the computer-aided design program (CAD). The simple PANI synthesis and drop coating are present in the film on the 3D-printed electrode. In addition, this chapter also includes material characterization.
- **In Chapter IV**, the experimental results were provided. The first part results from 3D printing development, ink selection, and print testing. The printing results of carbon-based material for supercapacitor electrodes were presented. PANI deposition on 3D-printed electrode results and their condition are presented. In addition, this chapter also includes the characterization of material such as XRD, SEM, and electrochemical properties
 - XRD was used for phase identification of PANI
 - SEM was performed to investigate the morphology and structure

Electrochemical measurement

- CV was used for studying the redox process, electrochemical kinetics, and active surface area.
 - GCD was used for evaluating energy storage capacity, charge discharge kinetic
 - EIS was performed for characterization of interfaces and electrolyte
- **In Chapter V**, the conclusion of all section will be provided in this chapter.

CHAPTER II

LITERATURE REVIEW

The supercapacitor operates on a principle similar to that of a capacitor but with higher energy density and power density. The main components of a supercapacitor are electrodes, an electrolyte, and a separator, each of which affects the capacitance. The electrode, for example, consists of a material and structure that facilitates ion exchange between its surface and the electrolyte. Carbon-based materials exhibit electrochemical double-layer capacitance (EDLC), while conductive materials like PANI possess pseudocapacitive properties. These two material types have distinct advantages and limitations, as outlined in Table 2.1. Furthermore, the electrode's structure plays a significant role in ion exchange. For instance, a 3D flower-like structure at the nanoscale, such as CuCo_2O_4 , has been used as an electrode for supercapacitors (Jadhav *et al.*, 2016). Additionally, printed 3D supercapacitor electrodes can enhance the surface area available for ion exchange with the electrolyte (Chu *et al.*, 2020).

Table 2.1 Comparison EDLCs and pseudocapacitors capacitors (Zhang *et al.*, 2009).

Parameters	EDLC	Pseudocapacitor
Storage mechanism	Non-faradic/electrostatic, electrical charge stored at the metal/electrolyte interface	Faradic, reversible redox reaction
Specific capacitance	Lower	Higher
Energy density (Wh/kg)	Low (<0.1)	High (1-10)
Cycle Life/stability	High (>500,000)	Low (>100,000)
Material	Carbon-based materials, e.g. activated carbon, carbon nanotubes	Metal oxides, conducting polymers, e.g., NiO, MgO, PANI

The comparison between EDLCs and pseudocapacitors is shown in Table 2.1. Synergizing these two supercapacitor materials holds great potential for overcoming limitations and enhancing supercapacitor performance. Direct ink writing using pneumatic dispensing in 3D printing is a promising technique for fabricating 3D electrodes. The materials used in this technique should have a paste-like consistency with high viscosity. For instance, reduced graphene oxide (rGO) is an active material with high conductivity and low resistance. At the same time, cellulose acetate serves as a binder in the form of a paste with acetone as the solvent. The 3D-printed carbon-based material used for EDLCs is coated with PANI, a pseudocapacitive material. To evaluate the performance of 3D-printed rGO/PANI, material characterization (SEM and XRD) and electrochemical measurements are conducted.

To achieve the objectives of this work, the following section provides a literature review and explores relevant theories.

2.1 Electrochemical capacitor

As the development of portable electronic devices and other electrical appliances increases, the demand for power supplies has also increased. Batteries have always been a popular power supply because they can hold much charge. However, unsatisfied batteries still limit their performance, such as low power, taking a long time to charge, the number of charging times is estimated to be at most 1000 times, and generating heat during charging. However, another energy storage source is capacitors, commonly used in electronic circuits. Because it has the advantage of fast charging, discharging, and long cyclic stability. To combine the benefits of batteries and capacitors, we call supercapacitor or electrochemical capacitor properties, which are highly efficient for energy storage, as shown in Figure 2.1. The supercapacitor was first discovered in 1957 by Howard Becker of General Electric (GE); made of porous carbon and used acidic and super-formal electrolytes. The first commercial supercapacitor was created in the 1970. Since then, researchers have been focused on suitable materials and electrolytes to develop the potential of supercapacitors. The energy storage process of a supercapacitor can be divided into two processes;

1. Electrostatic Double Layer Capacitance (EDLC): electrostatic storage of the

electrical energy achieved by charge separation in a Helmholtz double layer.

2. Pseudocapacitor: electrochemical storage of the electrical energy achieved by faradaic redox reactions with charge transfer.

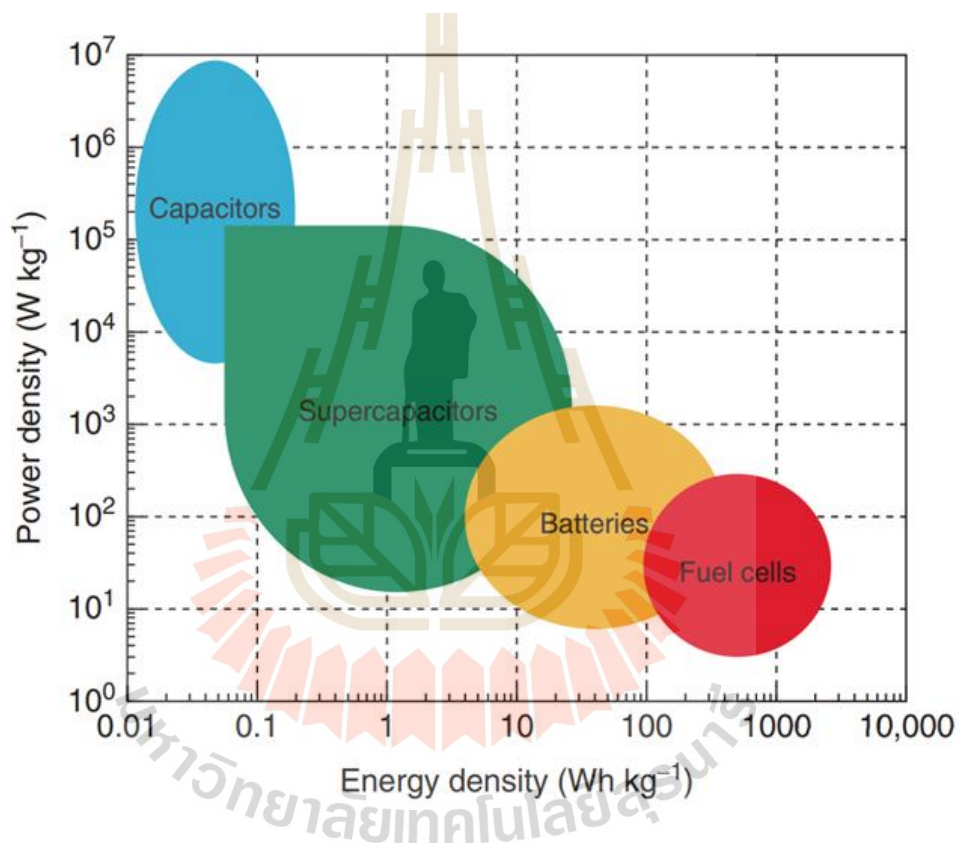


Figure 2.1 Ragone plot for significant energy storage and conversion devices (Kim *et al.*, 2015).

2.1.1 Electrochemical double layer capacitor (EDLC)

Electric double-layer capacitors (EDLCs) are energy storage devices that store energy as an electrostatic charge at the interface between a solid electrode and an electrolyte. The electrodes in EDLCs are typically made of porous carbon materials

with a high surface area, which provides a large surface area for the electrolyte to come into contact with. The electrolyte used in EDLCs is typically a liquid or gel containing ions, facilitating the charge transfer between the electrodes.

The principle of EDLC is shown in Figure 2.2. Helmholtz first described the accumulation of charges only at the electrode/electrolyte interface with capacitance (C) as equation (2.1)

$$C = \epsilon_0 \epsilon_r A / d \quad (2.1)$$

Where ϵ_0 and ϵ_r are the permittivity of free space and dielectric constant dielectric, A is the electrode surface area, and d is the adequate thickness of the double layer or charge separation distance. The separation distance is usually in angstrom range, Gouy-Chapman suggested the presence of a diffuse layer in the electrolyte close to the electrode surface (Gouy *et al.*, 1910). Stern then combined the Helmholtz and the Gouy-Chapman models and expressed the double-layer capacitance as a result of the charge accumulation of the Helmholtz layer at a thickness equal to the size of the solvent molecule and the diffuse layer where charges are scattered due to thermal fluctuation of the electrolyte (Stern *et al.*, 1924)

capacitance (C_{total}) is the series capacitance of the compact Helmholtz layer and the diffuse layer as given:

$$\frac{1}{C_{total}} = \frac{1}{C_H} + \frac{1}{C_{diff}} \quad (2.2)$$

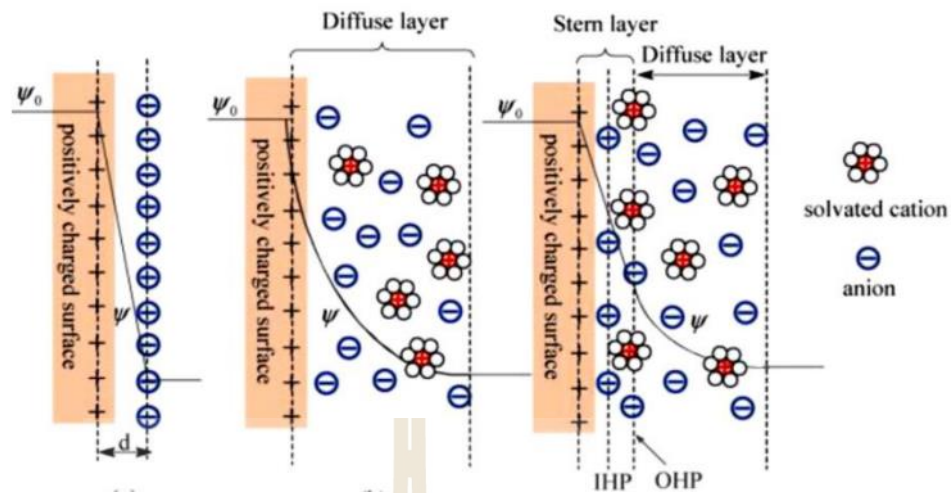


Figure 2.2 (a) The Helmholtz model, (b) the Gouy-Chapman model, and (c) the Stern model of the electrical double layer formed at an interface in an aqueous electrolyte. IHP refers to the distance of the closest approach of ions, and OHP refers to nonspecifically adsorbed ions. (Zhang *et al.*, 2009).

Electrostatic means transferring electrical charges between two electrodes, providing longer cyclic stability than batteries that rely on chemical processes. (Gualous *et al.*, 2003). Upon contact between active electrode materials and the electrolyte, positive and negative charges distribute themselves closely, forming what is known as an electrical double layer (EDL). This layer spans a short distance, typically ranging from 2 Å to 10 Å.

When a voltage is applied to an EDLC, the electrodes become polarized, and an electrostatic double layer forms at the interface between the electrode and the electrolyte. The double layer is formed by the accumulation of ions at the electrode surface, which separates charges and creates a potential difference. The amount of charge that can be stored at the electrode-electrolyte interface is proportional to the surface area of the electrode and the concentration of ions in the electrolyte (Kim *et al.*, 2022).

The capacitance of an EDLC is proportional to the amount of charge that can be stored at the electrode-electrolyte interface, and it is typically several orders of magnitude higher than that of a conventional capacitor. The energy density of an EDLC is determined by the amount of charge that can be stored and the voltage applied, while the power density is determined by the rate at which charge can be delivered or absorbed. The illustration of EDLC is shown in Figure 2.3. Usually, the EDLC electrode materials are porous carbons, such as activated carbons with high capacitance (100–200 F/g) and high specific surface area ($>1000 \text{ m}^2/\text{g}$) in microporosity (Shiraishi *et al.*, 2003).

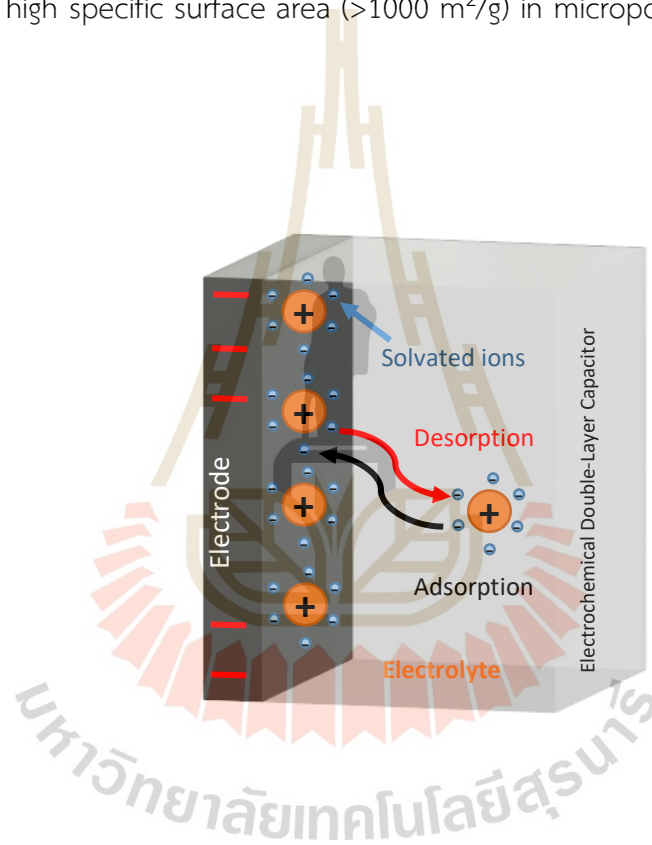


Figure 2.3 The charging of electrochemical double-layer capacitor (carbon) adapted from (Wang *et al.*, 2020).

2.1.2 Pseudocapacitor

Pseudocapacitors store electrical energy faradaically by electron charge transfer between electrode and electrolyte from a desolvated and adsorbed ion. The charge storage achieved by this mechanism is approximately 1-100 orders of magnitude higher than for the electric double layer (EDL) mechanism (Conway *et al.*, 1999). The

pseudocapacitor mechanism can refer to reversible and rapid redox reactions. The reaction occurs at the electrode-electrolyte interface, leading to electrical energy storage, as in Figure 2.4. When the voltage is applied to the pseudocapacitor, The iron of the electrolyte is attracted to the surface of the electrode. The absorbed ion forms a charge layer with the reversible oxidation and reduction reaction at the electrode-electrolyte interface.

The most attractive materials are transition metal oxide materials, such as Ruthenium oxides (RuO_2), Manganese oxide (MnO_2), other oxides, and conductive polymers. These materials have been widely investigated and are shown in Table 2.2. RuO_2 has a high theoretical specific capacitance value (1400–2000 F/g) but is highly toxic and has a high production cost (Dipanwita *et al.*, 2019). MnO_2 has been intensively investigated due to its natural abundance, high theoretical capacity (~1370 F/g), and low toxicity (Huang *et al.*, 2015). Polyaniline, a conductive polymer, has also been investigated for energy storage applications due to its attractive properties, such as high electrical conductivity, flexibility, environmental stability, low operational voltage, high theoretical pseudocapacitance, low cost, and abundance of the material (Hossein *et al.*, 2019). In theory, polyaniline (PANI) can have a specific capacitance of 2103 F/g (Hanlu *et al.*, 2009). A flexible current collector of a supercapacitor, deposited with PANI using a spraying technique, exhibited a high specific capacitance of 594.92 F/g at a scan rate of 5 mV/s, with a scanning potential window of (-0.8V to 0.8 V) (Shaker *et al.*, 2016).

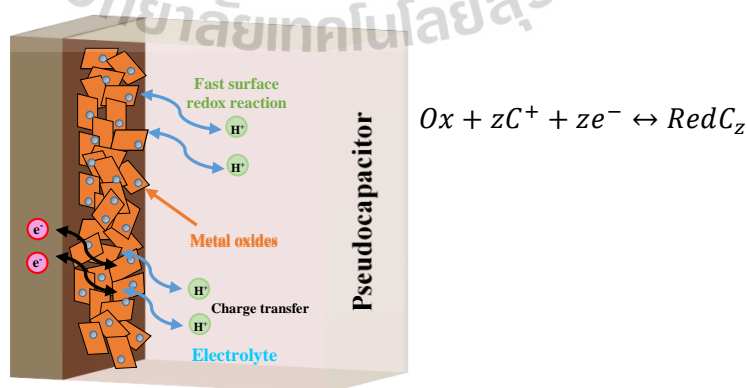


Figure 2.4 The charging of pseudocapacitor (metal oxides) adapted from (Wang *et al.*, 2020).

Table 2.2 Summary of the various metal oxide electrodes in supercapacitor application.

Material	Electrolyte	Capacitance (F/g)	References
CO ₃ O ₄	1.0 M KOH	358	Xin <i>et al.</i> , 2011
	1.0 M KOH	548	Meher <i>et al.</i> , 2011
	0.1M Na ₂ SO ₄	396.67	Niveditha <i>et al.</i> , 2018
CO ₃ O ₄ /Graphene	2.0 M KOH	978.1	Shuhua <i>et al.</i> , 2018
Fe ₃ O ₄	1.0M Na ₂ SO ₄	207.7	Lu <i>et al.</i> , 2013
Fe ₃ O ₄	1.0 M KOH	325.7	Tsung <i>et al.</i> , 2015
Fe ₃ O ₄ /rGO	1.0 M KOH	661	Tsung <i>et al.</i> , 2015
NiCO ₂ O ₄	3.0 M KOH	678	Yuan <i>et al.</i> , 2013
MnCO ₂ O ₄	6.0 M KOH	346	Padmanathan <i>et al.</i> , 2013
NiO	1.0 M KOH	2,584	Kong <i>et al.</i> , 2011
CuO	6.0 M KOH	1,800	Liu <i>et al.</i> , 2018
MnO ₂	0.1M Na ₂ SO ₄	1,380	Toupin <i>et al.</i> , 2004
PANI	1.0 H ₂ SO ₄	2,000	Hanlu <i>et al.</i> , 2009

2.1.3 Asymmetric supercapacitor

Asymmetric supercapacitors are composed of two dissimilar materials assembled as anode and cathode, as shown in the schematic in Figure 2.5. Generally, the anode is based on activated carbon, such as EDLC, and the pseudocapacitive metal oxide is based on the cathode. The unique design of the asymmetric supercapacitor offers a sizeable operating voltage window and high energy density. For the example of the asymmetric supercapacitor, the maximum voltage of 4.5 V exhibited a very high energy density of 103.8 Wh/kg (Wang *et al.*, 2010).

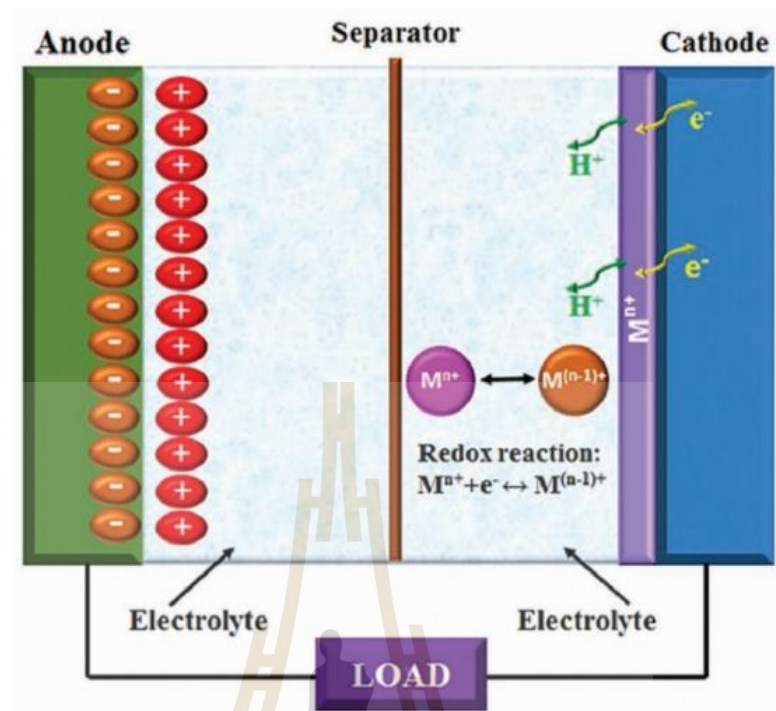


Figure 2.5 Schematic showing the typical construction of an asymmetric supercapacitor (Choudhary *et al.*, 2017).

2.2 Polyaniline (PANI)

Polyaniline (PANI) is a conductive polymer that plays a vital role in energy storage systems as a pseudocapacitive material. In the past, researchers have given PANI significant attention due to its high specific capacitance, flexibility, easy method of preparation, and low cost.

2.2.1 The properties of polyaniline

PANI has various properties, which depend on its form. Its chemical nature determines its color (Abdulwahhab *et al.*, 2022).

- white/clear or colorless, if the polymer form is leucoemeraldine and the polymer type is pernigraniline.
- blue to violet color, if the polymer form is emeraldine basic form.
- green color, if the polymer form is emeraldine salt form.

All forms of PANI are insoluble in water, acetone, ethanol, and other solvents but soluble in dimethylformamide, dimethyl sulfoxide, and N-methyl-2-pyrrolidone (Shacklette *et al.*, 1993). PANI can be a conductive polymer only in an emeraldine form (Babel *et al.*, 2021). Generally, the range of PANI conductivity is from $\sigma \leq 0.1\text{--}10\text{ S/cm}$ (undoped base emeraldine) to $\sigma \geq 10\text{ S/cm}$ (doped salt emeraldine). Moreover, PANI has anti-corrosion properties: polyaniline composites have outstanding performance in smart coatings, superhydrophobic coatings, and capacitive material. PANI has been widely used in energy storage, especially supercapacitor, because it can improve the the capacitance due to the rapid oxidation and reduction reaction (Weerasinghe *et al.*, 2018)

2.2.2 Synthesis of PANI

PANI has various preparation methods. In this work, chemical polymerization is used to synthesise PANI because it is a simple method capable of preparing large quantities. In this method, PANI was prepared by chemical oxidative polymerization (COP) of aniline monomer using ammonium persulfate as a redox initiator.

Polyaniline synthesis methods:

- Electrochemical polymerization
- Chemical polymerization
- Vapor-phase polymerization
- Photochemically initiated polymerization
- Enzyme-catalyzed polymerization

Controlling the morphology of PANI

The morphology of PANI is affected by various reaction parameters and conditions, such as the dopant and monomer.

- Dopant and monomer: the dopant (HCl and HNO₃) has a significant effect on controlling the morphology (Diggikar *et al.*, 2019)

- Reaction condition: the different stirring speeds offer the PANI nanostructures synthesized (Park *et al.*, 2012). The decrease in temperature of PANI synthesis affects the increases in PANI rod size (Chandra *et al.*, 2016).

PANI synthesis by chemical polymerization is simple, cheap, and capable of preparing large quantities, which makes it suitable for this work. Hanlu and colleagues reported a specific capacitance of 2,000 F/g for polyaniline (Hanlu *et al.*, 2009). Furthermore, many studies have been focused on improving PANI through composites with other materials. For example, the MnO₂/PANI composite on carbon fiber paper exhibited a high specific capacitance of 437 F/g at 1 A/g (Yang *et al.*, 2015). PANI/carbon powder composites provided the specific capacitance of 304.87 F/g (Santi *et al.*, 2019), and polyaniline/graphene nanocomposites (PANI/Gr) exhibited a specific capacitance of 922 F/g at 10 mV/s (Du *et al.*, 2013).

Moreover, the nanostructure and morphology of PANI offer benefits for supercapacitor electrodes, providing a large surface area and interface. PANI can form various nanostructures, such as nanoflakes, nanofibers, nanorods, nanosheets, and nanoparticles. The formation of these structures is determined by the conditions of the polymerization solution (Jixiao *et al.*, 2007). Previous studies have demonstrated remarkable electrochemical properties for PANI-based materials, as shown in Table 2.3.

Table 2.3 Comparison of supercapacitor performance of the PANI-based materials reported earlier.

Material	Discharge rate	Potential range (V)	Electrolyte	Specific capacitance (F/g)	Ref.
PANI	10 mV/s	-0.1 - 0.8	1 M H ₂ SO ₄	503	Dhawale <i>et al.</i> , 2011
PANI	2 mA/cm ²	0 - 1.0	1 M H ₂ SO ₄	480	Sivaraman <i>et al.</i> , 2010
PANI nanowires	23 A/g	0 - 0.75	1 M H ₂ SO ₄	742	Gupta <i>et al.</i> , 2005
Self-doped PANI	1 A/g	-0.6 - 0.7	0.5 M Na ₂ SO ₄	408	Bian <i>et al.</i> , 2012
PANI/C	2 A/g	-0.2 - 0.8	0.5 M H ₂ SO ₄	1486	Bavio <i>et al.</i> , 2014
Mesoporous C/PANI	2 mV/s	-0.1 - 1.0	1 M H ₂ SO ₄	470	Zhou <i>et al.</i> , 2011
G/PANI	1 A/g	0 - 1.0	1 M H ₂ SO ₄	808	Zhang <i>et al.</i> , 2017

2.3 3D printing development for supercapacitor

3D printing is an additive technology for manufacturing parts. It does not require a block of material or a mold to manufacture physical objects; it simply stacks and fuses layers of material, as shown in Figure 2.6. It is typically fast, has low setup costs, and can create more complex geometries than traditional technologies, with an ever-expanding list of materials. It is used extensively in engineering, particularly for prototyping and creating lightweight geometries.

Hideo Kodama first patented 3D printing in Japan in 1981. The technique at that time was UV light irradiation onto photopolymers. In 1987, 3D System released the first commercial stereolithography (SLA).

It is well known that the manufacturing process is the part of casting or turning. These processes are complex, time-consuming, and costly. 3D printing technology has overcome these disadvantages. In addition, in the troubleshooting steps, 3D printing allows us to plan efficient production and design samples on a computer. This allows us to create precisely the desired model before production. The 3D printing process starts with designing an object in a computer program; then, the 3D file is converted into a G-code file by slicing program. The popular 3D printer technique is fuse deposition modeling, which injects plastic filament through a high-heat nozzle. From the past to the present, 3D printing technology has constantly evolved with new 3D printing techniques. Each 3D printing technique has a different operation, as presented in Tables 2.4 and 2.5. 3D printers can be categorized into several types of processes, as in Figure 2.7:

- 1 **Vat Polymerization:** liquid photopolymer is cured by light.
- 2 **Material Extrusion:** molten thermoplastic is deposited through a heated nozzle.
- 3 **Powder Bed Fusion:** powder particles are fused by a high-energy source.
- 4 **Material Jetting:** liquid photosensitive fusing agent droplets are deposited on a powder bed and cured by light.
- 5 **Binder Jetting:** droplets of liquid binding agent are deposited on a bed of granulated materials, which are later sintered together.
- 6 **Direct Energy Deposition:** molten metal simultaneously deposited and fused.
- 7 **Sheet Lamination:** individual sheets of material are cut to shape and laminated together.

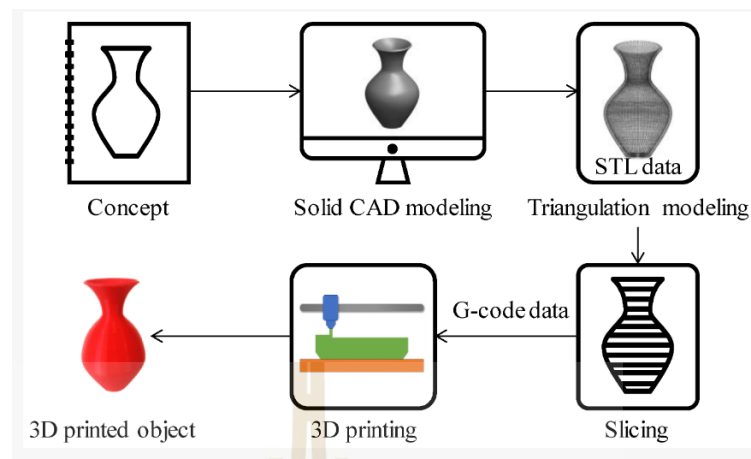


Figure 2.6 The explanation process of additive manufacturing technologies (Ullah *et al.*, 2020).

The process of 3D printing can follow these steps.

- Design the concept of the object to be fabricated.
- Create the concept object using a computer-aided design (CAD) program.
- Convert the CAD file to STL format for compatibility with any 3D printer.
- Slice the CAD model with various parameters in a slicing program to obtain a G-code file format.
- Execute the G-code file to initiate the printing process.
- Remove the printed object from the print bed.

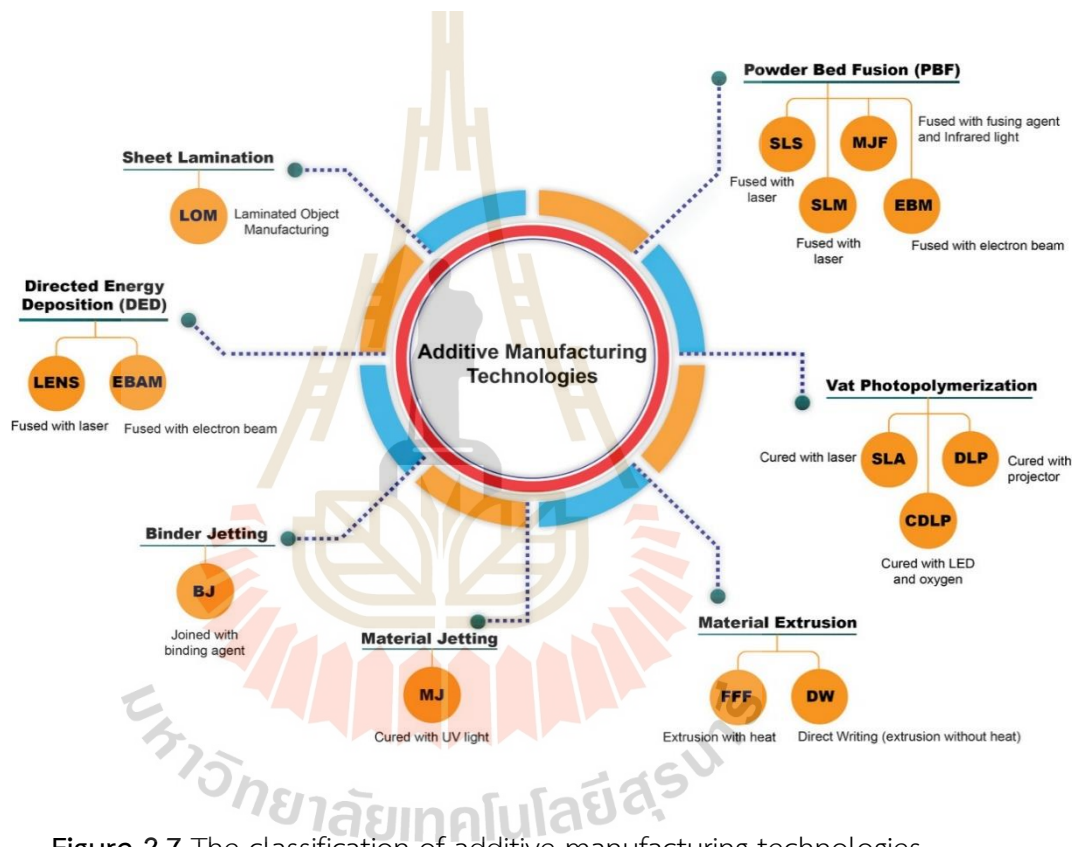


Figure 2.7 The classification of additive manufacturing technologies.

2.3.1 The Classification of additive manufacturing technologies

Vat photopolymerization

Photopolymerization is when a photopolymer resin is exposed to specific wavelengths of light, causing it to solidify, shown Figure 2.8. Stereolithography (SLA), digital light processing (DLP), and digital light synthesis (DLS) are the three main vat polymerization techniques. These techniques transform liquid resin into solid, resulting in highly detailed objects with a resolution of 10-30 microns. However, vat photopolymerization is generally not suitable for multi-material printing due to the difficulty in controlling the contamination of the vat by different materials (Rafiee *et al.*, 2020).

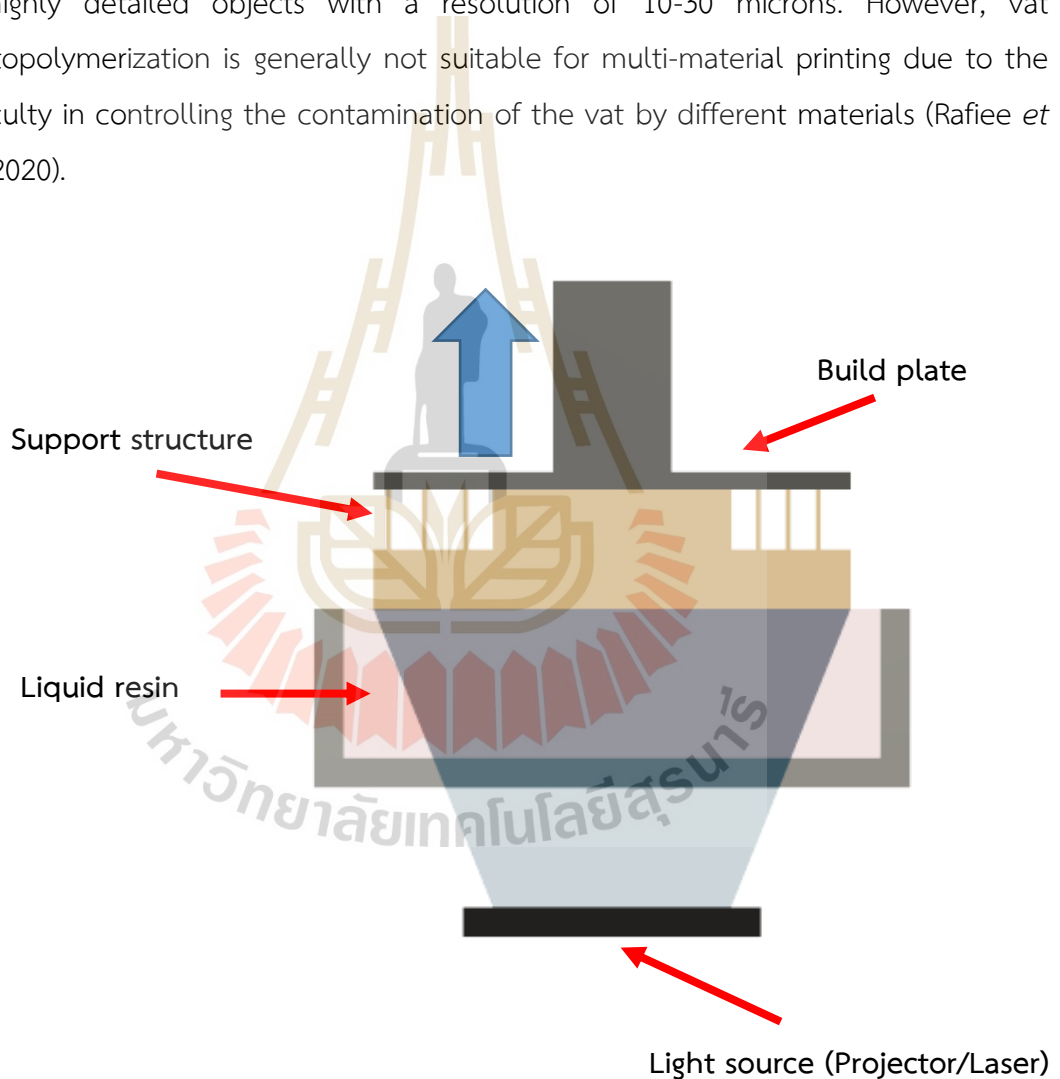


Figure 2.8 Schematic representation of vat photopolymerization.

Powder bed fusion

Powder bed fusion (PBF) technologies utilize a heat source to induce fusion (sintering or melting) between plastic or metal powder particles, layer by layer, as shown in Figure 2.9. PBF a high level of detail in the printed object, but post-processing is still required to refine the details. However, when using this technique, careful consideration must be given to the material selection, considering the melting point of the powder material and its heat transfer properties.

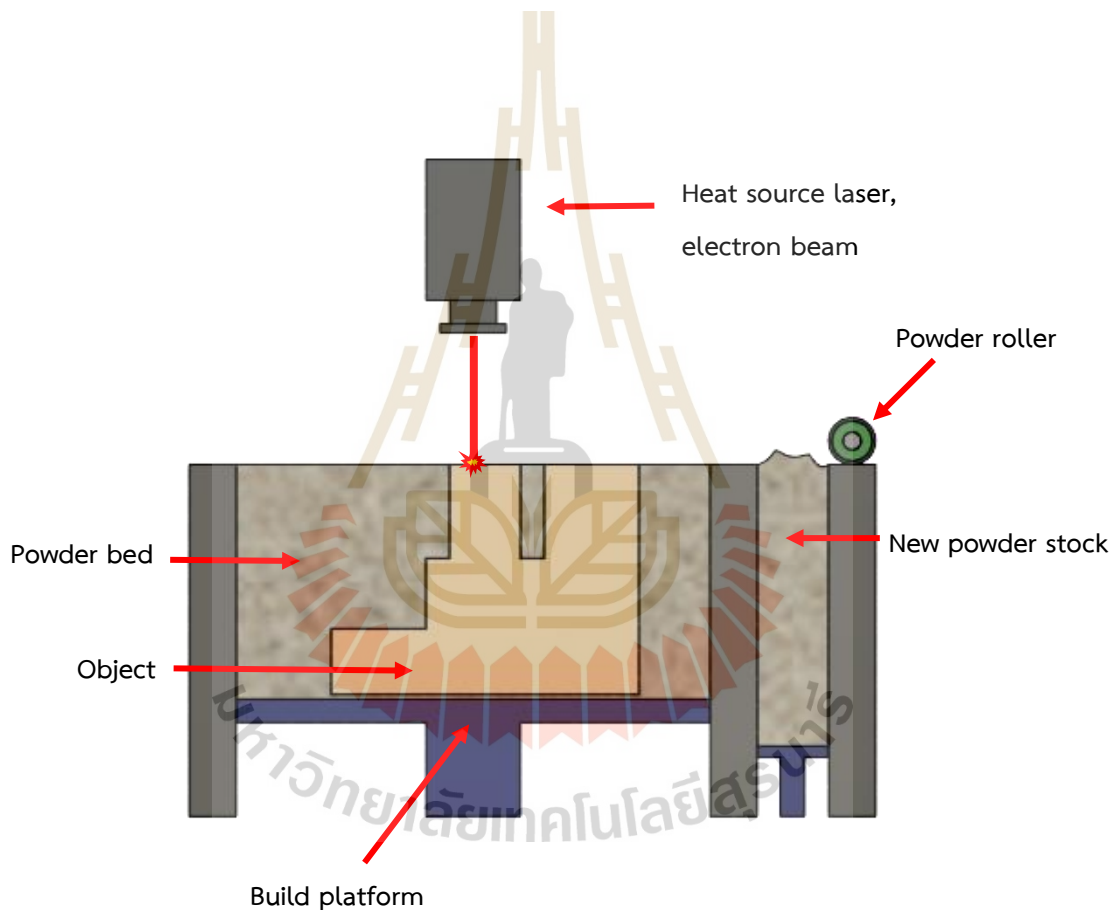


Figure 2.9 Schematic representation of PBF.

Material extrusion

Material extrusion involves squeezing a material through a nozzle onto a build plate, layer by layer, shown Figure 2.10. Fused deposition modeling (FDM) is a widely used 3D printing technology that falls under this category. Material extrusion has many advantages, which have garnered attention from researchers. Depending on the application, it can print with multiple materials, using either heated or non-heated nozzles. The materials can be in powder, filament, or paste, and the cost of the printer system is relatively inexpensive. The versatility of material extrusion has attracted attention in materials research and other disciplines such as medicine, biology, engineering, and more.

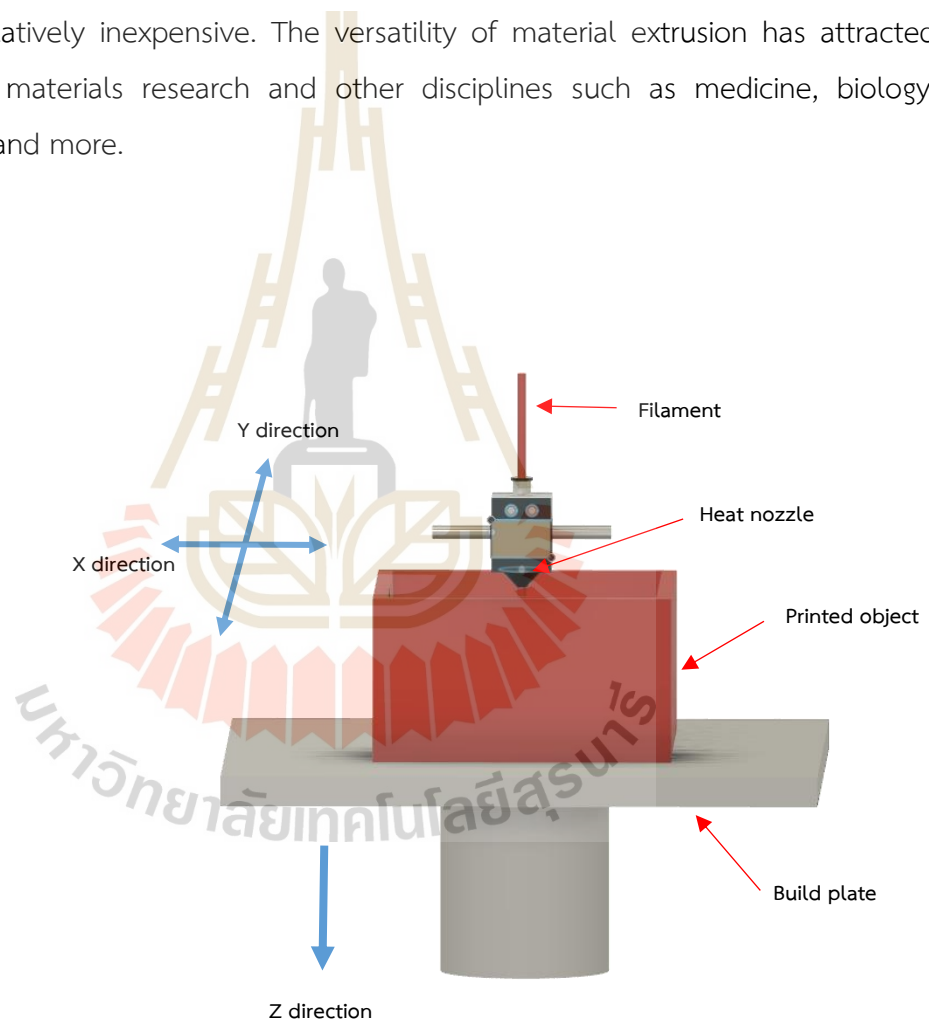


Figure 2.10 Schematic representation of FDM.

Material jetting

Material jetting technologies use UV light or heat to harden photopolymers, metals, or wax, building parts one layer at a time, shown Figure 2.11. Nanoparticle jetting (NPJ) and Drop-on-demand (DOD) are two other types of material jetting.

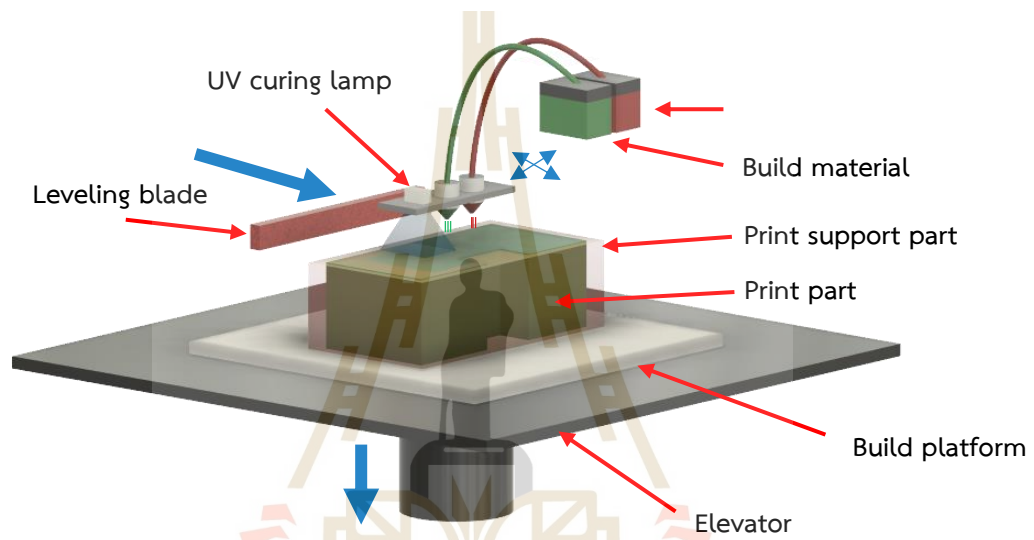


Figure 2.11 Schematic representation of material jetting.

Binder Jetting

Binder jetting is similar to material jetting, but it uses an industrial printhead to deposit a binding adhesive agent onto thin layers of powder material. Unlike other 3D printing technologies, binder jetting does not require heat.

Direct energy deposition

Direct energy deposition (DED) creates 3D objects by melting powder material as deposited, shown Figure 2.12. It is mainly used with metal powders or wire and is often called metal deposition. Laser engineered net shaping (LENS) and electron beam additive manufacture (EBAM) also fall within this category.

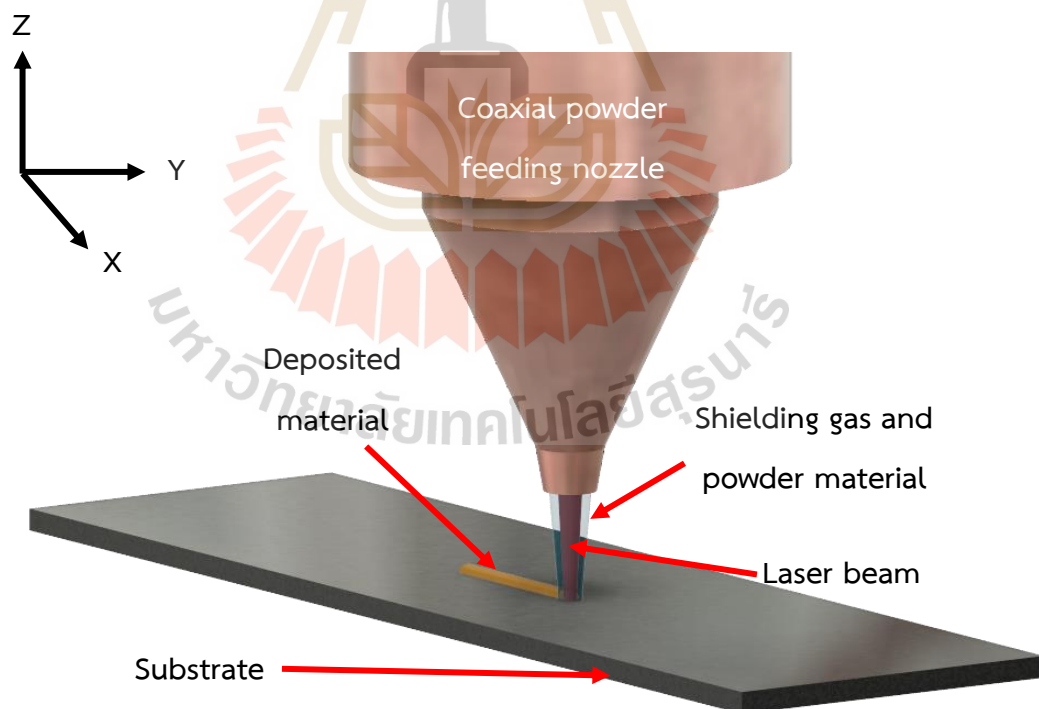


Figure 2.12 Schematic representation of DED.

Sheet lamination

A thin sheet of material is fed from the roller or placed onto the build platform. Depending on the type of sheet lamination, the next layer may or may not be bonded to the previous sheet. Selective deposition lamination (SDL) and ultrasonic additive manufacturing (UAM) bond the layers together and then cut the 3D shape at the end, while the cut-then-stack paradigm of computer-aided manufacturing of laminated engineering materials (CAM-LEM) cuts the layers into shape and then bonds the layers together. The process continues until all the layers are completed to achieve the total height. Then, the print block is removed, and all the unwanted outer edges are removed to reveal the printed 3D object, as in Figure 2.13.

In sheet lamination, the layer thickness is the same as the thickness of thin sheets of material and dictates the final quality. Layer thickness also depends on the machine and process used.

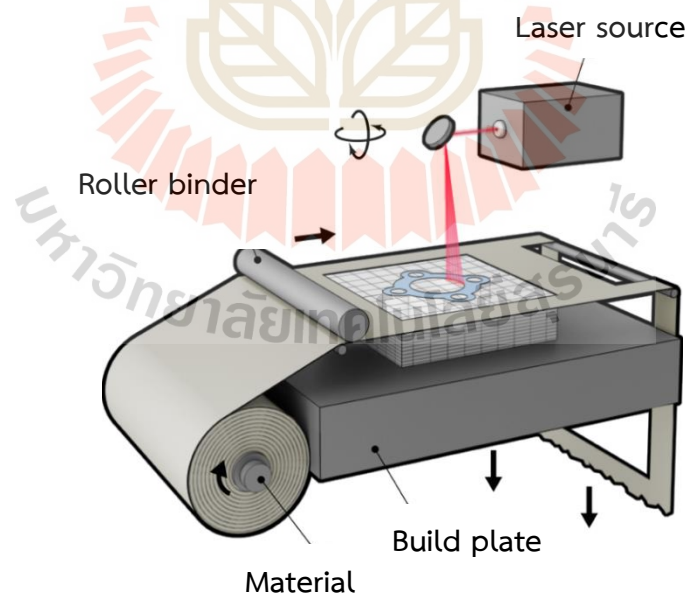


Figure 2.13 Schematic representation of sheet laminate.

Table 2.4 The specification of 3D printing techniques.

3D printing types	Material	Material form	Extrusion	Inkjet	Stereolithography	Laser-assisted
Fused deposition modeling	Thermoplastic, Composite material	Filament, aerogel	Yes	No	No	No
Stereolithography	Photopolymer resin	Liquid	No	No	Yes	Yes
Selective laser sintering	Composites	Powder	No	No	No	Yes
Material jetting	Metal, Waxes, Resin	Powder	Yes	Yes	Yes	No
Binder jetting	Metal, Sand	Powder	No	Yes	No	No
Direct metal sintering	Metal	Powder	No	No	No	Yes
Sheet lamination	Composite	Composit material film	No	No	Yes	No

Table 2.5 The advantage/drawback comparison of 3D printing techniques.

	Extrusion	Inkjet	Stereolithography	Laser-assisted
Advantages	<ul style="list-style-type: none"> - Simple - Capable of various material - Suitable for high viscosity material 	<ul style="list-style-type: none"> - Ability to print low viscosity Materials - Fast fabrication speed - Low cost - High resolution 	<ul style="list-style-type: none"> - Nozzle-free technique - High printing speed - High accuracy 	<ul style="list-style-type: none"> - High resolution - Good for the composite material powder
Drawbacks	<ul style="list-style-type: none"> - Only applicable for viscous liquids 	<ul style="list-style-type: none"> - Poor functionality for vertical structures - Unable to print high-viscosity material 	<ul style="list-style-type: none"> - Only the liquid solution is operated - Not suitable with a high-viscosity material 	<ul style="list-style-type: none"> - Only applicable with powder material - Many post-processing
Printing speed	<ul style="list-style-type: none"> - Slow 	<ul style="list-style-type: none"> - Fast 	<ul style="list-style-type: none"> - Fast 	<ul style="list-style-type: none"> - Fast
Material	<ul style="list-style-type: none"> - Plastic, Aerogel, High viscosity material 	<ul style="list-style-type: none"> - Liquid/metal/polymers 	<ul style="list-style-type: none"> - Liquid resin (Photopolymer) 	<ul style="list-style-type: none"> - Powder/Metal/polymer/composite
Cost	<ul style="list-style-type: none"> - Moderate 	<ul style="list-style-type: none"> - High 	<ul style="list-style-type: none"> - Low 	<ul style="list-style-type: none"> - High
Vertical printing ability	<ul style="list-style-type: none"> - Good 	<ul style="list-style-type: none"> - Poor 	<ul style="list-style-type: none"> - Good 	<ul style="list-style-type: none"> - Good
Resolution	<ul style="list-style-type: none"> - 100 μm 	<ul style="list-style-type: none"> - 50 μm 	<ul style="list-style-type: none"> - 25 μm 	<ul style="list-style-type: none"> - 10 μm

2.3.2 The fabrication of convention and 3D printing of supercapacitor electrode

Preparing the supercapacitor electrode on a lab scale

The commercial supercapacitor electrode comprises three components: activated carbon, carbon black, and a polyvinylidene fluoride binder, formed as a layer on a conductive-carbon coated aluminum foil current collector. The fabrication process for the commercial supercapacitor is shown in Figure 2.14, and the example is shown in Figure 2.15.

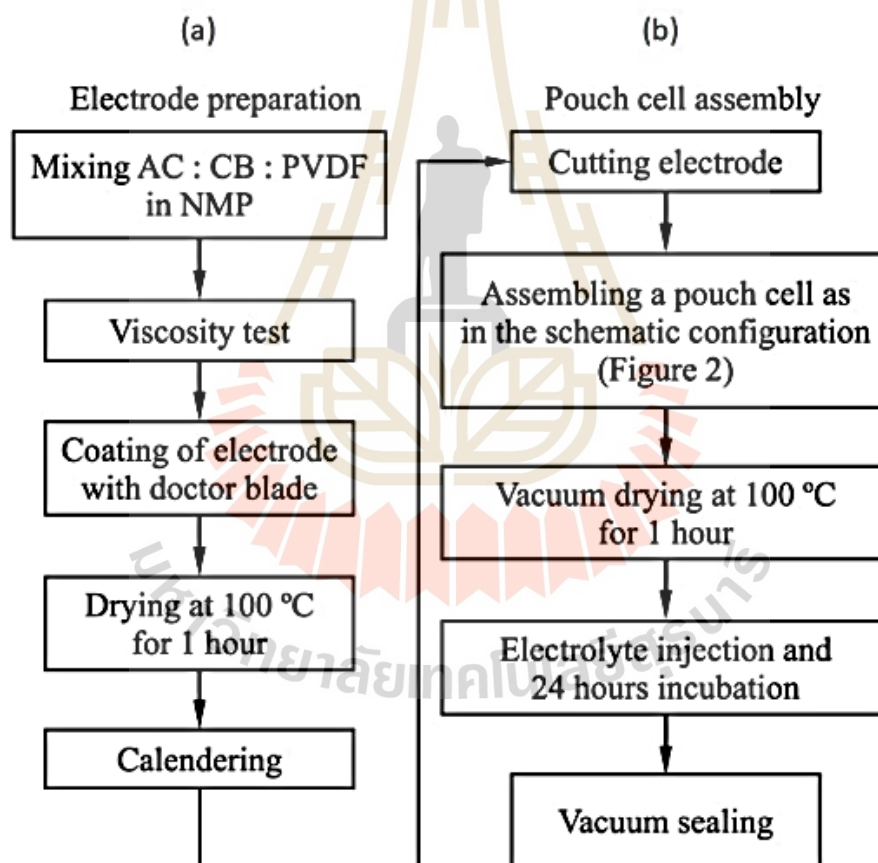


Figure 2.14 The flow chart of pouch cell supercapacitor fabrication: (a) electrode preparation and (b) pouch cell assembly (Safitri *et al.*, 2020).

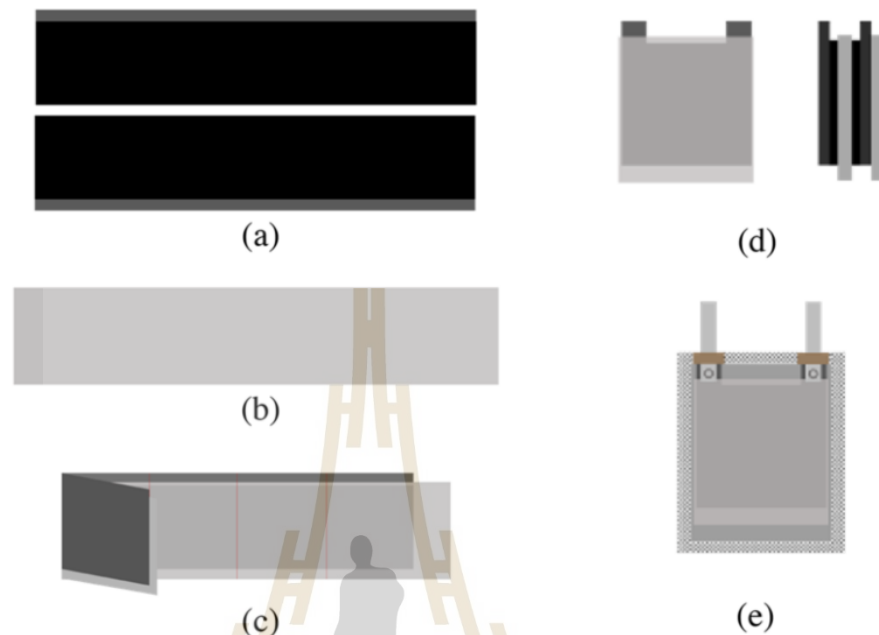


Figure 2.15 The components layout of a pouch cell supercapacitor: (a) carbon-coated electrodes, (b) a separator, (c) a stack of electrodes and separators, (d) front-view (left) and side view (right) of a rolled cell, and (e) an assembled pouch cell (Safitri *et al.*, 2020).

As the fabrication of a commercial supercapacitor, the mixing of activated carbon (AC), carbon black (CB), and polyvinylidene fluoride (PVDF) in a solvent N-Methylpyrrolidone (NMP), and then the carbon slurry was spread onto a sheet of current collector with a doctor blade device producing carbon film. The coated material on the electrode is dried in an oven and prepared for the pouch cell assembly.

In fabricating pouch cell supercapacitors, the coated material forms a two-dimensional pattern. The ion exchange rate occurs near the surface of the electrode and electrolyte, which impacts the capacitance.

Typically, aluminum foil, copper foil, and nickel foam are widely used to fabricate supercapacitors in a laboratory by coating the surface with active materials such as activated carbon, graphene, and carbon-based material. The following is a conventional method for fabricating a supercapacitor in a laboratory setting.

Materials:

- Electrode material (such as activated carbon or metal oxides)
- Conductive additives (such as carbon black or graphite)
- Binder (such as polyvinylidene fluoride or sodium carboxymethyl cellulose)
- Electrolyte solution (such as potassium hydroxide or sulfuric acid)
- Current collector (such as aluminum foil, copper foil, or nickel foam)

Equipment:

- Doctor blade machine
- Oven or hotplate
- Hydraulic press

Procedure:

Preparation of active material: The active material is typically prepared by mixing the electrode material, conductive additive, and binder in a solvent. The binder must hold the active material onto the nickel foam substrate. The mixture is then sonicated or stirred to ensure the components' homogeneous dispersion.

Coating the active material on substrate: The prepared active material and binder mixture are coated onto the nickel foam substrate by a drop coating or doctor blade. This coating method of active material can control the active material film thickness.

Drying the Coated Film: The active material coated on the substrate is dried in an oven to remove the solvent and binder and solidify the active material on the substrate.

Hydraulic Pressing: After drying, the coated active material is pressed with hydraulic pressure to improve performance. The pressure typically ranges from 5 to 10 MPa, and the pressing time can vary from a few seconds to several minutes. The pressing helps increase the contact between the active material and the nickel foam, improving the overall performance of the supercapacitor.

2.4 3D printing of supercapacitor electrode

As the conventional fabrication of supercapacitors is limited to a 2D structure, the key performance of supercapacitors depends on the surface area of the electrode. Therefore, researchers are focusing on studying the electrode structure such as Yao Bin and his colleague demonstrated a 3D-printed graphene aerogel electrode with MnO₂ loading of 182.2 mg/cm² shown Figure 2.16, which achieves a record-high areal capacitance of 44.13 F/cm², the areal capacitance is increased and the gravimetric capacitance remains unchanged as the MnO₂ loading increases (Yao *et al.*, 2019). Teng *et al.*, 2013, have developed an effective and simple strategy to prepare large areal mass loading of MnO₂ (0.31-13.6 mg/cm²) on 3D porous nickel foam as an electrode. 3D MnO₂/G-gel/NF has a large areal capacitance of 3.18 F/cm² (234.2 F/g). Teng *et al.*, 2015, demonstrated the ultralight highly conductive 3D graphene hollow (3DGH) of V₃S₄ and MnO₂ as anode and cathode materials, respectively. A quasi-solid-state has an energy density of 7.4 Wh/kg at an average density of 3,000 W/kg. 3DGH enhanced the effective surface area and charge transport of electrodes and increased the mass ratio of active material to the current collector. He *et al.*, 2012, reported a graphene/MnO₂ coated free-standing, flexible Ni foam. The CVD process deposits graphene on Ni foam, and MnO₂ is deposited on graphene/Ni foam via electrodeposition. The thickness of MnO₂ varies by the deposition time. This 3D flexible supercapacitor exhibits an energy density of 6.8 Wh/kg at power density of 62 W/kg for 1V window voltage, with a high areal capacitance of 1.42 F/cm².

Numerous research studies have shown the advantages of 3D electrodes over conventional bulk electrodes in increasing the electrode surface area. Moreover, some research exhibits high capacitance with high mass loading on the 3D electrodes, which is impossible for conventional bulk electrodes. Table 2.6 shows the materials and fabrication of 3D electrodes.

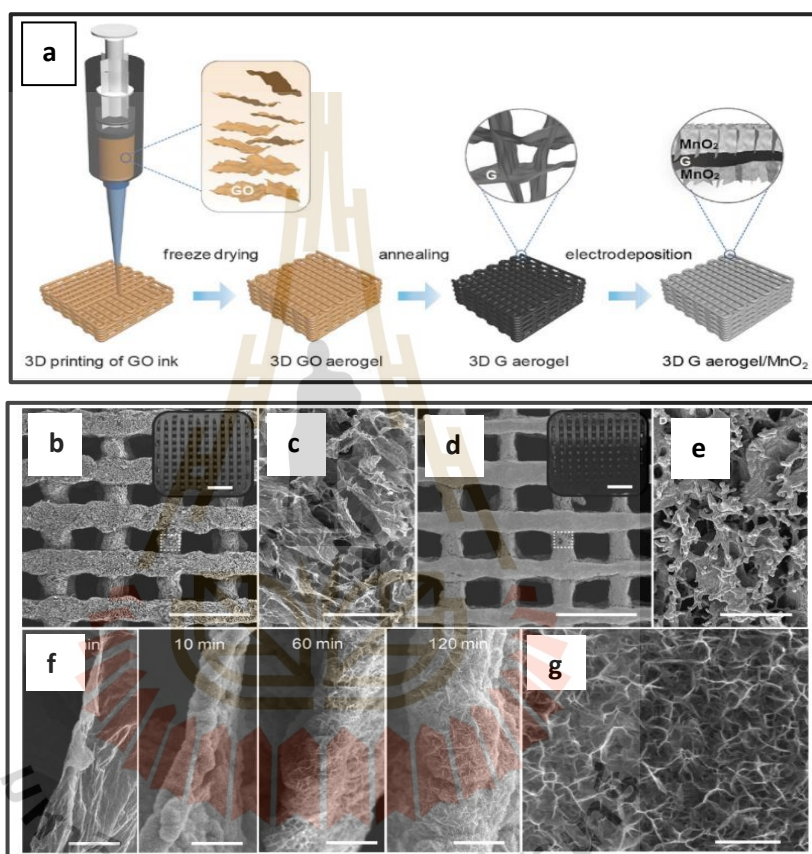


Figure 2.16 a) The illustration of 3D-printed graphene aerogel fabrication. b) SEM image of 3D-printed graphene aerogel, scale bar 1 mm. c) The magnified SEM image of the cylindrical rod highlighted in (b), scale bar 40 μm . d) SEM image of 3D-printed graphene aerogel electrodeposition with MnO_2 , scale bar 1 mm. e) The magnified SEM image of cylindrical rod highlighted in (d), scale bar 40 μm . f) SEM image of the edge of 3D-printed graphene aerogel at different electrodeposition times of MnO_2 , scale bar 2 μm . g) SEM image of MnO_2 nanosheet on 3D-printed graphene aerogel, scale bar 200 nm (Yao *et al.*, 2019).

Table 2.6 The comparison of 3D electrode performance.

Electrode description	Fabrication methods	Mass loading	Capacitance	Ref.
Nanostructure MnO ₂	Non-templating	2-3 mg/ cm ²	110 F/g at 1A/g	Chen <i>et al.</i> , 2014
MnO ₂ -NiO nanoflake	Non-templating	3 mg/ cm ²	0.101 F/cm ²	Liu <i>et al.</i> , 2012
Co ₃ O ₄ nanowire@ MnO ₂ nanosheets	Non templating	1.5 mg/ cm ²	480 F/g at 2.67 A/g	Liu <i>et al.</i> , 2011
3D nanoporous NiO	Non templating	-	1,176 F/g at 1mV/S	Chen <i>et al.</i> , 2009
3D graphene/Co ₃ O ₄ nanowire composite	Nickel foam templating	-	1,100 F/g at 10A/g	Dong <i>et al.</i> , 2012
MnO ₂ coated freestanding 3D graphene foam	Nickel foam templating	0.85-9.80 mg/ cm ²	1.42 F/cm ² at 2mV/S	He <i>et al.</i> , 2013
3D graphene/CNFs/ MnO ₂ composite	Nickel foam templating	0.1 mg/ cm ²	946 F/g at 2mV/S	He <i>et al.</i> , 2014
MnO ₂ /3DGH	Nickel foam templating	-	345 F/g at 10A/g	Zhai <i>et al.</i> , 2015
ZnO@Co ₃ O ₄	Nickel foam templating	2.0 mg/ cm ²	857.7 F/g at 1 A/g	Cai <i>et al.</i> , 2014

Table 2.6 The comparison of 3D electrode performances (Continued).

Electrode description	Fabrication methods	Mass loading	Capacitance	Ref.
Ultrathin mesopores Ni Co ₂ O ₄ nanosheets	Nickel foam templating	0.4 mg/ cm ²	1,450 F/g at 20 A/g	Yuan <i>et al.</i> , 2012
MnO ₂ @RGO	3D printing	182.2 mg/ cm ²	242.19 F/g	Bin <i>et al.</i> , 2015
GO	3D printing	-	21.0 F/cm ²	Shangwen <i>et al.</i> , 2019
Graphene	3D printing	-	102 F/g	Altin <i>et al.</i> , 2019

Many researchers have demonstrated the potential of 3D printing for fabricating complex supercapacitor electrodes with controllable geometries and tailored properties. However, some challenges remain, such as optimizing the ink formulation and printing parameters for better performance. Moreover, commercial 3D printers for this research are expensive, and only high-budget laboratories can access them. Therefore, the development of 3D printing for supercapacitors can address this issue.

2.5 Electrochemical measurements

Typically, electrodes' electrochemical performance is defined as their capacitance (F/g, F/cm², F/cm³) and energy/power density (Wh/kg and W/kg). This method typically measures the material's electrochemical properties, such as cyclic voltammetry, galvanostatic charge/discharge, and electrochemical impedance spectroscopy.

2.5.1 Cyclic voltammetry (CV)

Cyclic voltammetry is widely used to measure the electrochemical properties of electrode material. The potential is applied to the electrode, scanned between two electrodes, and the current is measured. The voltage scans reverse when reaching the limit to complete the cycle. The measurement result can be plotted between two parameters: the current at the electrode and the applied voltage, which is the cyclic voltammetry (CV). For the ideal EDLC electrode, the CV curve is rectangular. For pseudocapacitors, the CV curve is different from EDLC and shows the redox reaction peak, which is the capacitance as pseudocapacitance. The CV of EDLC and pseudocapacitor is shown in Figure 2.17. The capacitance of an ideal supercapacitor can be calculated by equation (2.3).

$$\frac{dq}{dt} = C \left(\frac{dV}{dt} \right)$$

$$C = \frac{I}{v} \quad (2.3)$$

Where dq/dt is the current I and dV/dt is the scan rate (v)

In the experimental, the specific capacitance can be calculated according to equations (2.4) or (2.5):

$$\text{Gravimetric capacitance} \quad C_{cv} = \frac{1}{mv\Delta V} \int I(V)dV \quad (2.4)$$

$$C_{cv} = \frac{1}{m\Delta V} \int I(t)dt \quad (2.5)$$

$$\text{Areal capacitance} \quad C_{cv} = \frac{1}{Av\Delta V} \int I(V)dV \quad (2.6)$$

$$C_{cv} = \frac{1}{A\Delta V} \int I(t)dt \quad (2.7)$$

Where term $\int I(V)dV$ and $\int I(t)dt$ refer to the area around the CV curve and discharge curve, m is the mass of the activated material (g), A is the geometric electrode working area (cm^2), ν is the scan rate (mV/s), and ΔV is the voltage window (V).

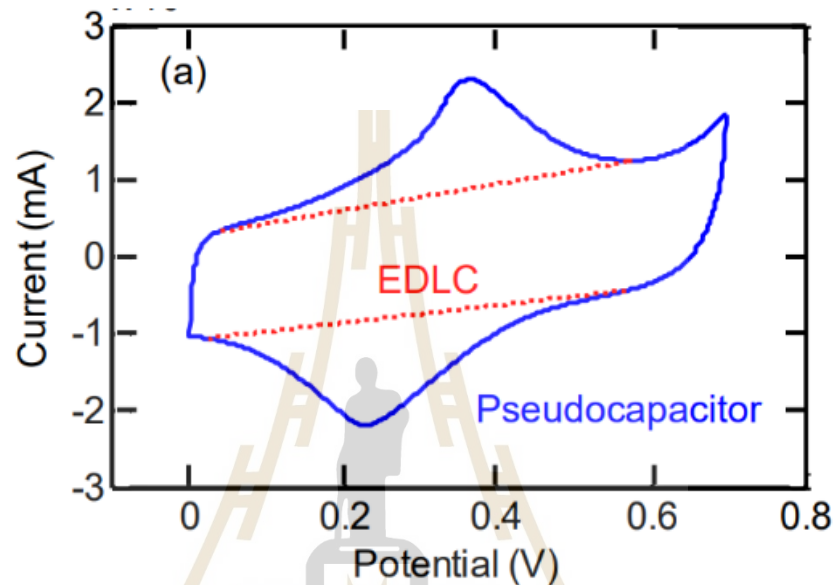


Figure 2.17 Cyclic Voltammograms showing rectangular features for an EDLC system and superimposed reduction and oxidation peaks for a redox active pseudocapacitor (Achilleos *et al.*, 2014).

2.5.2 Galvanostatic charge/discharge testing (GCD)

A GCD test is the most efficient measurement for the evaluation of the capacitance and cycle life of the supercapacitor. The GCD measurement is performed by controlling the current and voltage vs time during the charging and discharging process, shown Figure 2.18. For the ideal capacitor, the charge and discharge curves are linear and symmetrical at various currents. The basic equation (2.8) can estimate the capacitance from the discharge curve.

$$C = \frac{I\Delta t}{\Delta V} \quad (2.8)$$

The specific capacitance with mass m of electrode materials can be calculated by:

$$C = \frac{I\Delta t}{m\Delta V} \quad (2.9)$$

Where I is the discharge current (A), m is the mass of active material (g), ΔV is the potential during the discharge process (V), and Δt is the discharge time (S).

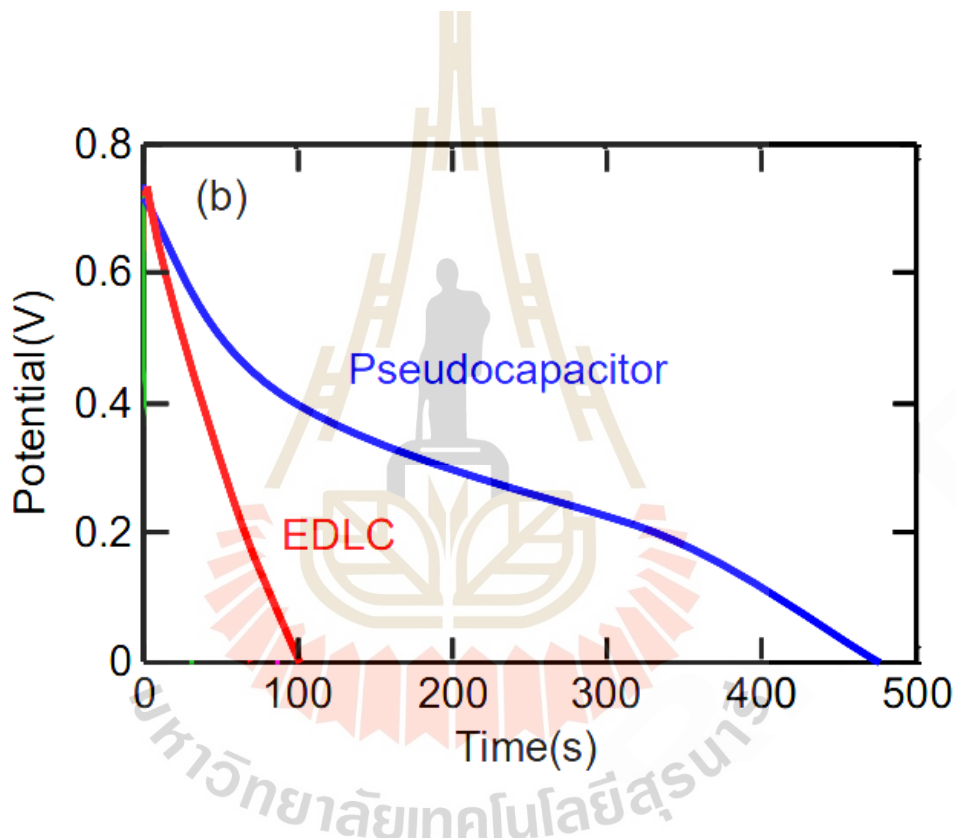


Figure 2.18 Discharge curves for an EDLC and a pseudocapacitor. The EDLC shows a constant pseudocapacitor discharge rate, which depends on the potential-dependent redox reaction rate (Achilleos *et al.*, 2014).

2.5.3 Electrochemical impedance spectroscopy (EIS)

EIS is a frequency domain technique to characterize energy storage. In this technique, the system is performed using a small voltage amplitude of 5 or 10 mV, applying the frequency of an AC signal from 0.01 Hz to 100 kHz. The corresponding

sinusoidal current and voltage signal ratio provide the complex impedance with a particular frequency. In a capacitor, the current lags voltage (less angle than voltage) by an angle(ϕ). The ϕ is 90° for the ideal capacitor when the applied voltage is

$$V(\omega) = V_0 e^{j\omega t} \quad (2.10)$$

The current will be

$$I(\omega) = I_0 e^{(\omega t + \phi)} \quad (2.11)$$

where the V_0 and I_0 are the maximum amplitude of voltage and current signal. The electrochemical impedance can be estimated by the following equation:

$$Z = \frac{V(\omega)}{I(\omega)} = \frac{V_0}{I_0} e^{-j\phi} \quad (2.12)$$

The complex impedance is defined as:

$$|Z| = Z' + (Z'') \quad (2.13)$$

Where Z' and Z'' are the real and imaginary parts of the impedance, respectively. The modulus ($|Z|$) and the phase angle (ϕ) are defined as

$$|Z| = \sqrt{(Z')^2 + (Z'')^2} \quad (2.14)$$

$$\phi = \tan^{-1} \left(\frac{Z''}{Z'} \right) \quad (2.15)$$

Typically, the EIS data analysis of supercapacitors can be represented with two plots: the Nyquist plot and the Bode plot. The Nyquist plot is the plot of the opposite imaginary part impedance ($-Z''$) versus the real part impedance (Z'). In contrast, the logarithm of the impedance (Z) or phase angle (ϕ) versus the logarithm of the frequency is the Bode plot. For the ideal EDLC, the Nyquist plot will be a vertical line containing only the EDLC as presented in Figure 2.19 (a) and (b); the Nyquist plot consists of the three regions. The intercept at the real part axis (Z') at high frequency presents an Ohmic resistance (R_s), the sum of the current collector and bulk electrolyte

resistances. The charge transfer resistance (R_{ct}) corresponds to the diameter of the semi-circle at a high frequency region. The linear part over low frequency refers to the Warburg resistance (R_w), which is employed to explain the diffusion of ions into the surface of the electrode.

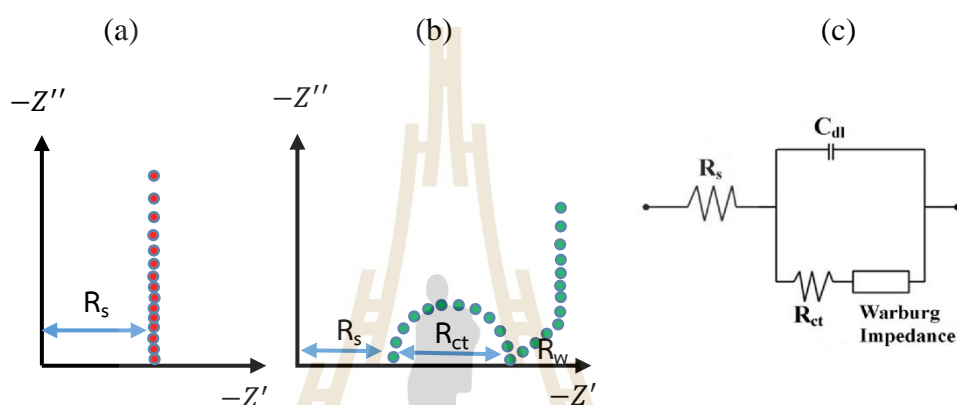


Figure 2.19 Nyquist plot of EDLC a) Ideal, b) Ordinary, and c) Basic equivalent circuit of EDLC.

2.6 Summary

In Chapter II, the first section describes electrochemical capacitors and supercapacitors, as well as the mechanism of each type of supercapacitor that occurs at the surface of the electrode/electrolyte. The surface area of a supercapacitor is one of the main factors that enhance its performance. PANI is a pseudocapacitive material through which ion transfer occurs via a redox reaction. Moreover, PANI has a nanofibrous network morphology. 3D printing technology offers a possible way to fabricate the electrode in a 3D micro-structure.

Since the surface area of conventional supercapacitor electrodes is limited by the available surface area and their thickness, they cannot store as much energy for a given volume or weight, resulting in low power and energy density. To address this research gap, new electrode structures and materials must be developed to achieve a high surface area. 3D printing technology is a candidate for creating complex

structured electrodes to increase the surface area. Chapter III will describe the process and methods for developing 3D printing for supercapacitor electrodes (research objectives 1 and 2), the synthesis of PANI, material characterization (research objective 3), and electrochemical measurement (research objective 4).



CHAPTER III

METHODOLOGY

Four main steps will be taken to address the hypothesis of this thesis: 1) develop a 3-D printing machine, 2) The ink preparation and print testing, 3) polyaniline (PANI) synthesis and deposition, and 4) characterization of 3D-printed supercapacitor electrode. The first section will present the 3D printing development and setup used in this work, starting with an enumeration of each component and then the specific part of the development. The second section will provide the ink selection and conditions for this work. The third section will present PANI preparation as the active material and coating method. The last section is the characterization of reduced graphene oxide/polyaniline (rGO/PANI) 3D printing supercapacitor electrode.

HYPOTHESIS (H1): Extruded 3D printing method is suitable for the 3D-printed electrode because the materials must be prepared in high viscosity ink. Three type of extruder 3D printing techniques are considered, the pneumatic 3D printing system is one of candidate to develop for the small amounts of material.

3.1 3D printing development

To prove the hypothesis, the initial phase of the experiment focuses on developing a 3D printing process for the material, utilizing ink with high viscosity. Subsequently, the printed electrodes are subjected to material characterization and measurement of electrochemical properties for further investigation.

OBJECTIVE 1: To design and develop a 3D printer for fabrication of supercapacitor electrodes

As described in chapter II, 3D printing technology can be classified into 7 types. Each type offers different advantages and is suited for specific applications. For the fabrication of 3D-printed supercapacitor electrodes, the development based on FDM techniques is the most suitable in this work.

In this thesis, the development of a 3D printer for supercapacitors is based on the BLV mgn12 modified by Levi, an open-source project. However, this work focuses on the extruder system, which was designed with significant deviations from the original project. The details about the extrusion system will be provided in the next topic.

The main components of FDM 3D printing include 1) frame, 2) build platform/print bed, 3) extruder, 4) control board, 5) step motor, 6) power supply, 7) cooling fan, and 8) LCD. These components are shown in Figure 3.1.

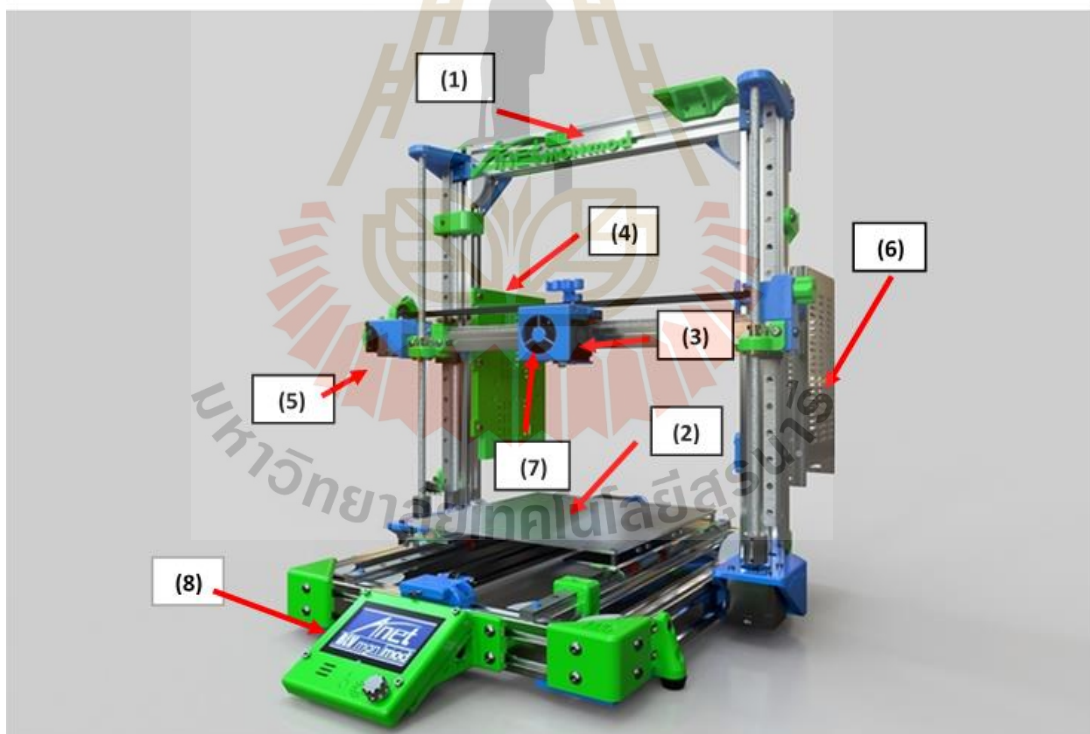


Figure 3.1 Schematic of the conventional FDM 3D printer, which has main components consisting of (1) frame, (2) build platform/print bed, (3) extruder, (4) controller board, (5) stepper motor, (6) power supply, (7) cooling fan, and (8) LCD.

3.1.1 3D printer components

1) Frame

The Cartesian FDM is based on the Cartesian coordinate system in mathematics; therefore, the frame is the normal XYZ system, which holds all other components together. In this study, aluminium profiles 2020 and 2040 were selected, with machine dimensions of 350×400×500 mm³. The design uses two Nema 17 stepper motors along the Z-axis. The frame can be adjusted from a few centimeters up to a meter, depending on the application.



Figure 3.2 Schematic of conventional FDM 3D printer frame.

2) Build a platform/print bed

The print bed is a fundamental component that provides the proper surface for printing. Usually, the print bed is made from an alumina plate connected to a heater located underneath. The heater heats the build plate to a temperature of about 50°C to 100°C, ensuring good adhesion of the first layer during printing. However, for 3D-printed supercapacitors, the heated function of the print bed can be turned off because the printed material is already mixed with a binder and can adhere well on its own. In some cases, a glass plate covers the print bed, making it easier to remove the printed object once the print job is finished.

In this thesis, the MK2B dual power heat bed, shown in Figure 3.3, is selected. It is a PCB heat bed with a circuit pattern embedded within the plate, which exhibits resistance when a constant voltage of either 12V or 24V is applied. This resistance leads to the occurrence of heat through the Joule effect, by Joule's law. The temperature range can be adjusted from 25°C to 100°C.

Joule's law $Q = I^2Rt$

Where Q is the amount of heat in Joules (J).

I is the electric current that flows through the wire in amperes (A).

R is the value of the electrical resistance of the wire in ohms (R).

t is the time that current passes through the wire in seconds (s).

This heat is directly proportional to 1) the square of the current, 2) the resistance of the wire, and 3) the time the current flows through the wire.



Figure 3.3 The MK2B dual power heat bed.

3) Extruder

The extruder is a vital component of a 3D printing system that functions to feed the material, as in Figure 3.4. Typically, the material is fed in regular FDM printers using a step motor drive through a heated nozzle. The melted material is extruded from the nozzle and deposited onto the print bed or the previous printed layer, which quickly dries and solidifies.

However, for our specific work, we utilize a paste-like material prepared from an active substance. Consequently, we require a different extruder system than regular FDM printers. The next topic will provide further details about this.

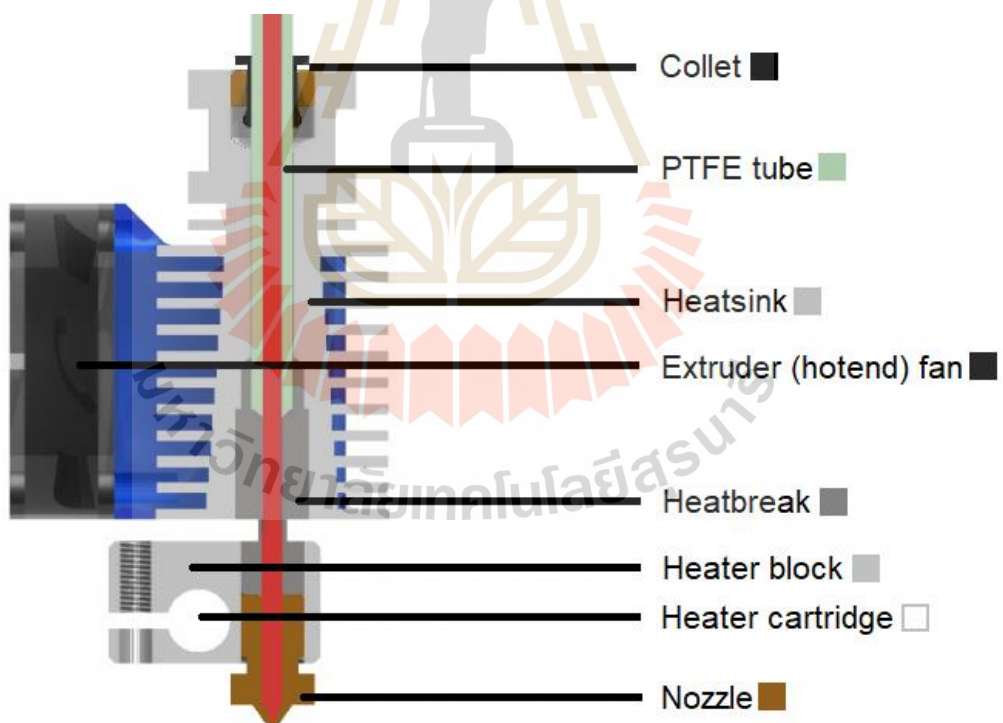


Figure 3.4 The schematic of the E3D extruder, the most popular extruder for FDM 3D printers. (Image courtesy of E3D).

4) Controller board

The controller board serves as the central control unit of the 3D printer. It receives commands from the slicer program and controls the movement of the printer's axes, executing the corresponding code and functions for each part. There are various types and commercial brands of controller boards available.

For this work, we utilize the Arduino Mega 2560 as the controller board and the RAMPS 1.4 shield, as shown in Figure 3.5. Further details will be provided in the next topic.

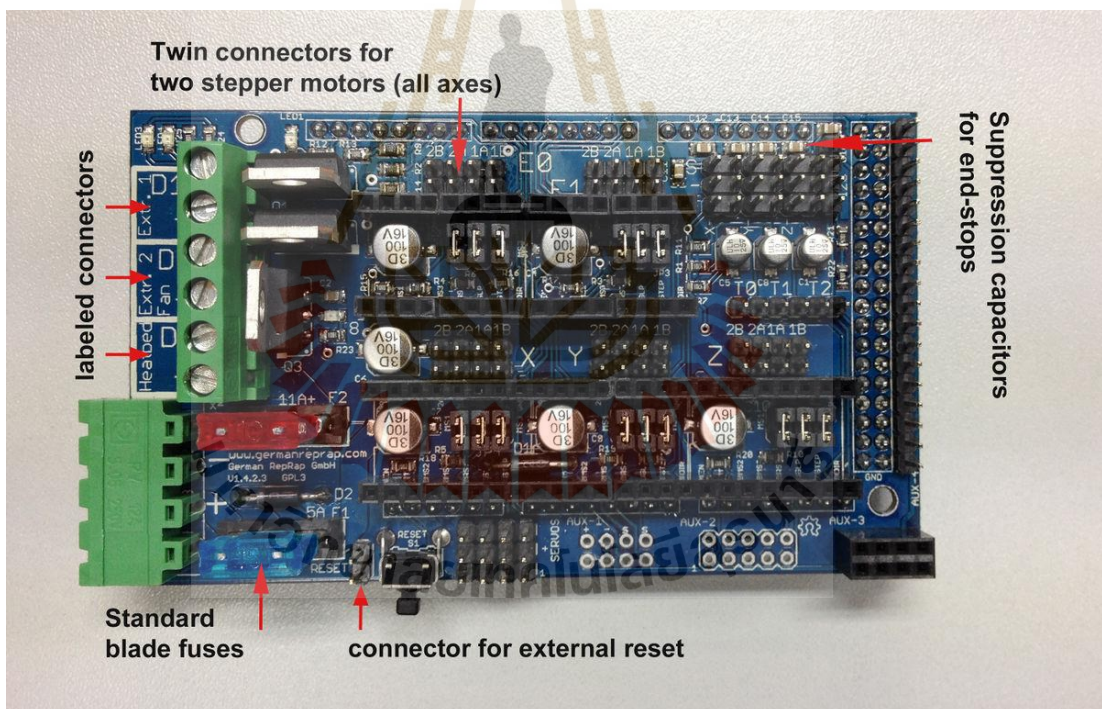


Figure 3.5 RAMPS 1.4 shield, 3D printer controller board (Credit: RepRap.org).

5) Stepper motor

Stepper motors play an important role in accurately and precisely moving the filament feeder, print head, and build plate based on the coordinate instructions from G-code. The Nema 17 stepper motor is commonly used in FDM printers. The term 'Nema 17' refers to the motor's standard size and mounting dimensions, as in Figure 3.6a. Typically, a stepper motor has a step angle of 1.8 degrees per step, requiring 200 steps to complete one revolution or cycle. For finer steps, a stepper driver can provide a tiny angle of the revolution for each step.

This thesis uses the micro stepper driver TMC2209, which offers 256 micro steps, as shown in Figure 3.6b. This means that the highest precision achievable is $1.8/256$ degrees or approximately 0.007 degrees, enabling exact motor control and resulting in smoother and quieter prints. While one stepper motor is generally sufficient for moving the nozzle or print bed, multiple stepper motors can be used per axis, depending on the design. For example, six stepper motors are utilized in a 3D printing core XY system.

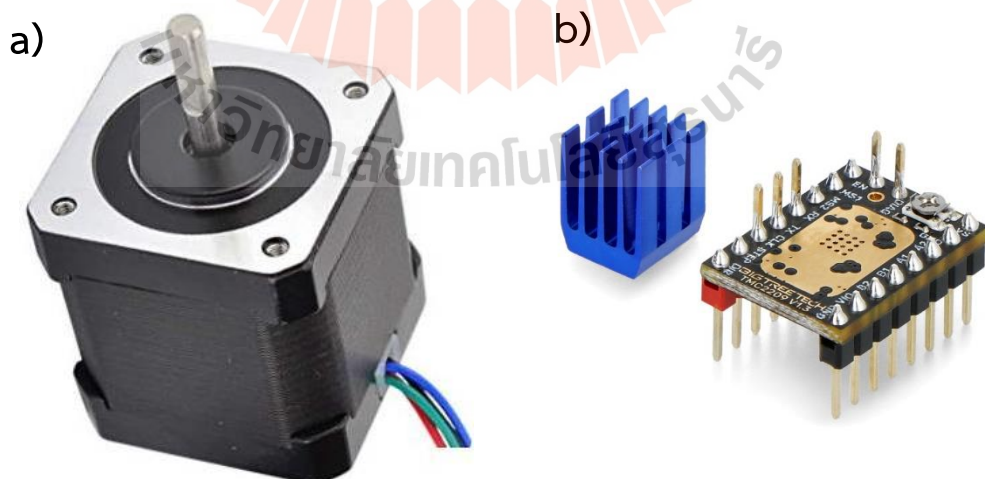


Figure 3.6 a) Nema 17 stepper motor. b) micro stepper motor driver TMC 2209.

6) Power supply

The power supply converts 220V AC electricity to either 12V or 24V DC to power the electrical components of the 3D printer. It is crucial to ensure that the power supply can adequately cover the power requirements of all components. Typically, a power supply with a capacity that exceeds 30% of the total power consumption is chosen for improved stability and safety during printer operation. Our work uses a Meanwell RSP-500-24DC power supply, which provides 500 watts of power at 24V DC, as shown in Figure 3.7.



Figure 3.7 Meanwell RSP-500-24DC power supply.

7) Cooling fan

Cooling fans play a vital role in 3D printing, preventing warping, overheating, and nozzle clogging, ensuring print stability and high-quality results. The cooling fan is in the schematic of Figure 3.4. These fans aid in the rapid solidification of the melted filament, resulting in excellent print quality. However, the cooling function is unnecessary in this work, where materials such as paste, ink, or gel are used. Therefore, the cooling function can be omitted from the machine.

8) LCD

The LCD serves as a monitoring tool for the machine, providing a user-friendly interface to control various aspects of the printer, as in Figure 3.8. It displays important information such as nozzle temperature, print bed temperature, and printing time. Additionally, the buttons on the display allow users to access command functions and make live adjustments during operation.

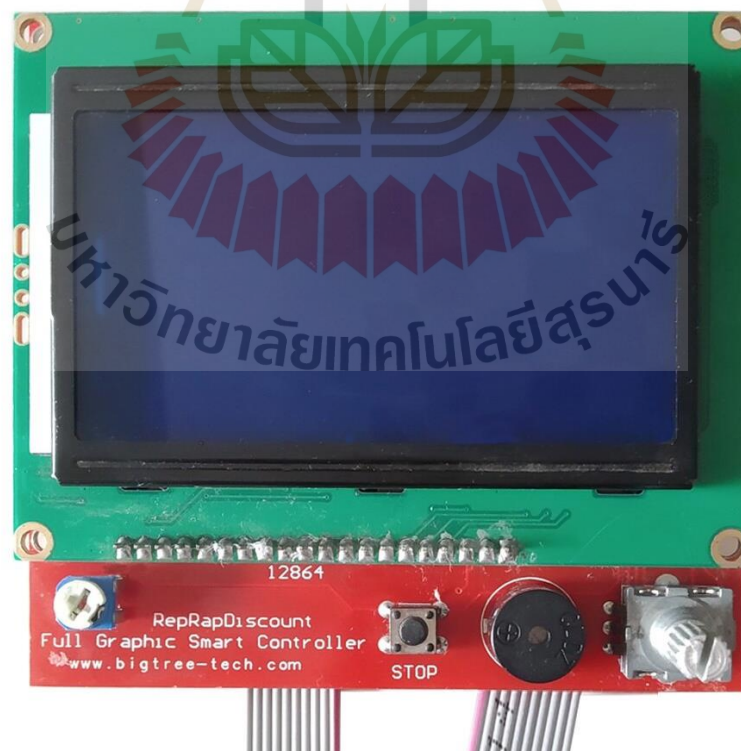


Figure 3.8 12864 LCD for 3D printer (Credit: RepRap.org)

3.1.2 General materials for building a 3D printer

Frame and Structure:

- Extruded aluminum profiles (typically 20x20 mm or 20x40 mm)
- Corner brackets and joining plates for the frame
- Mounting hardware (screws, nuts, T-nuts, etc.) for assembly

Linear Motion:

- MGN12 linear rails and linear carriage blocks
- Mounting brackets for the linear rails
- M3 or M4 screws and nuts for securing the rails and carriage blocks

Electronics and Control:

- 3D printer controller board: Arduino Mega 256, RAMPS 1.4 shield
- Stepper motors: NEMA 17
- Stepper motor drivers: TMC 2209
- Wiring and connectors
- Power supply: Meanwell RSP-500-24DC
- End stops (limit switches): for XYZ axes
- Heated bed

Extruder and Hot end:

- 10 ml syringe
- Air pump connector
- Air pressure regulator

Mechanic Components:

- Z-axis lead screw and nut
- Belts and pulleys

The process of developing a 3D printer for supercapacitors can be depicted in Figure 3.9. In this process, the primary focus is developing the extruder system, which involves considering and developing extruders.

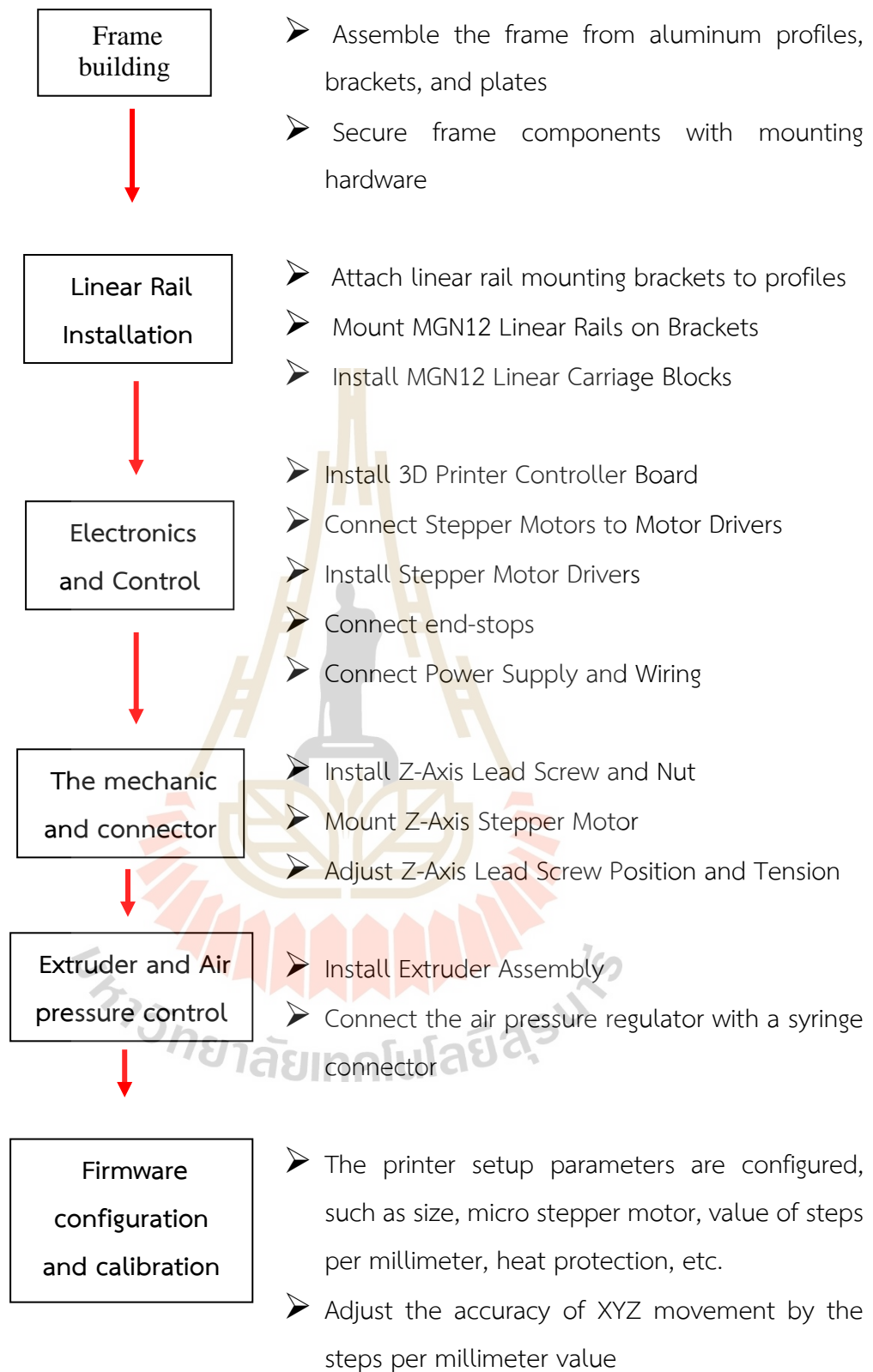


Figure 3.9 The flowchart of the 3D printer for the supercapacitor process.

3.1.3 The electronic wiring

After the assembly of the mechanical parts, the next step in the process is the electronic and wiring setup. The controller board used in this work is the Arduino Mega 256 + Ramps 1.4 shield, as illustrated in Figure 3.10.

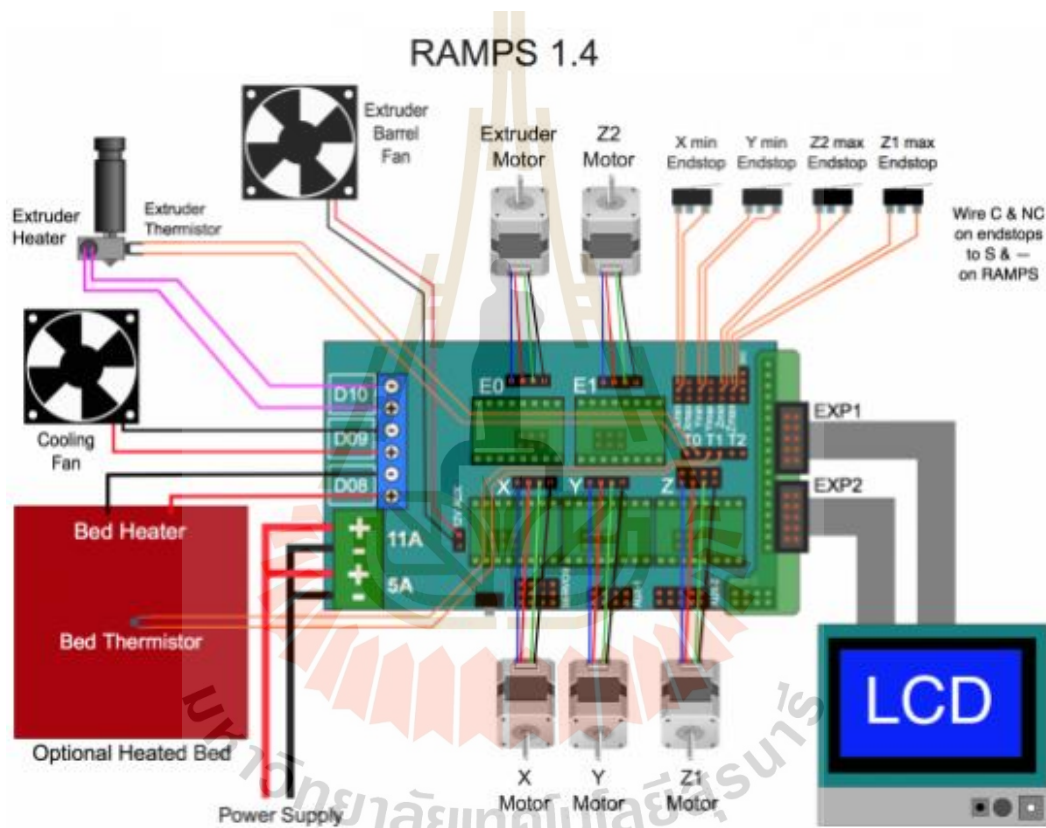


Figure 3.10 The electrical wiring diagrams for RAMPS 1.4 (Reference from reprap.org).

3.1.4 Firmware configuration

The Open-source Marlin firmware is widely used in 3D printing, including commercial 3D printers from brands such as Anet, Prusa, and Creality. The firmware is compatible with Cartesian and Delta 3D printer types. Marlin is released under the GNU General Public License (GPL), which means its source code is freely available for

modification and distribution. This allows the 3D printing community to contribute to its development and enhance its functionality.

This section provides the main parameters for configuring Marlin firmware, including the type of electronics, temperature sensor, printer geometry, and end-stop configuration, as presented in Figure 3.11. The selection of these parameters depends on the specific design and characteristics of the 3D printer. This work presents the main parameters considered for the given design.



```

Configuration - Notepad
File Edit Format View Help
// This will remove the need to poll the interrupt pins, saving many CPU cycles.
#define ENDSTOP_INTERRUPTS_FEATURE

//=====
//===== Movement Settings =====
//=====
// @section motion

/**
 * Default Settings
 *
 * These settings can be reset by M502
 *
 * Note that if EEPROM is enabled, saved values will override these.
 */

/**
 * With this option each E stepper can have its own factors for the
 * following movement settings. If fewer factors are given than the
 * total number of extruders, the last value applies to the rest.
 */
#define DISTINCT_E_FACTORS

/**
 * Default Axis Steps Per Unit (steps/mm)
 * Override with M92
 *
 * X, Y, Z, E0 [, E1[, E2[, E3[, E4]]]]
 */
#define DEFAULT_AXIS_STEPS_PER_UNIT { 160, 160, 6300, 567 }

/**
 * Default Max Feed Rate (mm/s)
 * Override with M203
 *
 * X, Y, Z, E0 [, E1[, E2[, E3[, E4]]]]
 */
#define DEFAULT_MAX_FEEDRATE { 400, 400, 3, 50 }

/**
 * Default Max Acceleration (change/s) change = mm/s
 * (Maximum start speed for accelerated moves)
 * Override with M201

```

Figure 3.11 The illustration of Marlin firmware configuration.

Movement Settings

- #Axis Steps Per Unit (steps/mm) : { 80, 80, 400, 95 }
- #Max Feed Rate (mm/s): { 200, 200, 15, 25 }
- #Max Acceleration (change/s) change = mm/s: { 3000, 3000, 100, 5000 }
- #Jerk (mm/s) : 10.0

Endstop Settings

- #define USE_XMIN_PLUG
- #define USE_YMIN_PLUG
- #define USE_ZMIN_PLUG

Thermal Settings

- #HEATER_MINTEMP: 170
- #HEATER_MAXTEMP: 240
- #BED_MINTEMP: 0
- #BED_MAXTEMP: 100

Extruder

- #PREVENT_COLD_EXTRUSION: 5
- #EXTRUDE_MINTEMP: 170

Thermal Runaway Protection

- #THERMAL_PROTECTION_HOTENDS
- #THERMAL_PROTECTION_BED

The size of the print bed

- #X_BED_SIZE: 200
- #Y_BED_SIZE : 200

Travel limits (mm) (Travel limits (mm) after homing, corresponding to end stop positions.)

- #X_MIN_POS: 0
- #Y_MIN_POS: -20
- #Z_MIN_POS: 0
- #X_MAX_POS X_BED_SIZE: 200
- #Y_MAX_POS Y_BED_SIZE: 200
- #Z_MAX_POS: 300
-

In the initial stage of developing the 3D printing system, the decision was made to use an FDM 3D printer for construction, as in Figure 3.12. Subsequently, the printer was tested by printing an object after completing the building process.

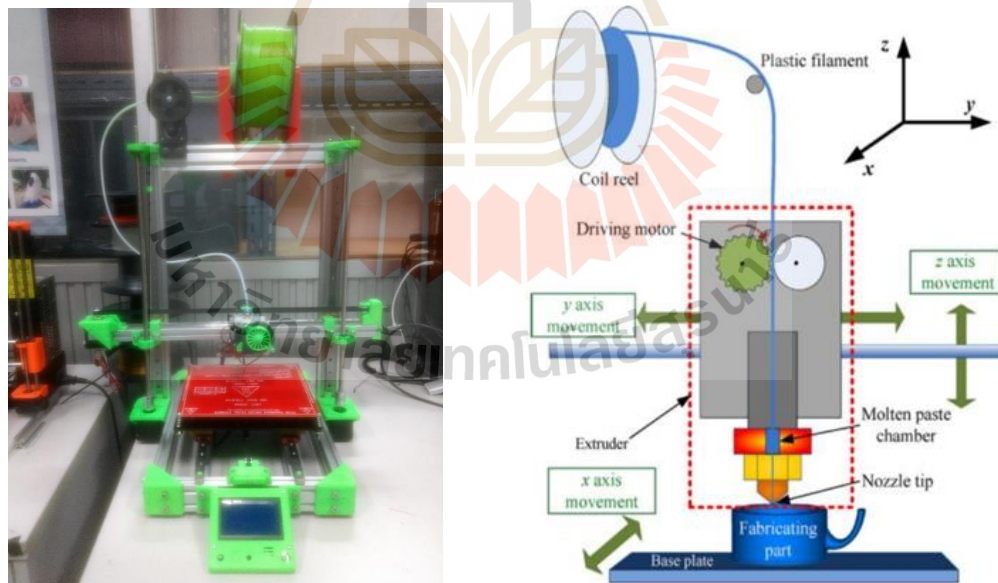


Figure 3.12 a) Shows the initial version of the constructed FDM 3D printer. This printer underwent testing for printing accuracy and calibration by printing a reference cube. b) Schematic of fused deposition modeling component (Jin *et al.*, 2015).

3.1.5 The print accuracy testing

For print accuracy testing, the printed object is measured and compared to the scale of the model in the CAD file. Typically, a cube with a known scale is used as the reference model, as shown in Figure 3.13. If the measured printed scale differs from the CAD model, the 'Axis Steps Per Unit values (steps/mm) ' in the configuration file of the Marlin firmware must be adjusted to compensate for the disparity.



Figure 3.13 The reference cube model for the movement calibration.

3.1.6 The extruder development

The key distinction between conventional FDM 3D printers and direct ink writing lies in the extruder system. This section focuses on developing and replacing the original FDM 3D printer extruder with a DIW extruder. The DIW extruder works with an air pump, and the air pressure is controlled by the air pump regulator, as shown in Figure 3.14. This allows for selecting a suitable pressure when operating the 3D printer.

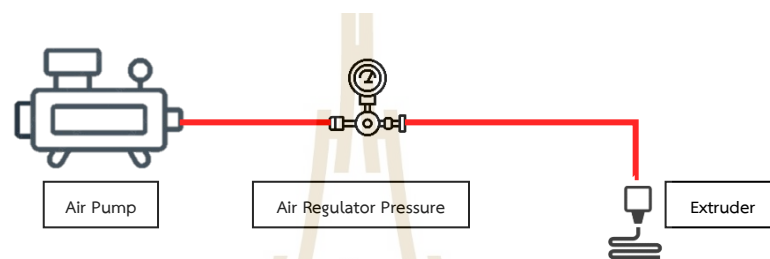


Figure 3.14 The illustration of DIW extruder component.

As mentioned earlier, the new design of the extruder system has been adopted to replace the conventional extruder in FDM 3D printers. For 3D printing aerogel materials, the extruder is modified using direct ink writing techniques, as shown in Figure 3.15. Direct ink writing techniques are generally classified into three types: 1) pneumatic, 2) piston-driven, and 3) screw-driven. In pneumatic dispensing, the driven force is provided by air pressure from the air pump. The piston-driven technique is controlled by a motor, providing vertical mechanical force, while the screw-driven technique utilizes rotational mechanical force. The choice of direct ink writing technique depends on the application. For large quantity materials, the screw pump is suitable. However, for small quantity materials, direct ink writing techniques garner more attention as they allow direct feeding from the syringe, resulting in less wasted material.

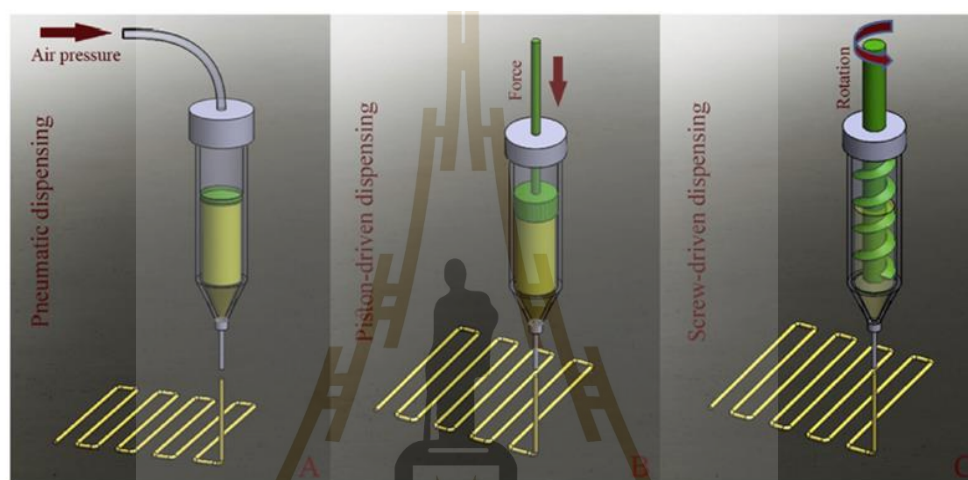


Figure 3.15 Schematic diagram of the direct ink writing for aerogel material methods: (A) pneumatic, (B) Piston-driven, and (C) screw-driven dispensing method (Derakhshanfar *et al.*, 2018).

3.1.6.1 The extruder selection

3.1.6.1.1 Pneumatic: This technique is used for printing with a small amount of material. The material is loaded inside the syringe, ranging from 3 to 250 ml, but the most widely used syringe is 10 ml. In this case, the pneumatic design is specifically constructed for the 10 ml syringe. The printed part of the pneumatic extruder system is designed to fit with the 10 ml syringe and pneumatic fitting. The pneumatic fitting is connected to the air tube, air regulator pressure, and air pump, respectively, as in Figure 3.16.

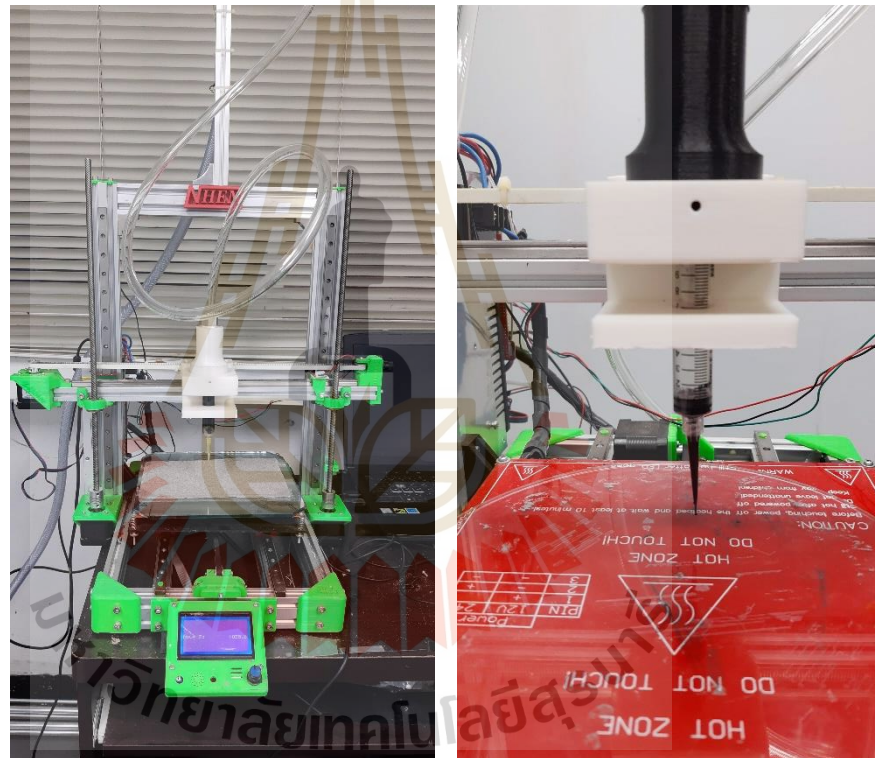


Figure 3.16 Pneumatic dispensing development.

3.1.6.1.2 Piston-driven: The stepper motor controls the piston-driven mechanism, which provides the vertical mechanical force to push the material out of the syringe. The stepper motor provides the direct force from the motor to the syringe in the design. The stepper motor is connected to the 10 mm screw rod shaft and the syringe as in Figure 3.17.

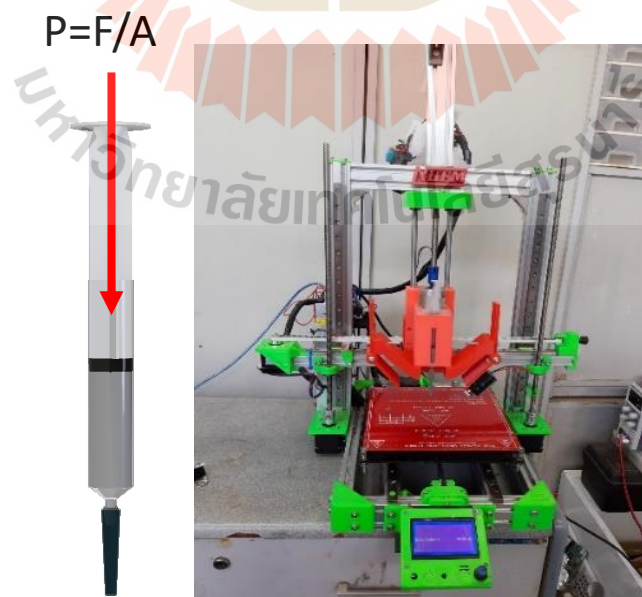
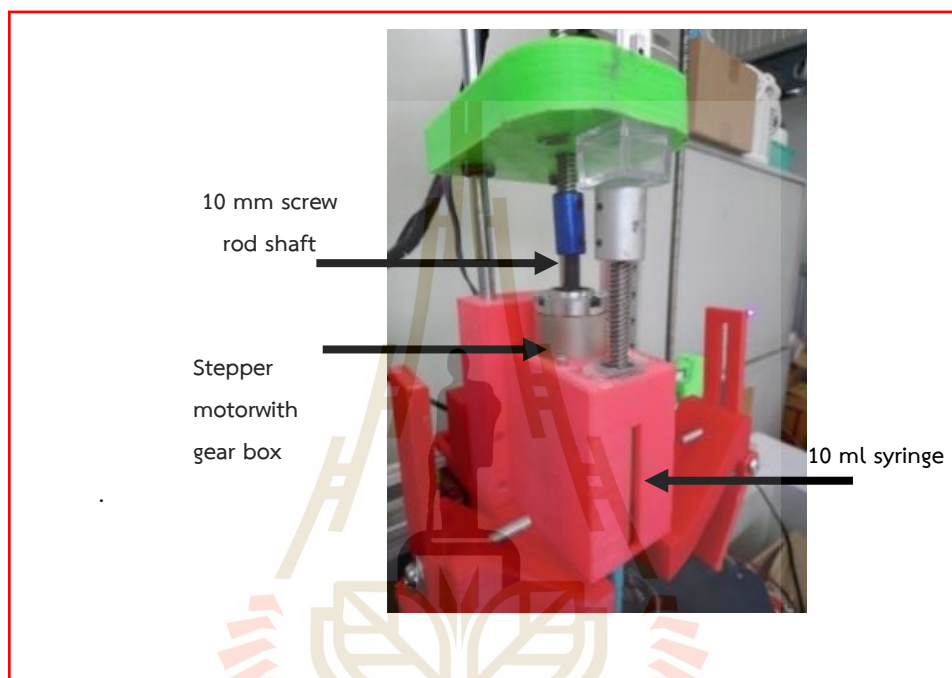


Figure 3.17 The illustration of piston-driven.

3.1.6.1.3 Screw-driven: In this work, the screw is driven by stepper motor, which provides the rotational force required for the screw's movement. It functions by utilizing a rotating screw or auger to feed the material. The screw, often referred to as an extruder screw or feed screw, is responsible for pushing the material forward. In the design, a 100 ml syringe is a material loader that connects to the air pump; the screw is inside the extruder, and also the screw is directly connected to the Nema 17 stepper motor. Regarding the nozzle, the smallest possible size in this work is 1.2 mm. The extruder system is presented in Figure 3.18.

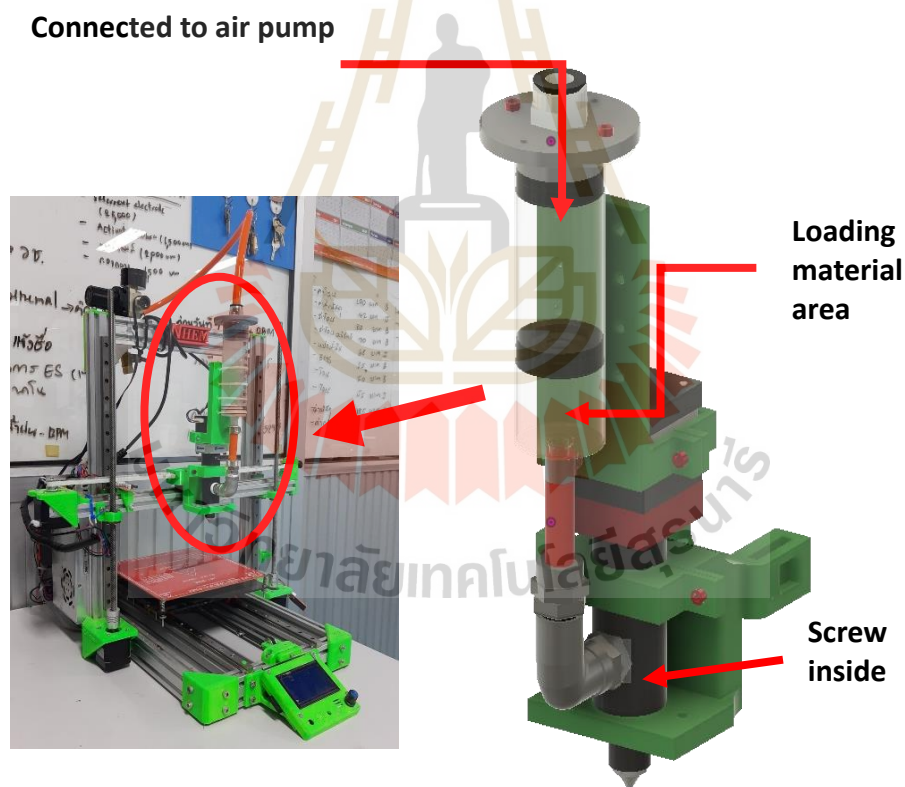


Figure 3.18 Screw-driven dispensing development for aerogel and paste material.

3.2 High viscous ink 3D-printed electrode preparation

Objective 2: To study and prepare the high viscous ink 3D-printed electrodes using carbon and cellulose-based materials.

To achieve objective 2, the electrode material must be prepared as a paste. However, the raw active material is in powder form. This means that a binder material is required to transform the raw active powder material into ink or paste. By mixing them with an optimized ratio, it can be used as ink for 3D printing for 3D electrodes, as

Hypothesis 2 (H2): Carbon-based materials can be mixed with cellulose-based materials and suitable for extruded 3D printing, when rGO/CA 5 % wt in Acetone mixed with optimized condition.

Materials:

- Reduce graphene oxide (rGO) produced by Haydale
- Activated carbon (AC) and carbon black (CB) from SCG company
- Cellulose acetate (CA): 99.99%, average Mn= 50,000 by GPC (Aldrich)
- Methylcellulose (MC): $C_{20}H_{38}O_{11}$, 99.95%, high viscosity 4000 cPs by Thomas Baker, India
- Aniline: $C_6H_5NH_2$, ACS reagent, $\geq 99.5\%$, Mw=93.13 g/mol by Aldrich
- Acetone: CH_3COCH_3 , ACS reagent, $\geq 99.5\%$, Mw=58.08 g/mol by RCI Labscan
- Deionized water (DI, Synchrotron Light Research Institute)
- Hydrochloric acid (HCl)
- Potassium hydroxide (KOH)

3.2.1 Ink design

3.2.1.1 Methyl cellulose (MC)

Colloidal gel materials are excellent candidates for direct ink writing because their viscoelastic properties allow them to maintain their shape, even when spanning gaps in the underlying layers of the printed structure. Two important criteria are considered in the design of this ink. First, the ink must exhibit a well-controlled viscoelastic response, allowing it to flow through the deposition nozzle and immediately set to retain the shape of the deposited features. Second, the ink must contain a high colloid volume fraction to minimize drying-induced shrinkage after complete assembly.

In this work, the ink design is first modeled using various compositions of AC, MC, and water with different aspect ratios. The other conditions of the aerogel are loaded into a syringe and printed using pneumatic dispensing techniques while varying the operating air pressure from 15 to 80 PSI. The printed results show that the optimum composition for the aerogel is achieved with 7.5-10.0 wt% of MC. When the MC content is below 7.5 wt%, the printed objects exhibit shrinkage and lack shape retention due to low viscosity. On the other hand, when the MC content is above 10 wt%, the high viscosity of the ink makes it difficult to print and can lead to nozzle clogging problems. The printed results are reported in Table 3.1 and Figure 3.19. However, the ink with 7.5 wt% of MC, exhibiting a well-controlled viscoelastic response for shape retention of the deposited features, shows low evaporation solidity.

To overcome the solidity issue of the 3D-printed objects, the binder is changed from MC to CA. Using acetone as a solvent, the ink evaporates less, resulting in improved solidity, as shown in Figure 3.19C. The demonstration of the ink design reveals that using CA as a binder at 7.5-10.0 wt% is suitable for 3D-printed objects in this work.

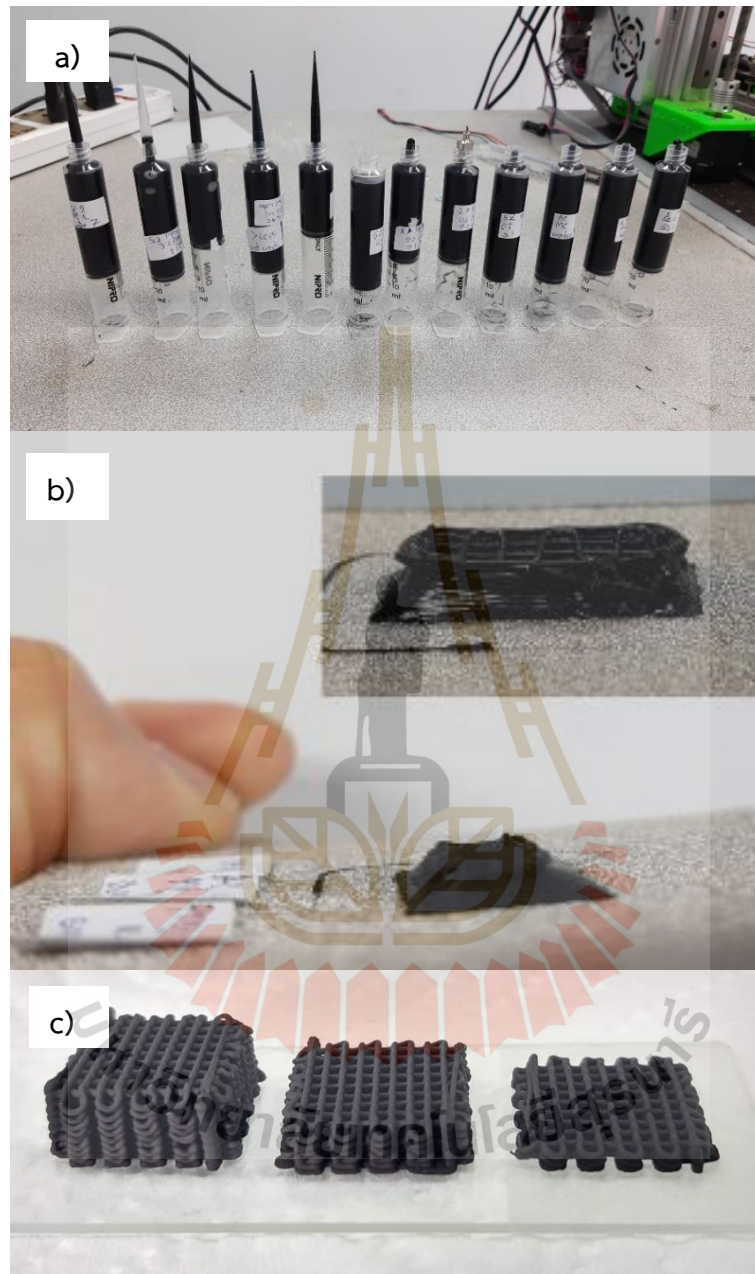


Figure 3.19 a) The 3D-printed object with a variable condition of the ink samples. b) The 3D-printed object with a MC < 7.5 wt%. c) The printed object with CA 7.5-10.0 wt%.

Table 3.1 The aspect ratio of 3D-printed ink composite material.

AC	MC	Water	AC:MC: Water	MC (wt%)	Printing condition		Printing result
					Pressure (PSI)	Print speed (mms ⁻¹)	
0.5	0.5	9.0	1:1:18	5	15-20	4	- Too liquid and low viscosity; the printing sample cannot sustain itself
1.0	0.5	8.5	2:1:17	5	15-20	4	- Too liquid and of low viscosity; the printing sample cannot sustain itself
1.5	0.5	8	3:1:16	5	15-30	4	- Too liquid and of low viscosity; the printing sample cannot sustain itself
2.0	0.5	7.5	4:1:15	5	20-30	4	- Cannot sustain itself
1.25	0.75	8.0	5:3:32	7.5	-	-	- Good shape in printing, but the viscosity is a bit low
1.75	0.75	7.5	7:3:30	7.5	60-65	4	- Good shape in printing, but the viscosity is a bit too high
0.5	1.0	8.5	1:2:17	10	20-30	4	- The viscosity is a bit low, and it cannot sustain itself for 30 minutes

Table 3.1 The aspect ratio of 3D-printed ink composite material (Continued).

AC	MC	Water	AC:MC:Water	MC (wt%)	Printing condition		Printing result
					Pressure (PSI)	Print speed (mms ⁻¹)	
1.0	1.0	8.0	1:1:8	10	50-60	4	- The viscosity is a bit too low and cannot sustain itself
1.5	1.0	7.5	3:2:15	10	75-85	4	- Good shape in printing, but the viscosity is a bit too high and it cannot sustain itself for 1 hour
2.0	1.0	7.0	2:1:7	10	80-90	4	- Viscosity is too high; cannot finish printing
0.5	1.5	8.0	1:3:16	15	75-80	4	- Viscosity is too high; cannot finish printing

Problem

In the earlier experiments, MC was used as a binder. MC can be dissolved in water, which means that when the printed electrode is soaked in an aqueous electrolyte, the MC can be degraded. Another problem is its stability in environmental conditions, as it degrades more quickly on high-humidity days, as in Figure 3.20.

Solution

Consider using a new binder that is not soluble in water. CA is chosen because it is not soluble in water but is soluble in acetone. However, acetone evaporates rapidly. To use acetone as a solvent for CA, a small amount of paraffin oil, approximately 1 wt%, needs to be added.

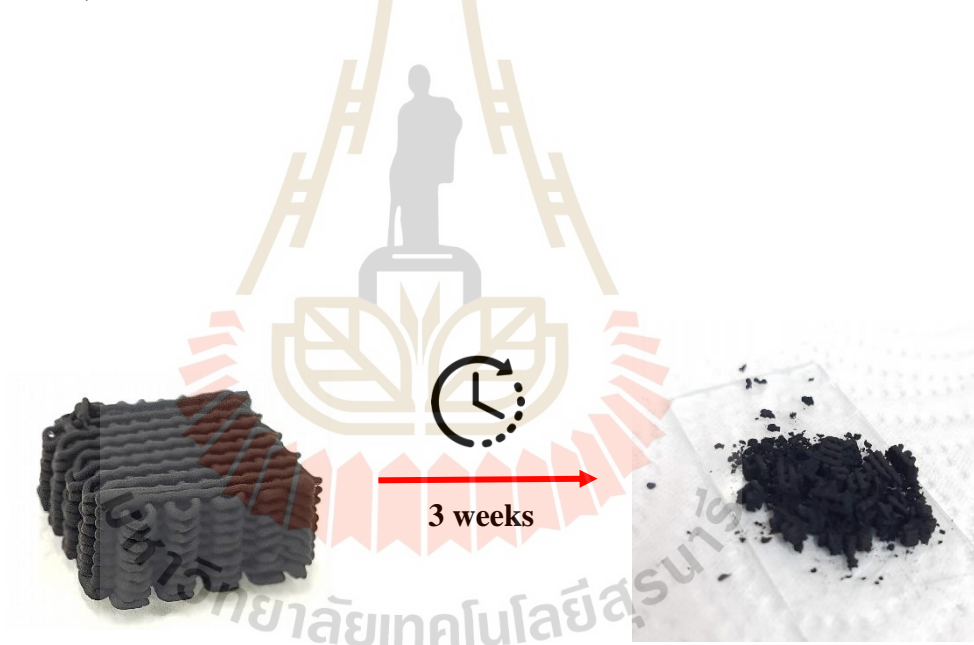


Figure 3.20 The degradation of 3D-printed rGO occurs when CA is used as the binder.

Note: It is important to consider low humidity when using and storing 3D-printed objects where MC is the main compound.

3.2.1.2 Cellulose acetate

In this process, CA is considered an alternative after encountering issues with MC. CA is chosen to address the degradation problem caused by using CA as a binder, due to its insolubility in water. The following section presents the materials, methods, procedures, experimental conditions, and results.

The material ratio used in the previous section (3.2.1.1 Methyl cellulose (MC)) can guide subsequent experiments. In the ink preparation stage, a rGO, CA, and acetone mixture. The powder material ratio of rGO to cellulose acetate is 1:19, corresponding to a 5 wt% concentration of rGO. The ink preparation for a 10 ml syringe requires 0.2g of rGO, 3.8g of cellulose acetate, and 16g (20 ml, with a density of 0.791 g/mL at 25°C) of acetone as the solvent. The mixture is achieved through manual homogenization or hand mixing. After mixing, the material is loaded into a 10 ml syringe and connected to a syringe holder, as shown in Figure 3.16.

Celluloses acetate printing test

In the first printing test, the bridge printing is performed at a printing speed of 5 mm/s by varying the distances 2, 4, 6, 8, and 10 mm, as shown in Figure 3.21. This testing shows the fast evaporation of ink, addressing the overhang and print collapse problem. To test the printing electrode, a model with dimensions of 30×15×5 mm³ was constructed, as shown in Figure 3.22.

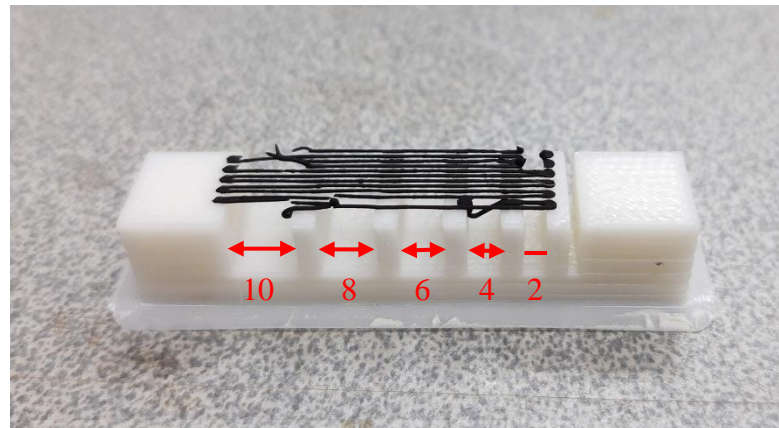


Figure 3.21 The bridge material print testing of CA.

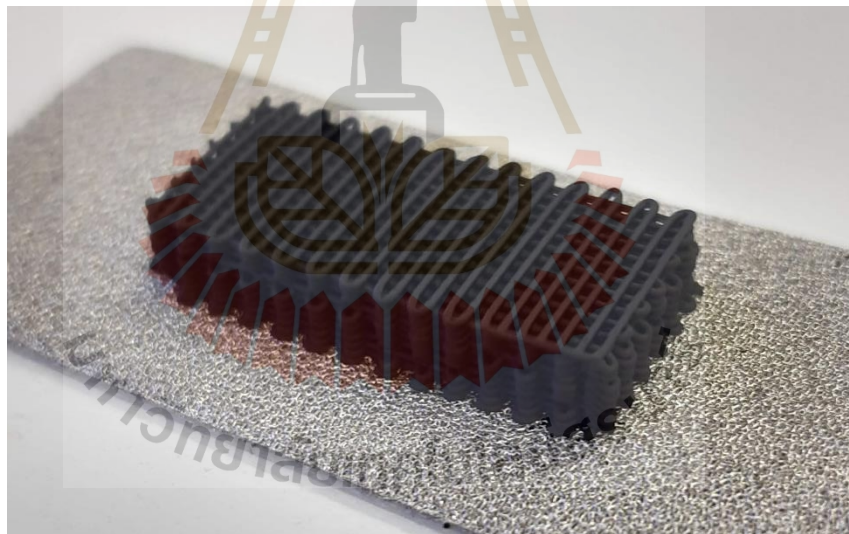


Figure 3.22 The test printing electrode by the pneumatic extruder. The material is 5 wt% of rGO, and CA is used as a binder. The printing speed is 5 mm/s at an air pressure of 413 KPa (60 PSI).

3.3 3D-printed supercapacitor electrode

Objective 3: To study printing parameters of the 3D-printed supercapacitor electrodes.

As the optimized ink ratio from the previous section has been determined, these parameters have been selected for printing the 3D supercapacitor in this section. Specifically, the following parameters are utilized for printing the 3D-printed electrode: fixed pattern, flow speed, and printing speed. The only varying parameter is the number of layers, ranging from 4 to 24. The electrode design is illustrated in Figure

HYPOTHESIS 3 (H3): 3D printing parameters (layer number, pattern, flow speed, printing speed) affect to the 3D-printed electrode shape and their capacitance values.

3.23.

A net-shaped electrode with dimensions of $10 \times 10 \text{ mm}^2$ is selected for the electrode design. This size is chosen because it allows for the simultaneous printing of multiple samples, and the net-shaped design provides a larger surface area than a solid shape. The layer thickness of the net-shaped electrode is set at 0.15 mm. The process diagram in this section is presented in Figure 3.24.

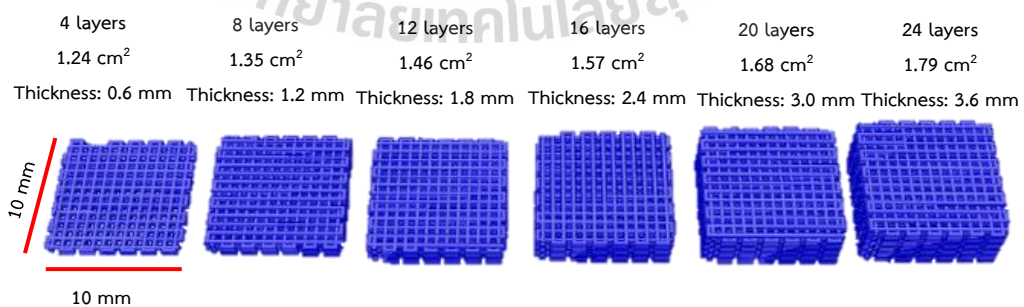


Figure 3.23 The electrode design, the net shapes $10 \times 10 \text{ mm}^2$, and thickness is varied from 0.6 mm (4 layers) to 3.6 mm (24 layers).

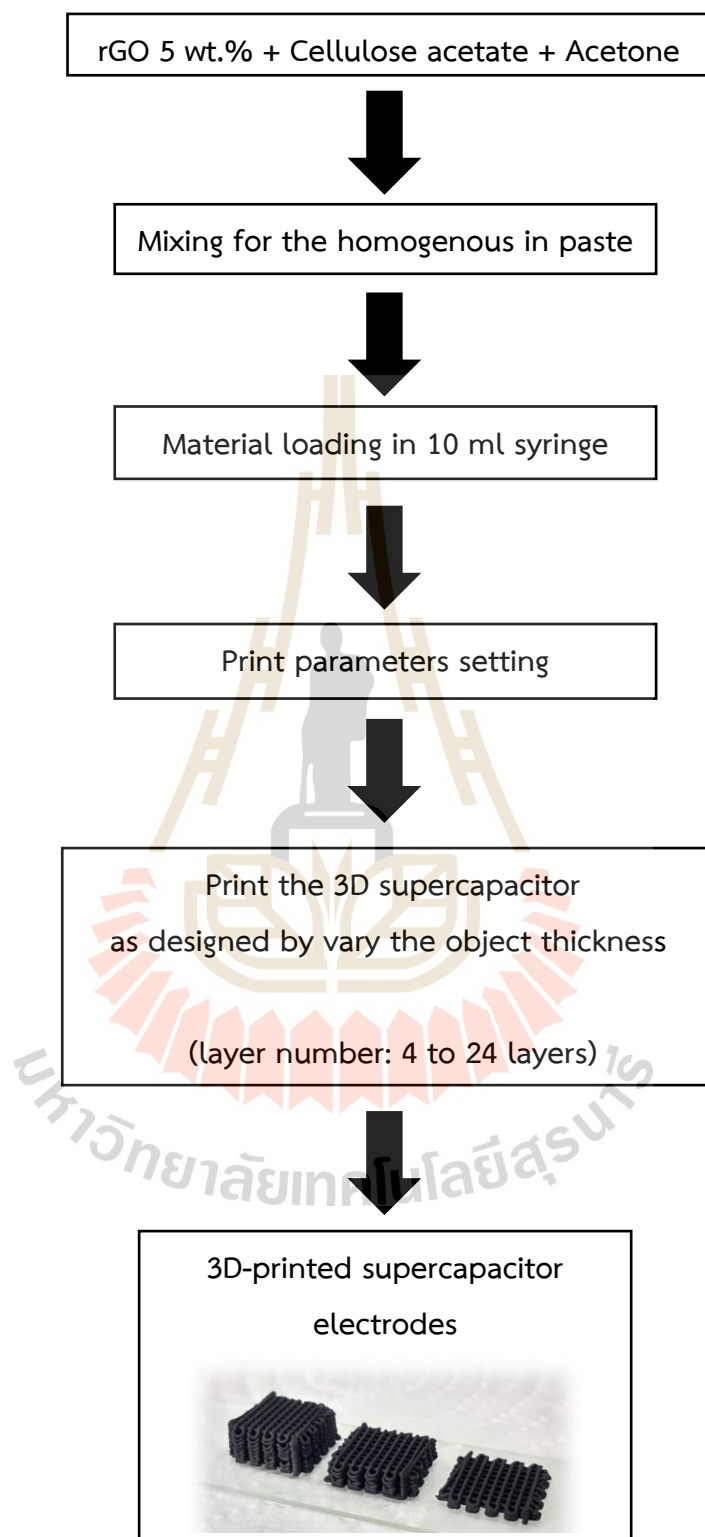


Figure 3.24 The diagram showing the preparation of a 3D-printed supercapacitor electrode.

3.3.1 The ink preparation and printing

1. **rGO 5 wt.% + Cellulose acetate + Acetone:** The powder material ratio of rGO to CA is 1:19, corresponding to a 5 wt% concentration of rGO. Based on this ratio, the ink preparation for a 10 ml syringe requires 0.2g of rGO, 3.8g of CA, and 16g (20 ml, with a density of 0.791 g/mL at 25°C) of acetone.
2. **Mixing for a homogeneous paste:** rGO and CA, both in powder form, can be manually mixed in a beaker. During mixing, acetone is gradually added to the beaker until the materials form a paste-like and homogeneous mixture.
3. **Material loading in 10 ml syringe:** The paste of the mixed material is loaded into a 10 ml syringe and sealed with a rubber plunger. A 0.4 mm diameter nozzle is inserted into the syringe tip, and then the syringe is connected to the pneumatic extruder system.
4. **Print parameters setting:** The parameters such as layer number, pattern, flow speed (pressure), and printing speed are configured in the slicing program (Slic3r and Repetier-Host), as outlined in Table 3.2.
5. **Print the 3D supercapacitor as designed by varying the object thickness:** The design of the 3D supercapacitor electrode is based on the assumption that the electrode's thickness affects its performance. The electrode shape remains consistent at 10×10 mm², but the thickness varies. Specifically, the thickness is set at 0.6 mm for 4 layers, 1.2 mm for 8 layers, 1.8 mm for 12 layers, 2.4 mm for 16 layers, 3.0 mm for 20 layers, and 3.6 mm for 24 layers.
6. **3D-printed supercapacitor electrodes:** Five sets of electrodes with varying thicknesses are printed and will be utilized in the subsequent step of the experiment, which involves PANI coating.

Table 3.2 The printing parameter of 3D-printed supercapacitor.

Printing parameters	Values	Description
Layer number	Depend on model	● 4, 8, 12, 16, 20, and 24 layers
Layer high	0.15 mm	● Based on nozzle diameter (less than nozzle diameter 0.4mm)
Printing speed	2 to 40 mm/s	● Correlated with air flow pressure
Flow air pressure	137 KPa (20 PSI) to 413 KPa (60 PSI).	● Correlated with material viscosity and printing speed
Printing pattern	Net shape (rectilinear pattern)	● Simple and higher surface area compared to a solid object shape
Bed temperature	None	● No need function in this case
Print perimeters line	1 (line)	● Material purged around the electrode before printing

3.4 Polyaniline (PANI) synthesis and coating

PANI is a conductive polymer that has been important in energy storage systems as a pseudocapacitive material. PANI has received much attention from researchers due to its high specific capacitance, high flexibility, and low cost.

HYPOTHESIS 4 (H4): PANI coating process (coating method and cycle numbers) affects to capacitance values of the 3D electrodes. When PANI coating method and cycle number offers high surface area.

To address hypothesis 4, PANI is synthesized through chemical polymerization due to its simplicity, ease of preparation, scalability, and low cost. The drop coating method in the PANI synthesis bath is selected for coating the surface of the 3D-printed supercapacitor made from rGO. This method applies the PANI synthesized in the bath as a film onto the electrode surface. To increase the thickness of the PANI film, the number of coating cycles varies from 1 to 5 by repeating the drop coating process. These processes are correlated with objective 4.

Objective 4: To synthesis and coating PANI on 3D-printed supercapacitor electrode.

3.4.1 Polyaniline synthesis

PANI was synthesized by chemical oxidative polymerization (COP) of aniline monomer using ammonium persulfate as a redox initiator. First, 0.5 ml of aniline monomer was mixed in 1M HCl solvent. Then, 1.55g of ammonium persulfate in 1M HCl solvent was prepared as the redox initiator. Both solutions were rapidly mixed in the same proportion at room temperature, as shown in Figure 3.25. Subsequently, the solution changed its color to green as the chemical oxidative polymerization of the emeraldine salt formed. The polyamine solution was diluted from solid acid to pH 7 by precipitation and filtered with DI water several times. The PANI colloids were then ready for coating the 3D-printed electrode.

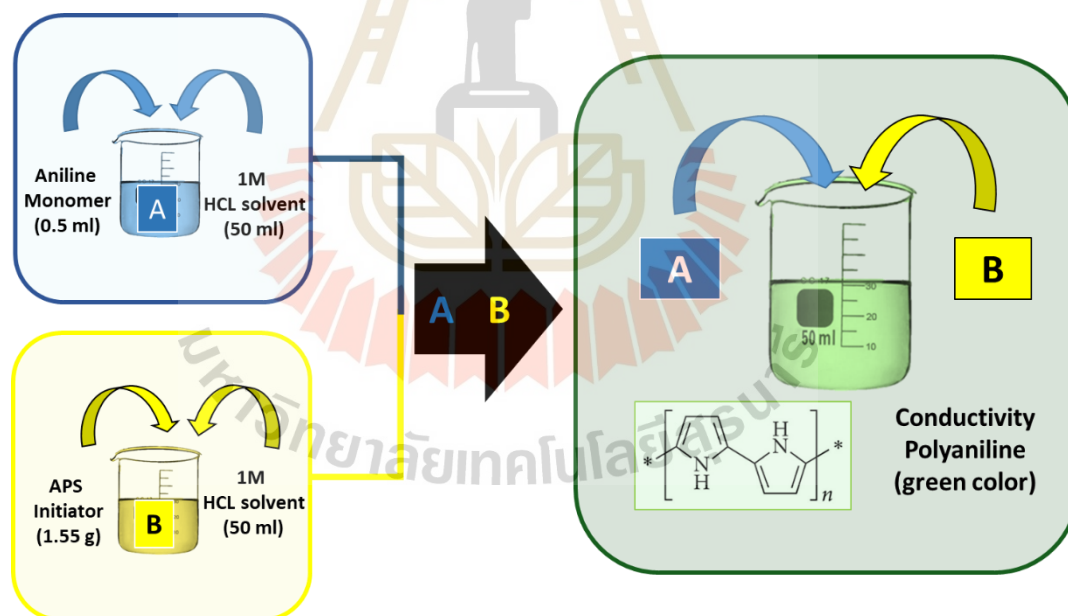


Figure 3.25 The experimental procedure for preparation of conductive PANI by the in situ chemical oxidative polymerization approach.

3.4.2 Polyaniline coating

Hypothesis 4 states that the thickness of the PANI film on the 3D-printed electrode can vary with the number of coating cycles. An increase in PANI film thickness is expected to increase the surface area of the 3D-printed electrode, which will affect its capacitance.

In the first experiment, a 3D-printed electrode was coated with a PANI film using a simple drop coating method. However, a problem arose when removing the sample from the coating bath due to its small size. To address this issue, a new approach was employed wherein the 3D-printed electrode was coated with PANI using the inside of a 3 ml syringe. The 3D-printed electrode was soaked in PANI colloid for 10 minutes during each coating cycle. Then, the PANI colloid was purged from the syringe, and the syringe with the electrode was placed in an oven at 60°C for 1 hour. This process completed one PANI coating cycle, as presented in Figure 3.26. The process was repeated for additional PANI coating cycles. In this study, the number of PANI coating cycles varied from 1 to 5.

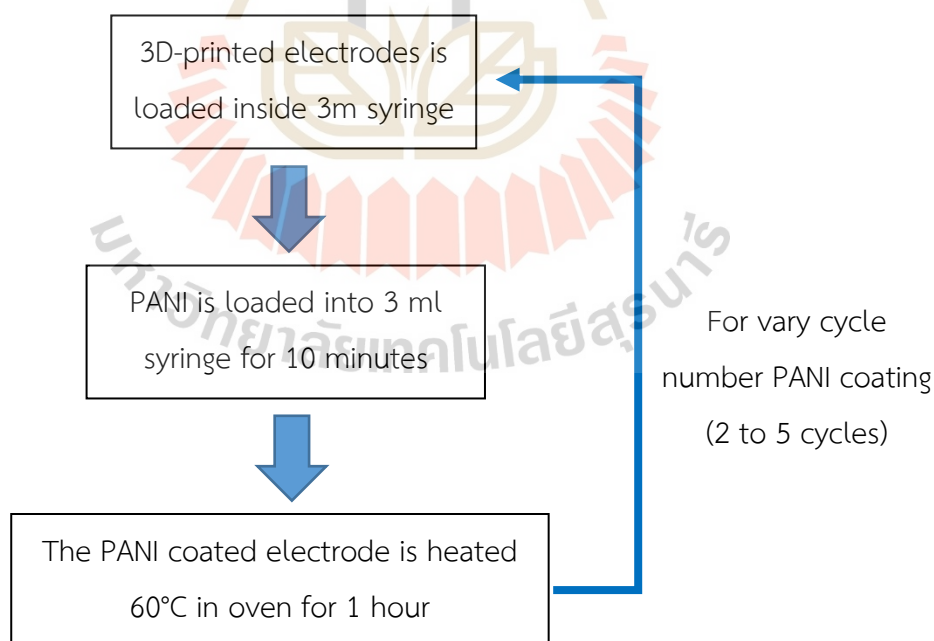


Figure 3.26 Diagram showing the PANI coating process.

3.5 Material characterization

3.5.1 X-ray diffraction (XRD)

X-ray diffraction (XRD) is an analytical technique for determining the structure of material. It provides the arrangement of atoms or molecules within a crystal lattice, including the spacing between lattice planes, the crystal symmetry, and the types of atoms present.

The principle behind XRD is based on the interaction of X-rays with the regular arrangement of atoms in a crystalline material. When a beam of X-rays strikes a crystal, it undergoes constructive interference with the crystal lattice, resulting in a diffraction pattern as illustrated in Figure 3.27. The fundamental principle behind XRD is Bragg's law, which relates the angles of incidence and diffraction of X-rays to the interatomic spacing within a crystal lattice. According to Bragg's law: $n\lambda = 2d \sin \theta$, where n is an integer representing the order of the diffraction peak, λ is the wavelength of the incident X-ray radiation, d is the inter planar spacing within the crystal lattice, and θ is the angle between the incident X-ray beam and the crystal lattice plane.

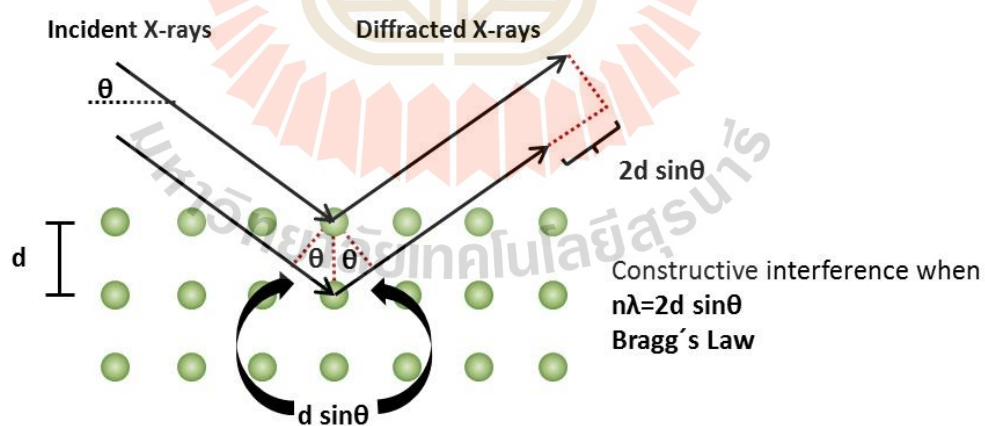


Figure 3.27 The diagram represents Bragg diffraction by crystal planes (Adapted from Leng *et al.*, 2009).

In this work, the phase and structure analysis of the PANI was carried out by X-ray diffraction (XRD; D2 Advance Bruker) with $Cu - K\alpha$ at $\lambda = 0.15406$ nm. The scan range was defined from 10° to 60° , with a time step of 0.5 and a step size of 0.02.

3.5.2 Scanning electron microscopy (SEM)

Scanning electron microscopy (SEM) is a powerful imaging technique used to obtain high-resolution images and surface topography information of samples. It provides detailed structural and morphological information at the micro- and nanoscale. This study employed an Oxford Instruments SEM to produce high-resolution images of a PANI-coated film on a 3D-printed electrode. Using carbon tape, the sample was affixed to the top of a conductive sample holder. The sample was conductive in this case, eliminating the need to coat it with a layer of gold film to enhance image quality. The sample was then loaded into a low vacuum load-lock chamber. A high voltage ranging from 1 kV to 30 kV was applied to operate the SEM.

3.6 Electrochemical properties measurement

Objective 5: To study electrochemical properties of the 3D-printed supercapacitor electrodes

3.6.1 Electrode preparation

The rGO/PANI square-shaped electrodes, measuring 10×10 mm, were prepared by DIW 3D printing as standalone electrodes in the previous section. The electrodes were kept soaked in an electrolyte for at least one day, and then the 3D-printed electrodes were ready to be installed in an electrochemical cell.

Hypothesis 5 (H5): Electrochemical measurement preparation (soaking time in electrolyte) affects to capacitance values of the 3D electrodes.

3.6.2 Electrolyte preparation

The electrolyte was prepared in an aqueous solution. The 3M KOH electrolyte was prepared at room temperature, and the concentration can be calculated using the following equation:

$$\text{Molar concentration} = \frac{\text{Amount in mole}}{\text{Volume of solution}}$$

3.6.3 Electrode setup

The electrochemical measurements were conducted in a 3-electrode system composed of a platinum counter electrode, an Ag/AgCl reference electrode, and a working electrode, as illustrated in Figure 3.28. The electrochemical cells were connected to the Metrohm Autolab PGSTAT302N potentiostat/galvanostat system, and Nova software was used for operation, as shown in Figure 3.29.

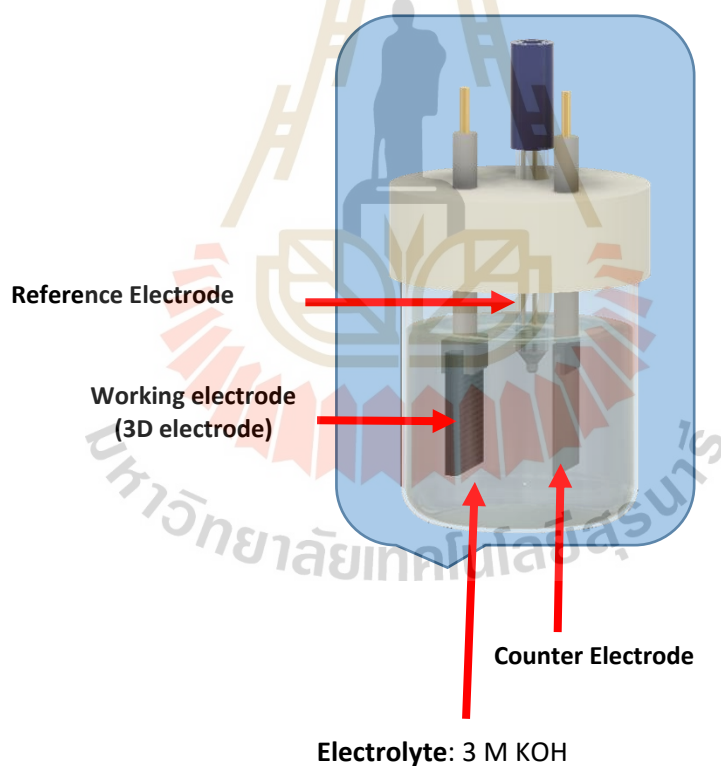


Figure 3.28 3-electrode electrochemical cell setup.

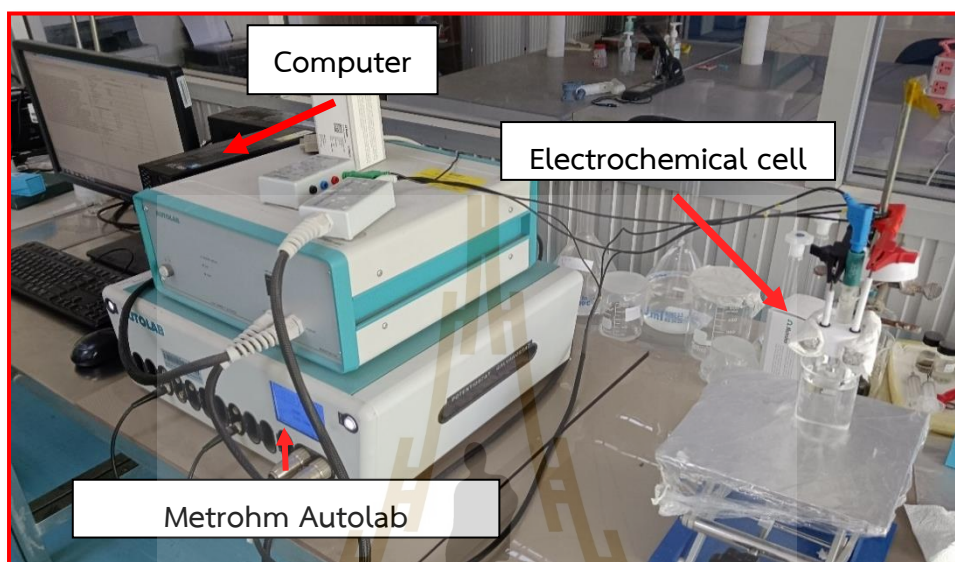


Figure 3.29 An electrochemical measurement was set up with a 3-electrode computer control system and a Metrohm Autolab PGSTAT302N potentiostat/galvanostat.

3.6.4 Cyclic voltammetry

This study measured CV under the conditions of potential windows from -0.9V to 0.4V and scan rates of 5, 10, 20, 30, 50, 100, 150, and 200 mV/s. The expected PANI CV curve shows the redox reaction peak, representing the pseudocapacitive nature of the material. For the evaluation of CV, the specific capacitance can be calculated using the following equation:

Specific capacitance or gravimetric capacitance:

$$C_{cv} = \frac{1}{vm\Delta V} \int IdV$$

areal capacitance: the amount of electric charge that can be stored per unit area of one of its electrodes.

$$C_A = \frac{1}{vA\Delta V} \int IdV$$

Where $\int IdV$ the area of the CV curve, m is the mass of active material (g), A is the area of the electrode (cm^2), v is the scanning rate (mV/s) and ΔV is the voltage window (V).

3.6.5 Galvanostatic charge/discharge

In this study, the GCD was measured with the same potential window as the CV, and the measurement current densities were 0.5, 1.0, 2.0, 3.0, 4.0, and 5.0 A/cm^2 . The GCD charging and discharging are performed by applying current and voltage, resulting in the charging-discharging time. This can be used to evaluate the capacitance with the area (C_A) of the electrode using the following equation:

$$C_A = \frac{I\Delta t}{A\Delta V}$$

Where I the discharge current (A), A is the area of the electrode (cm^2), Δt is the discharging time (s). and ΔV is the voltage window (V).

3.6.6 Electrochemical impedance spectroscopy

In this work, the EIS measurements were performed by the frequency range 0.01 Hz to 100 kHz at 0.1 V in galvanostatic mode. The equivalent circuits of electrochemical cells were evaluated with Nova 1.11 software.

CHAPTER IV

RESULTS AND DISCUSSION

In Chapter IV, the results and discussion of the thesis experiment are presented and divided into five major sections:

- 4.1 Developing a 3D printer for the fabrication of supercapacitor electrodes: This section provides the results and discussion of developing the direct ink writing (DIW) technique.
- 4.2 Studying and preparing high-viscosity ink for 3D-printed electrodes using carbon and cellulose-based materials: The optimized ratio of ink materials and the results of print testing are presented.
- 4.3 Investigating the printing parameters of 3D-printed supercapacitor electrodes: This section presents and discusses the printing results and parameters.
- 4.4 Synthesizing and coating PANI on 3D-printed supercapacitor electrodes: The synthesis method and coating process results are presented. Additionally, the morphology and structure of PANI were investigated using SEM and XRD.
- 4.5 Studying the electrochemical properties of 3D-printed supercapacitor electrodes: Cyclic voltammetry (CV), galvanostatic charge/discharge (GCD), and electrochemical impedance spectroscopy (EIS) were evaluated to explain the capacitive behavior.

4.1 Developing a 3D printer for the fabrication of supercapacitor electrodes

4.1.1 3D printer

The purpose of developing 3D printing is to address the research gap in supercapacitors, explicitly focusing on the effect of electrode structure on capacitance. Among various printing techniques, Direct Ink Writing has been selected.

for 3D printing electrodes due to several advantageous benefits. These include its compatibility with a wide range of materials, its ability to handle both small and large amounts of material, and its ease of preparation. The details of the development can be found in Table 4.1.

Table 4.1 The specification of the developed DIW 3D printer supercapacitor used in this work.

Mechanical Specifics	Description
Machine size	350 mm × 400 mm × 500 mm (LWH)
Maximum printing area	220 mm × 220 mm × 350 mm
Nozzle diameter	0.4 mm (optional 0.8 mm, 1.2 mm, and 1.5 mm)
Motor driver	TMC 2209: 256 micro steps
XY position precision	100 μ m
Z position precision	100 μ m
Max pressure	551 kPa (80 PSI)
Print bed temperature	25°C (room temperature) to 90°C
Minimum material requirement	3 ml

4.1.2 The extruder development system

The extruder system considered in this research consists of three types. The development initially started with the screw-driven dispensing system, followed by the piston-driven dispensing system, and finally, the pneumatic dispensing system. Through testing, the advantages and limitations of each system were identified, making them suitable for different applications. The development sequence is as follows:

Initially, the screw-driven dispensing system was adopted due to the availability of existing equipment, albeit initially used for different purposes. Modifications were made to the material loader, replacing it with a 250 ml syringe. This adaptation made the system suitable for tasks involving large volumes of material but not optimal for prototyping research requiring small material volumes. Another constraint is the nozzle size, which measures approximately 1.5 mm. This dimension is too large for 3D

electrode printing, which necessitates a nozzle size equal to or smaller than 0.4 mm. However, the system combines air pressure and a screw mechanism, facilitating the effective dispensing of high-viscosity materials and precise control over the dispensing rate.

Due to the limitations of the pneumatic dispensing extruder system, which requires large material quantities, a new system was needed as a replacement. The chosen alternative is the piston-driven system, which employs motor force to drive the plunger and dispense the material through the nozzle. While this system is well-suited for small quantities of material, it encounters a significant challenge in 3D electrode printing. The high viscosity of the material exceeds the motor's force, leading to difficulties in material dispensing and inconsistent injection rates due to accumulated pressure issues.

To overcome the challenges associated with injecting materials in low quantities and high viscosity, which are often encountered in screw-driven and piston-driven systems, the pneumatic dispensing system was developed. This system is generally less complex than the preceding two systems. However, it has the limitation of requiring continuous material injection to maintain pressure within the system, even during temporary pauses in the injection process.

Despite this limitation, the pneumatic dispensing system offers several advantages. It can be used with various quantities and accommodate materials with varying viscosity levels. Additionally, it provides convenience in the preparation and printing process. Table 4.2 presents the information regarding the three types of extruder systems obtained from the experiment, while the printing results are displayed in Figures 4.1 to 4.3.

Table 4.2 The direct ink writing techniques comparison.

	Screw-driven dispensing	Pneumatic dispensing	Piston driven dispensing
Amount of material	>30 ml	2-10 ml	2-10 ml
Nozzle diameter	1.4 mm	0.4 mm	0.4 mm
Flow rate controller	motor	Air pressure	motor
Material flow responsiveness	Immediately	Delay 3 seconds	Delay 5 seconds
Material loading time	15 minutes	10 seconds	10 seconds
Pros	<ul style="list-style-type: none"> • The material can be injected continuously and with good control. • Suitable for large volume and high viscosity material 	<ul style="list-style-type: none"> • Suitable for small quantities of materials • Less waste material • High viscosity materials can be injected 	<ul style="list-style-type: none"> • Suitable for small volume and low viscosity materials
Cons	<ul style="list-style-type: none"> • Not suitable for small volume materials 	<ul style="list-style-type: none"> • Not suitable for large volume printing • Not suitable for a low viscosity materials 	<ul style="list-style-type: none"> • Low driven force. • Not suitable for a high viscosity materials

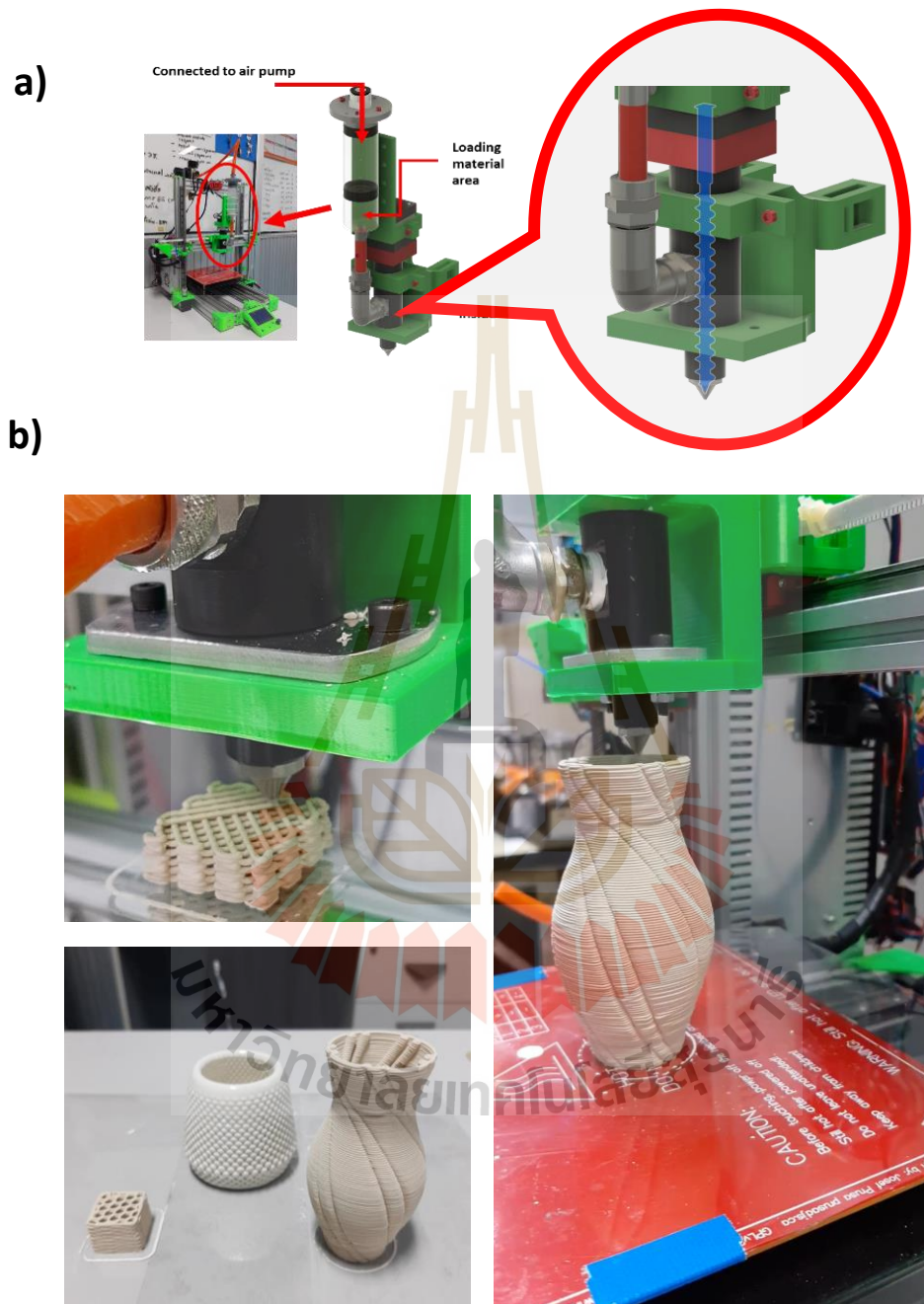
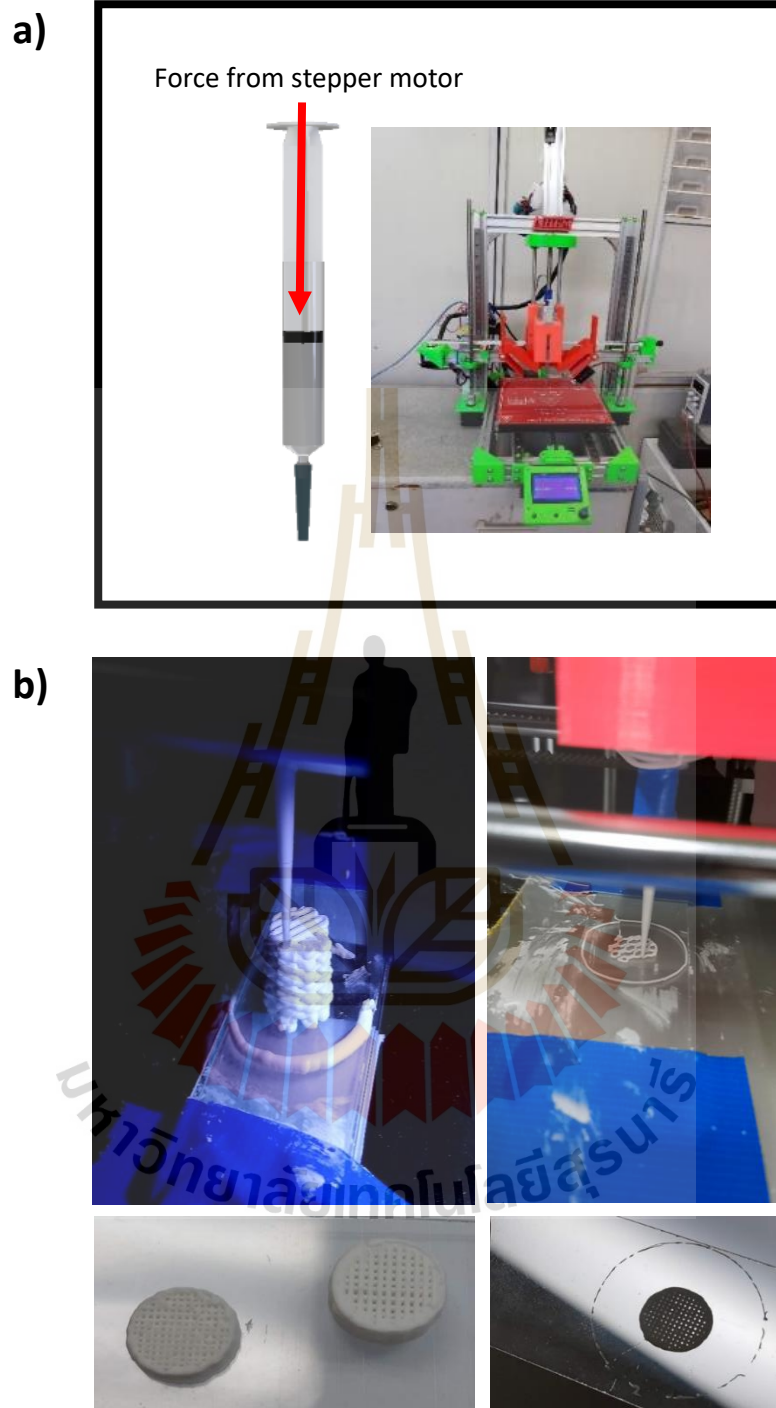


Figure 4.1 a) Screw driving dispensing b) the 3D-printed objects using clay as the material.



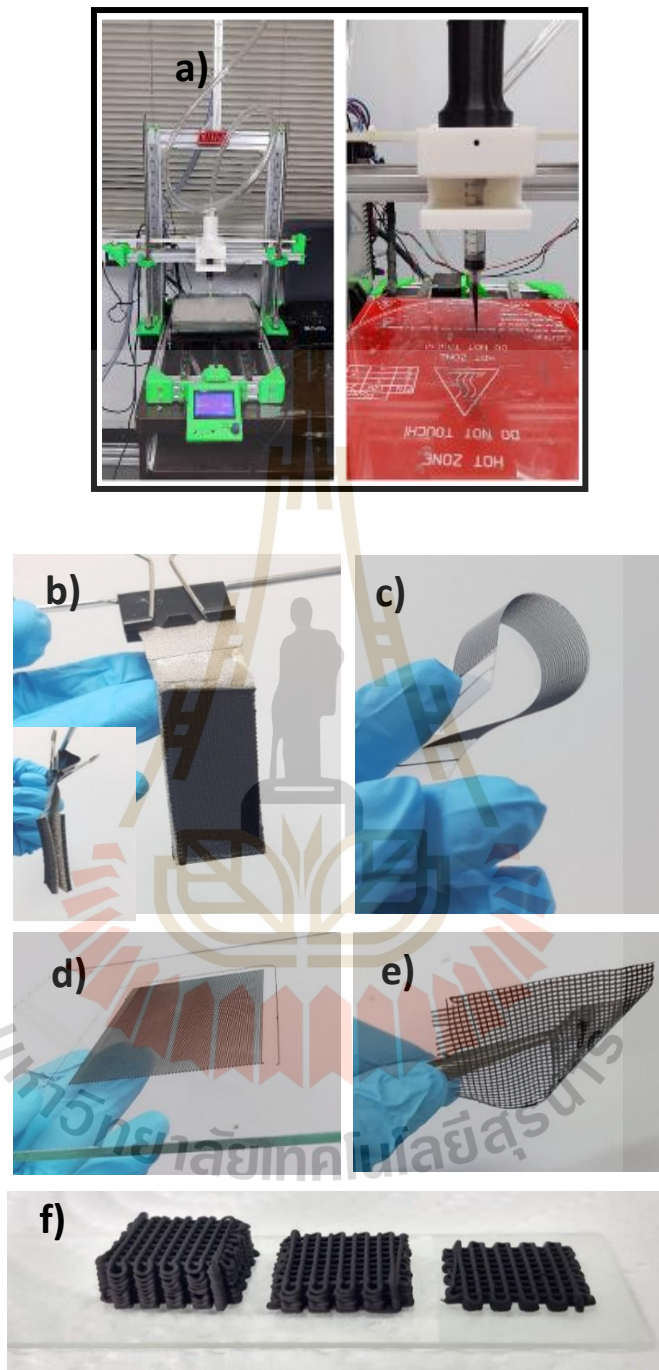


Figure 4.3 a) Pneumatic dispensing extruder. The 3D printing object, whose material is rGO/cellulose acetate, was printed on different substrates: b) nickel foam, c) plastic sheet, d) glass, e) stand-alone, and f) glass slide.

4.1.3 Discussion

This research focuses on printing materials that differ from those typically used in 3D printing, necessitating the design of a new, suitable material extruder system. Three different extruder systems have previously been proposed, each with its advantages and disadvantages. In this study, the pneumatic dispensing system is deemed the most appropriate due to the limited availability of material (< 50 ml) and high viscosity. However, if the material quantity increases, the pneumatic dispensing system can still meet this requirement by designing the material loading component to accommodate larger volumes. Alternatively, the screw-driven dispensing system can be considered, as it offers greater precision in controlling material extrusion compared to pneumatic dispensing.

4.1.4 Summary

This work utilizes the direct ink writing (DIW) system to develop a 3D printer specifically for printing 3D supercapacitor electrodes. The DIW system's significant specifications are outlined in Table 4.1. Regarding the extruder system development for this thesis, the materials prepared will be high-viscosity ink. This involves using a cellulose-based material as a binder to combine different materials into a highly viscous ink. The selection of the extruder system depends on its suitability for the work, and in this research, pneumatic dispensing is considered the most appropriate choice.

4.2 Studying and preparing high-viscosity ink for 3D-printed electrodes

In the preparation of ink for 3D printing, research has shown that cellulose materials have adhesive properties that help the components adhere well together. In this study, two types of cellulose, namely 1) methylcellulose (MC) and 2) cellulose acetate (CA), were considered. In the initial preparation, the MC was mixed with carbon-based materials (i.e., activated carbon and carbon black) and water as a solvent. As mentioned in the previous chapter, various mixtures were experimented with to find the most suitable composition. From these experiments, the optimal ratio for MC as a binder was 7.5-10 wt% of the total weight of components and twice the weight of the carbon-based material. However, despite these findings, issues were still encountered

during printing. The printed electrodes could only maintain their shape for approximately 30 minutes, and another problem arose due to the solubility of MC in water, leading to the dissolution of the electrode when immersed in an aqueous electrolyte.

Although these experiments encountered difficulties, the results provided valuable insights for problem-solving. Based on the preliminary conditions discovered from these experiments, the binder was changed from MC to CA, which has different solubility characteristics. CA can be dissolved in acetone but not in water, making it suitable for use in an aqueous electrolyte.

After establishing the initial conditions for the supercapacitor electrode printing process, the material rGO (reduced graphene oxide) was utilized instead of activated carbon and carbon black. The mixture ratios of the different components remained similar to the original formula. The following mixture ratio was used: the powder material ratio of rGO to CA is 1:19, corresponding to a 5 wt% concentration of rGO. For ink preparation, a 10 ml syringe was used; 0.2g of rGO, 3.8g of cellulose acetate, and 16g (20 ml, with a density of 0.791 g/mL at 25°C) of acetone were required as the solvent. To test the ink's suitability for 3D printing of supercapacitor electrodes, an additional testing process, overhang testing, was introduced in this research, referred to as "bridge material print testing." This testing method is a simple way to determine if the ink can successfully print on empty spaces. The results of printing supercapacitor electrodes using the ink formulation under these conditions are shown in Figure 4.4.

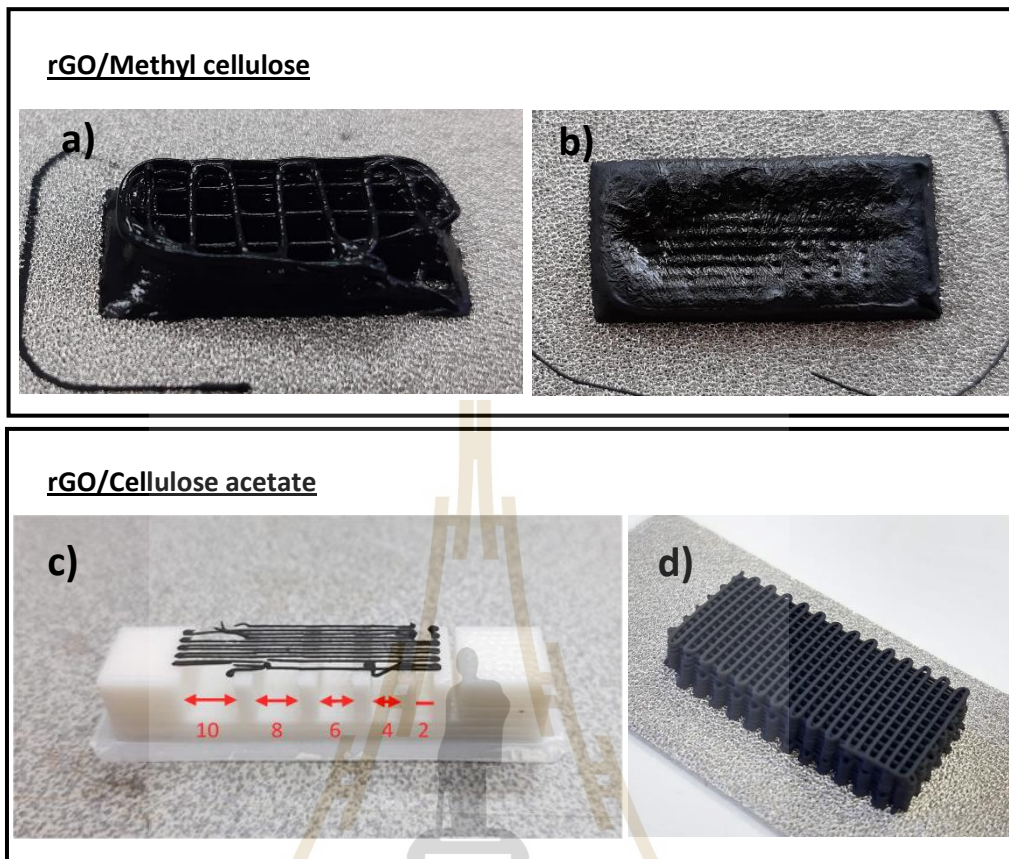


Figure 4.4 The printing result of ink preparation a) The 3D-printed object with MC < 7.5 wt% with infill pattern of printing parameters 5% and b) 50%. c) the CA bridge material print testing by varying the gap from 2 mm to 10 mm, and d) the CA supercapacitor electrode 3D-printed.

4.2.1 Discussion

When comparing the 3D-printed objects that used methyl cellulose as a binder, it was observed that they exhibited more significant shrinkage compared to the objects that utilized cellulose acetate. This can be partly attributed to the slower evaporation rate of the water-based solvent compared to acetone, which has a lower boiling point (56°C). Consequently, it can be concluded that employing cellulose acetate leads to superior printing results. The outcomes of the overhang print testing further substantiate this assertion. The ink comparison between reduced graphene

oxide (rGO)/methyl cellulose (MC) and reduced graphene oxide (rGO)/cellulose acetate (CA) is presented in Table 4.3.

Table 4.3 The ink comparison between reduced graphene oxide (rGO)/methyl cellulose (MC) and reduced graphene oxide (rGO)/cellulose acetate (CA).

Properties of ink	rGO/MC	rGO/CA
Solvent	Water	Acetone
Evaporate of solvent	Slow	Fast
Printed material self-sustaining	No (less than 4 hours)	Yes
Stable in aqueous electrolyte	No	Yes
Overhang print testing at 90°	No	Yes

4.2.2 Summary

From the experiments in this section, the conditions of the material and the mixture ratios used for preparing the ink with 5 wt% of rGO were identified. Additionally, an important characteristic of 3D printing, overhang print testing, was tested using bridge print testing, referred to as "bridge material print testing." This process of ink preparation is shown in Figure 4.5. The composition and conditions are crucial for developing new ink for 3D printing supercapacitor electrodes.

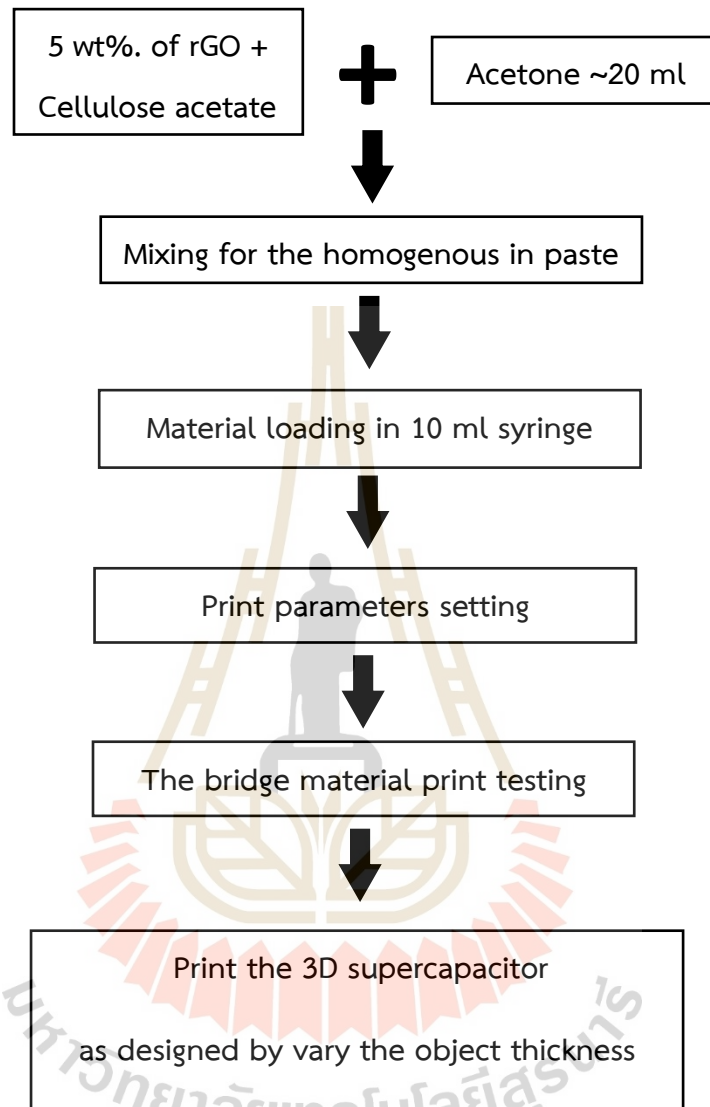


Figure 4.5 The diagram of the of rGO/CA ink preparation.

4.3 Investigating the printing parameters of 3D-printed supercapacitor electrodes

The parameters for 3D printing play a crucial role as they significantly impact the quality of the printed output. When the parameters are properly set, they contribute

to producing high-quality prints. However, if the parameters are unsuitable, they can lead to a reduction in print quality. Therefore, in this study, the parameters for 3D printing the supercapacitor electrode are similar to general 3D printer settings, with one key difference. The material extruder system is pneumatic, utilizing pressure from an air pump instead of the flow rate used in an FDM extruder. The air pressure needs to be synchronized with the printing speed. Table 4.4 presents the parameter values for 3D printing the supercapacitor electrode in this research.

Table 4.4 The optimized printing parameters.

Printing parameters	Values	Description
Layer number	Depend on model	● 4, 8, 12, 16, 20, and 24 layers
Layer height	0.15 mm	● should not exceed 80% of the nozzle diameter
Printing speed	5 mm/s	● Correlated with air flow pressure
Flow air pressure	~ 413 KPa (60 PSI).	● Correlated with material viscosity and printing speed
Printing pattern	Square shape (rectilinear pattern)	● Simple and high surface area than a solid object shape
Bed temperature	None	● No need function in this case
Print perimeters line	1 (line)	● Material purge out around the electrode before printing

In this section, the printing parameters are set according to Table 4.4, and samples with dimensions of 15 mm × 30 mm × 3 mm (LWH) were printed. These samples serve as supercapacitor electrodes made from rGO and cellulose acetate using the optimized ratio determined in section 4.2. A comparison was conducted between the 3D printing results of the electrode and the CAD-designed model using SEM images, as displayed in Figure 4.6. In Figure 4.6b, it is found that the gap is equal to 289.92 microns and the diameter of the line is equal to 351.15 microns, as evaluated in the histogram in Figure 4.7. These values are presented in Table 4.5.

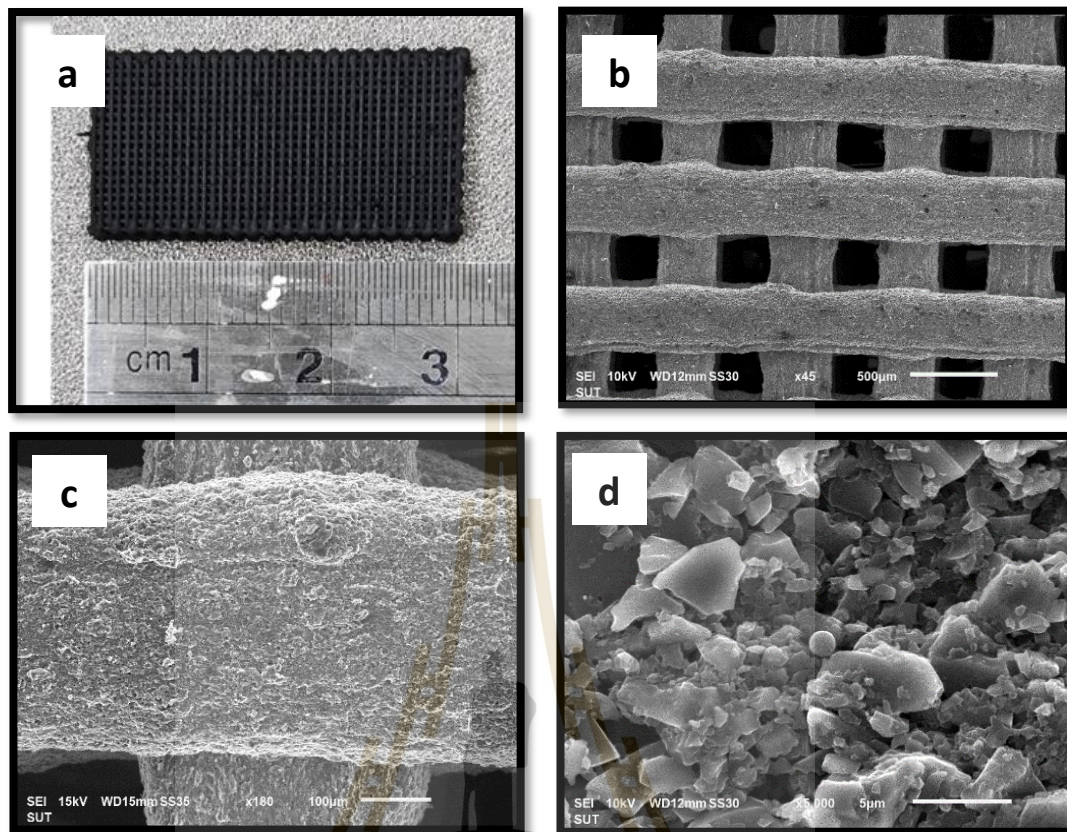


Figure 4.6 a) Photograph images of optimized 3D printing parameters with the designed dimension of 15 mm × 30 mm × 3 mm (LWH) on a nickel foam substrate; the image was recorded after the 3D printing at less than 1 hour. b), c), and d) SEM images of the 3D-printed electrode recorded after the 3D printing of more than 1 day at 45, 180, and 5000 magnifications, respectively.

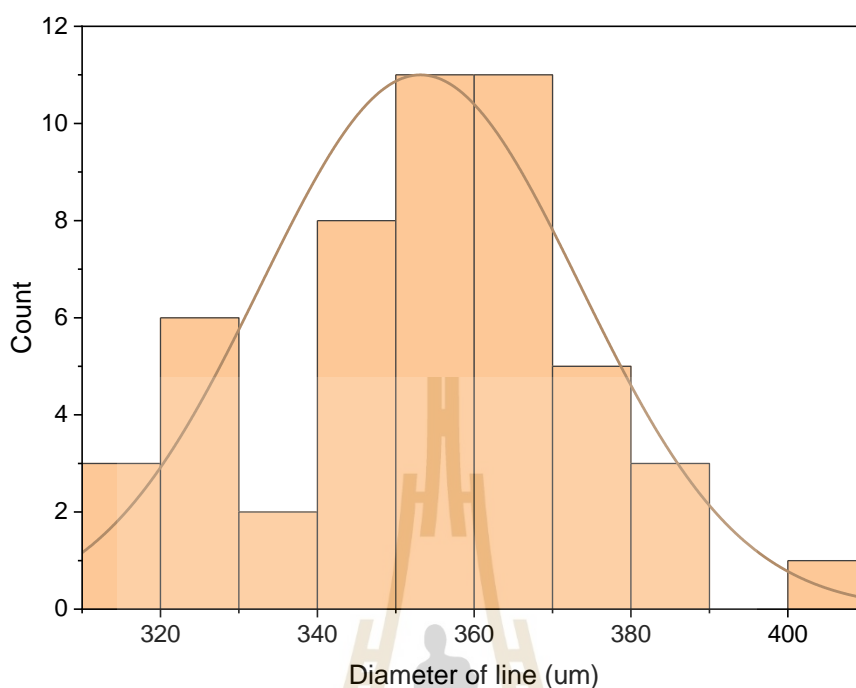


Figure 4.7 The histogram of the size distribution of 3D electrode.

Table 4.5 The observed value of the gap between line and diameter of line of 3D electrode.

Sample measurement	Average distance (μm)
Gap	282.92 ± 17.13
Diameter of line	353.15 ± 20.35

In order to apply a polyaniline coating on the surface of this 3D-printed electrode, the electrode was fabricated using a previously developed 3D printing technique with dimensions of 10 mm \times 10 mm (LW) and a designed layer height of 150 microns per layer. The electrode exhibits varying thicknesses, ranging from 4 layers, 8 layers, 12 layers, 16 layers, and 20 layers, up to a maximum of 24 layers. The relationship between the electrode thickness and its mass is illustrated in Figure 4.8 and Table 4.6. Subsequently, these electrodes with different thicknesses will undergo

testing under various conditions as part of the experiment involving the application of the polyaniline coating.

Table 4.6 The comparison between the layer number of 3D-printed electrode and their height with electrode mass.

Layer	Electrode mass (mg)	Electrode designed height (mm)	Electrode area (cm ²)
4	13.0 ± 1.2	0.6	1.24
8	22.3 ± 1.6	1.2	1.35
12	36.4 ± 3.4	1.8	1.46
16	45.5 ± 2.7	2.4	1.57
20	58.6 ± 1.7	3.0	1.68
24	72.9 ± 3.5	3.6	1.79

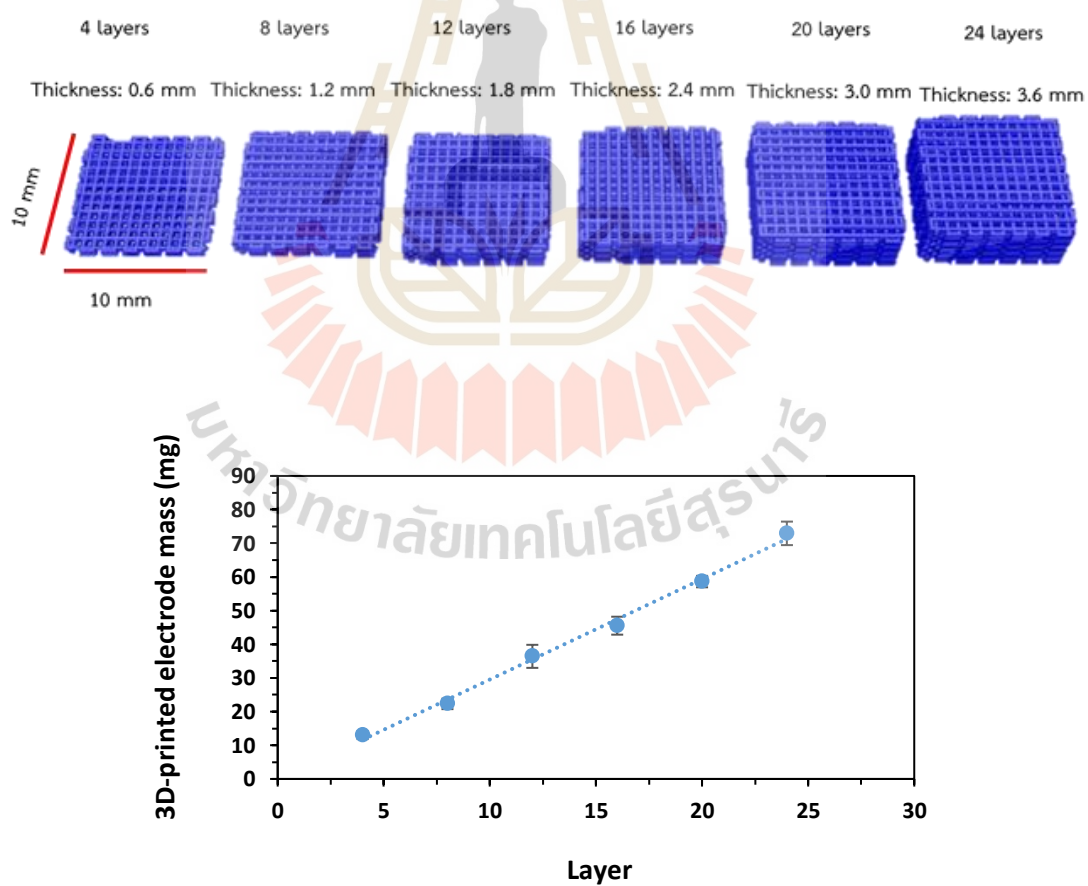


Figure 4.8 Graph shows the relationship between printed layer and the mass of 3D-printed electrode.

4.3.1 Discussion

The SEM images show that the model's size differs from the actual printed object after approximately one day. The size difference indicates that the printed object is smaller than the model's 10 mm × 10 mm (LW). After one day of printing, the size is reduced to 7.5 mm × 7.5 mm (LW), resulting in an estimated percentage change of approximately 25%. These experimental results can be recalculated for the printed line. The SEM image showed an average printed line size of 353 microns, smaller than the nozzle diameter of 400 microns. By comparing the 25% difference between the printed object and the model, it can be calculated that the line size is approximately 441 microns. However, the line size tends to be smaller when the nozzle moves faster or the printing speed increases. Conversely, a slower nozzle movement results in a larger line size. Therefore, maintaining a consistent printing speed is crucial to ensure high-quality and continuous printing.

Additionally, one factor that contributes to the reduced size of the printed object compared to the model could be the evaporation of acetone, a solvent. The evaporation of acetone after one day of printing leads to increased material compaction, resulting in a change in the size of the printed object.

4.3.2 Summary

The optimized parameters for DIW 3D printing in this study were investigated, as shown in Table 4.4, and the printing results were successful. After one day of printing, the acetone solvent in the printed object completely evaporates, causing it to shrink by approximately 25%. Therefore, the model should be approximately 25% larger than the desired final size when designing the printed object to compensate for the shrinkage during printing. As shown in Figure 4.8, the number of layers of the 3D-printed supercapacitor electrode increases, leading to a linear increase in the mass of the 3D-printed supercapacitor electrode.

4.4 Synthesizing and coating PANI on 3D-printed supercapacitor electrodes

The synthesis of PANI in this work is conducted via a chemical polymerization process, which involves the oxidation of aniline monomers, resulting in the formation of a polymer chain. Aniline monomers are mixed with an oxidizing agent using the oxidative polymerization approach. In this work, the oxidant used in PANI synthesis is ammonium persulfate (APS). The oxidizing agent initiates the polymerization process by oxidizing aniline and generating free radicals, leading to the growth of the polymer chain. When the aniline monomer is mixed with ammonium persulfate, chemical polymerization occurs, and the solution's color changes from colorless to green, as shown in Figure 4.9.

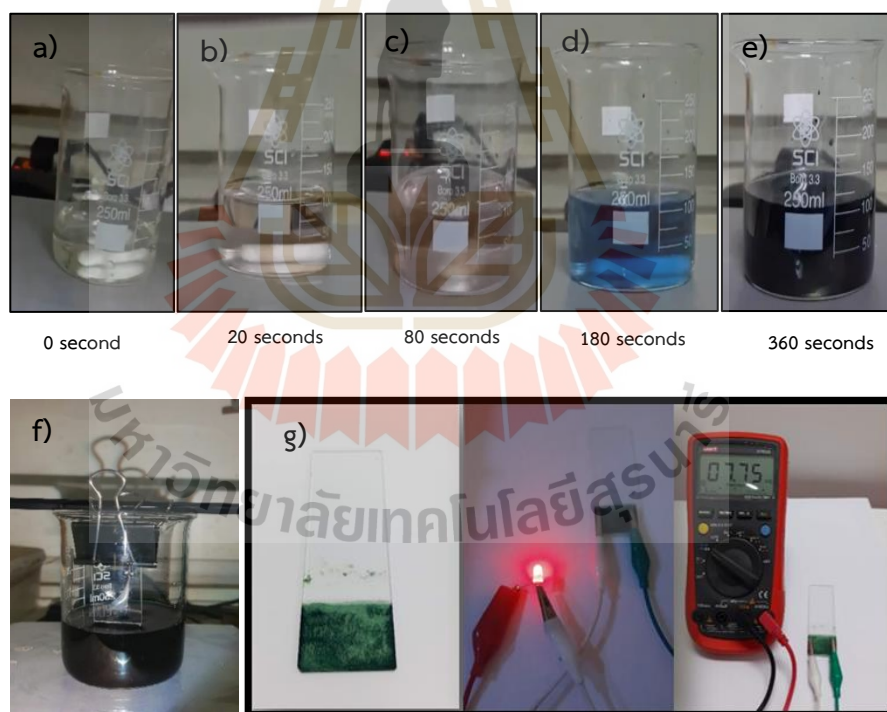


Figure 4.9 PANI synthesis by chemical oxidative polymerization (COP). Change of solution color of aniline polymerization at a) 0 second, b) 20 seconds, c) 80 seconds, and d) 180 seconds, and e) 360 seconds, f) PANI deposition on glass slide. g) The PANI resistive testing.

The color change during the process of chemical oxidative polymerization can indicate the growth of the conductive polymer chain, with each solution color having distinct properties.

- White/clear or colorless if the polymer form is leucoemeraldine and the polymer type is pernigraniline.
- Blue to violet if the polymer form is emeraldine base.
- Green if the polymer form is emeraldine salt, which is the conductive polymer.

Figure 4.9 shows that PANI is obtained through a synthesis process when the substance is mixed for 360 minutes. The color of the solution changes from colorless to pink, then transitions to blue, and finally transforms into a deep green color. This experimental result aligns with the characteristics of PANI in the form of emeraldine salt, indicating its ability to conduct electricity. A simple approach can be used to test the electrical conductivity of this solution. Immerse a non-conductive material, such as a glass slide, into the solution as shown in Figure 4.9f. Subsequently, the resistance value is measured, and an attempt is made to connect it to an electrical circuit using the coated glass slide as a bridge. If the coated glass slide conducts electricity, the electric current will flow in a complete circuit, illuminating a red LED light, as shown in Figure 4.9g. This experiment enables us to determine the electrical conductivity of the green-coated material on the glass slide. To validate the identity of the synthesized material as polyaniline (PANI), we can conduct a confirmation analysis using X-ray diffraction (XRD) and scanning electron microscopy (SEM).

4.4.1 X-ray diffraction (XRD) of polyaniline (PANI)

The XRD pattern of the synthesis PANI in Figure 4.10 was measured with Cu, $K\alpha$ wavelength of 1.54 \AA between 2θ from 10° to 60° , time step of 0.5 and the step size of 0.02. The XRD pattern of the sample shows the broad peak of amorphous PANI about $2\theta = 20.65^\circ$ and 25.19° corresponding to crystal plane 020 and 200 respectively, which diffraction peak is corresponding with other works (Vadiraj *et al.*, 2015, Srinivas *et al.*, 2012) and can confirm that the synthesized material is polyaniline.

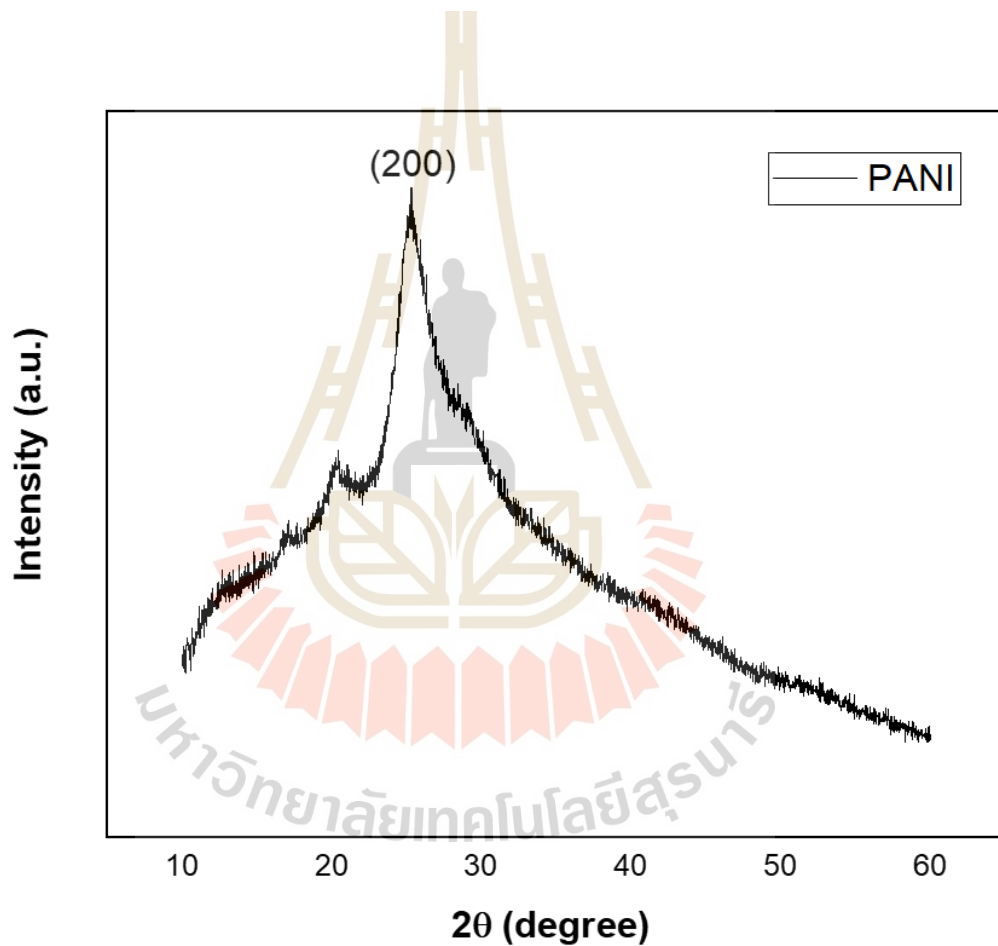


Figure 4.10 XRD pattern of the synthesized PANI using COP method.

4.4.2 Scanning electron microscope (SEM) of polyaniline (PANI)

The electrodes with varying thicknesses were previously fabricated. Subsequently, they were coated with PANI using different numbers of cycles, ranging from 1 to 5 cycles, to achieve films with thicknesses corresponding to the number of coating cycles. SEM images from the top view, as depicted in Figure 4.11, reveal the presence of gaps within the electrodes. The size of these gaps, quantified by the histogram, is about $284 \pm 34 \mu\text{m}$, as shown in Figure 4.12. Additionally, the cross-sectional SEM analysis provides information on the thickness of the PANI film based on the number of coating cycles, as shown in Figure 4.14.

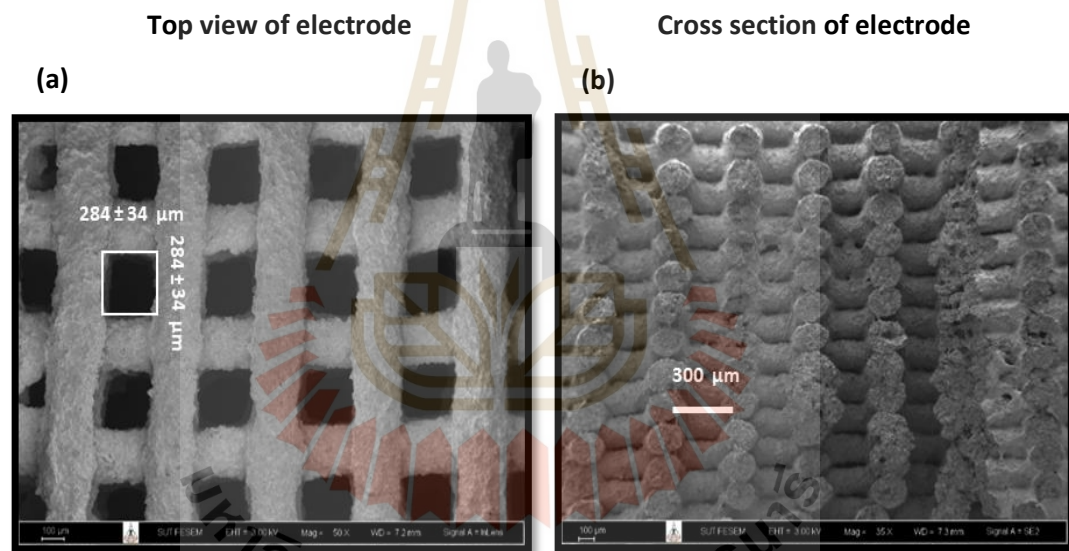


Figure 4.11 a) The top view SEM image of 3D-printed electrode. b) The cross section of 3D-printed electrode.

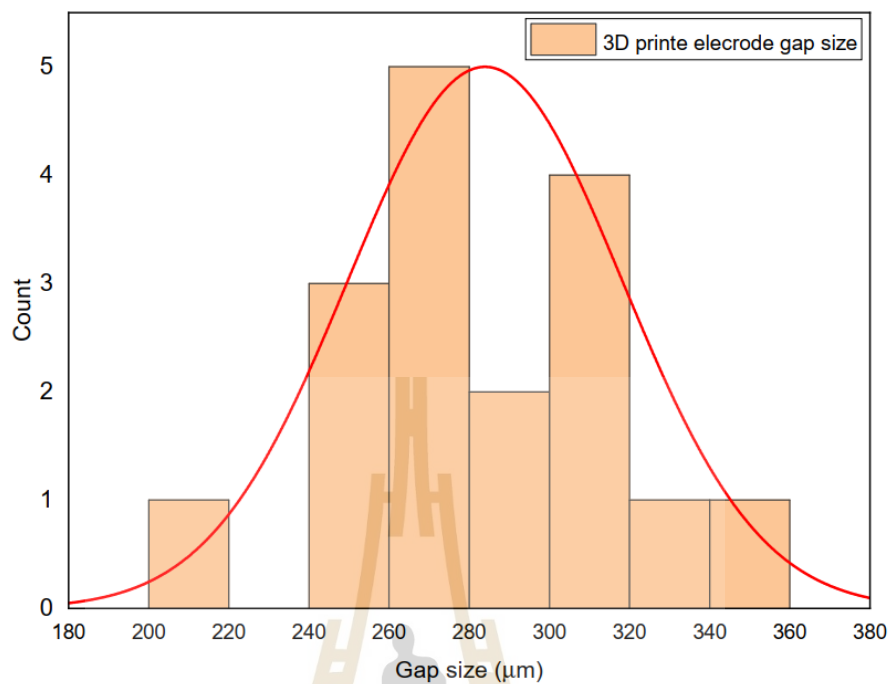


Figure 4.12 The histogram of the gap size in 3D-printed electrode.

SEM was used to study the morphology of polyaniline. The SEM results reveal the presence of a nano-sized network structure. As shown in Figure 4.13, the average nanofiber size is about 46.66 ± 5.50 nm, which significantly influences the surface area of polyaniline. By increasing the surface area, the PANI-coated 3D-printed electrode will exhibit a larger contact area with the electrolyte, enhancing their interaction.

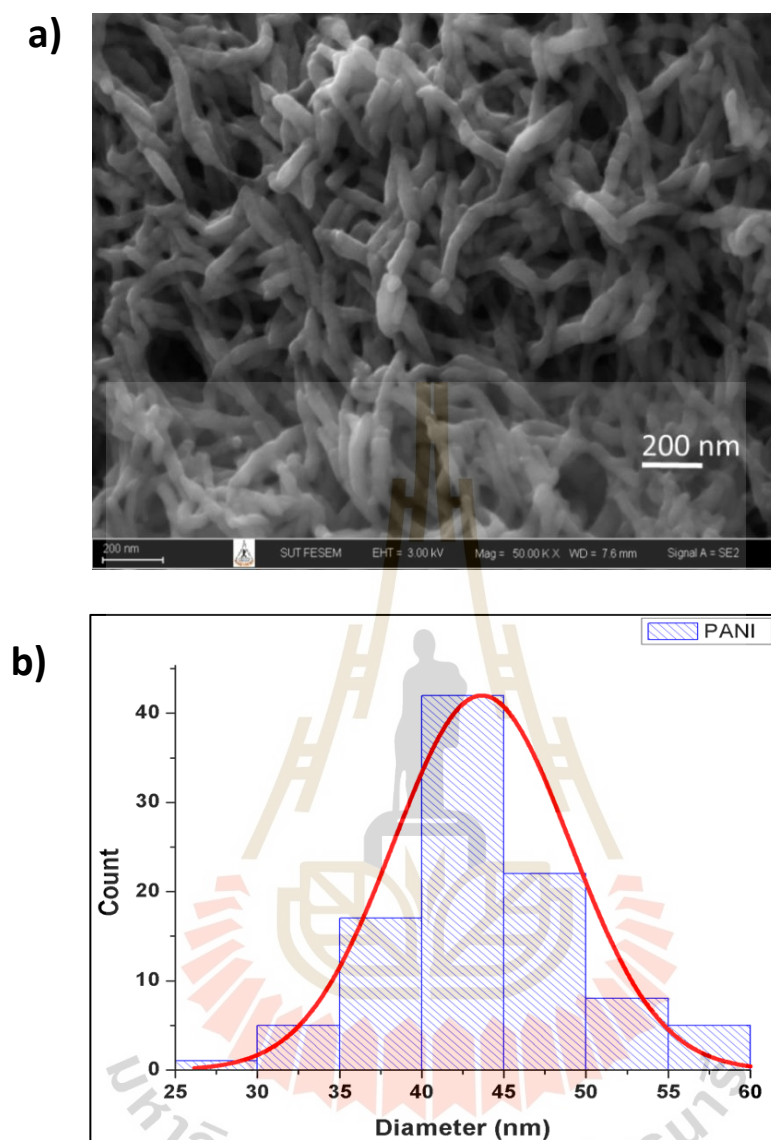


Figure 4.13 a) SEM image of PANI nanofibrous network. b) The histogram of PANI nanofiber diameter of 46.66 ± 5.50 nm.

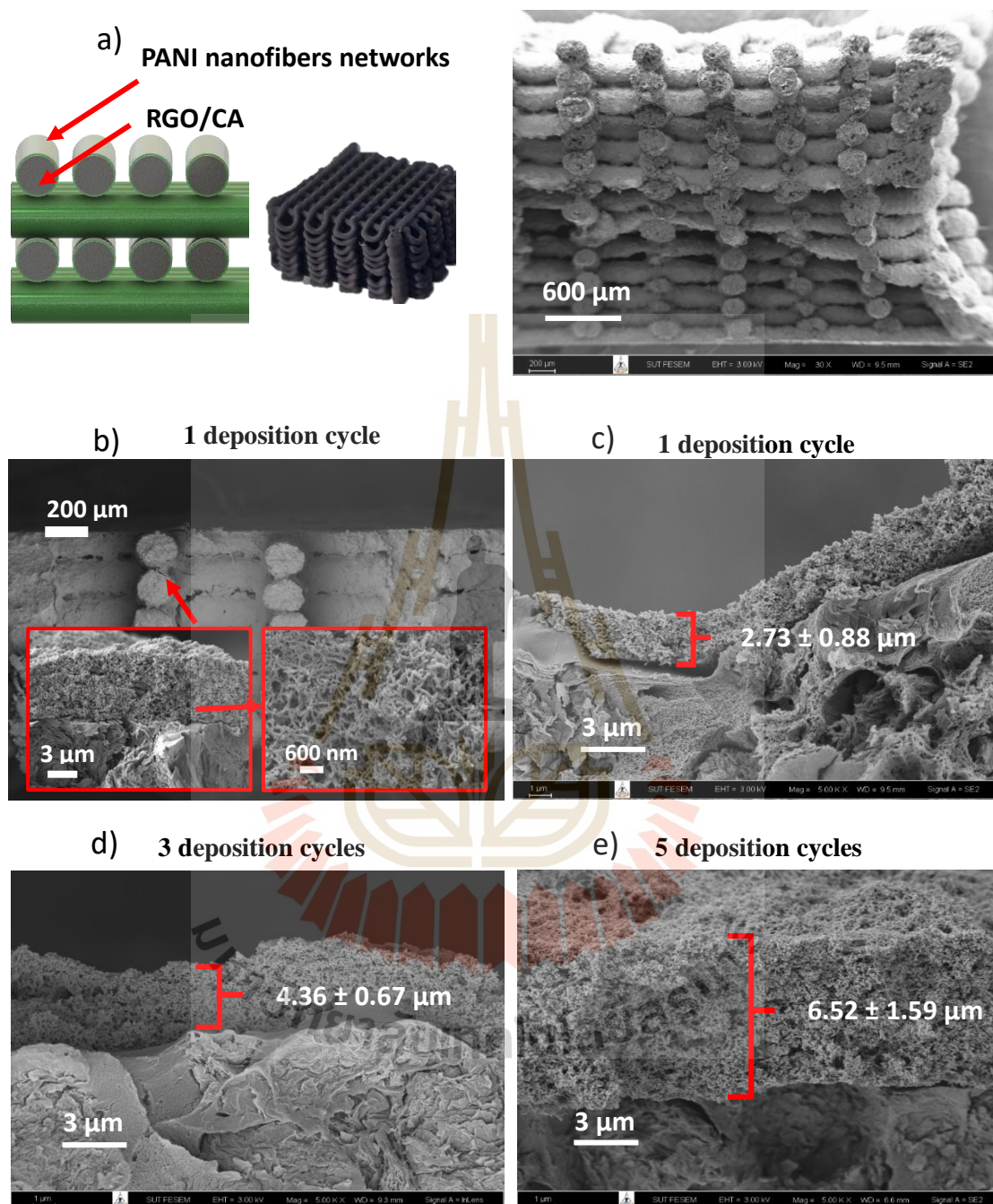


Figure 4.14 The cross section of 24 layers 3D-printed electrode with different deposition cycle. a-b) SEM cross section of rGO/PANI 3D-printed c) 1 deposition cycle, d) 3 deposition cycles, and e) 5 deposition cycles.

From Figure 4.14, the polyaniline film thickness increases with the number of deposition cycles, and the result of this relationship is presented in Table 4.7 and Figure 4.15.

Table 4.7 PANI film thickness with deposition cycle number.

PANI deposition cycle	PANI film thickness (μm)
1	2.73 ± 0.88
3	4.36 ± 0.67
5	6.52 ± 1.59

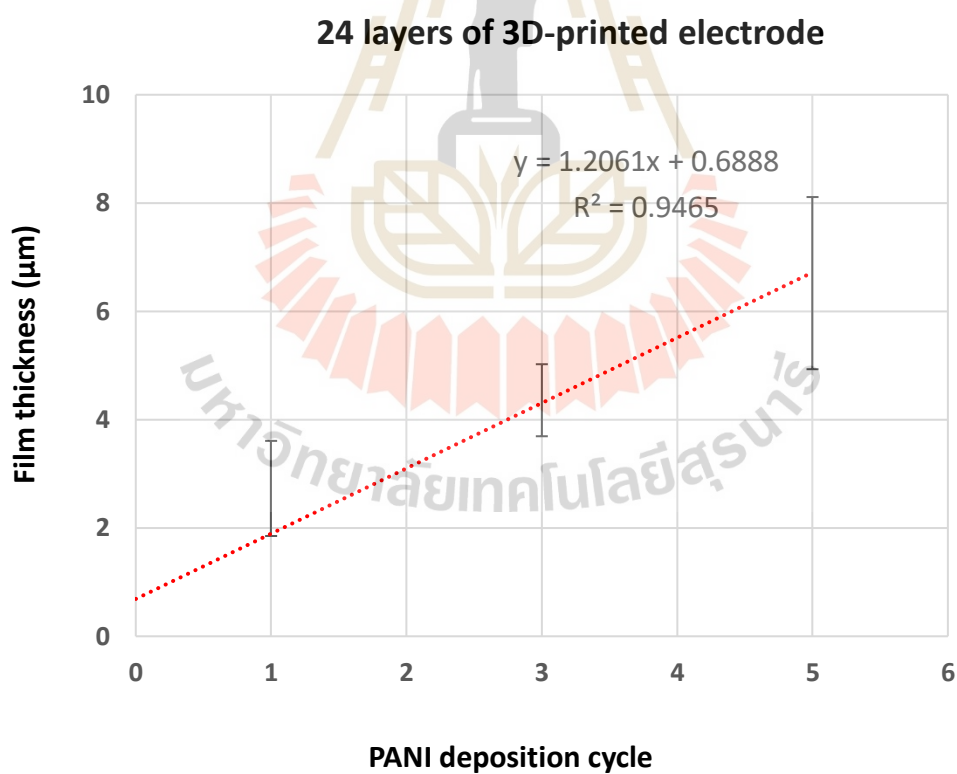


Figure 4.15 The graph shows the relationship between PANI deposition cycle number and film thickness.

Additional experimental results revealed that as the electrode thickness increases, the amount of PANI coating on the electrode surface correspondingly increases. This relationship is illustrated in Table 4.8 and Figure 4.16.

Table 4.8 The relationship between 3D-printed electrode thickness and PANI mass in 1 deposition cycle.

Electrode thickness (mm)	PANI mass (mg)
0.37	0.12 ± 0.05
0.75	0.15 ± 0.06
1.12	0.21 ± 0.04
1.49	0.32 ± 0.05
1.87	0.36 ± 0.08
2.24	0.52 ± 0.12

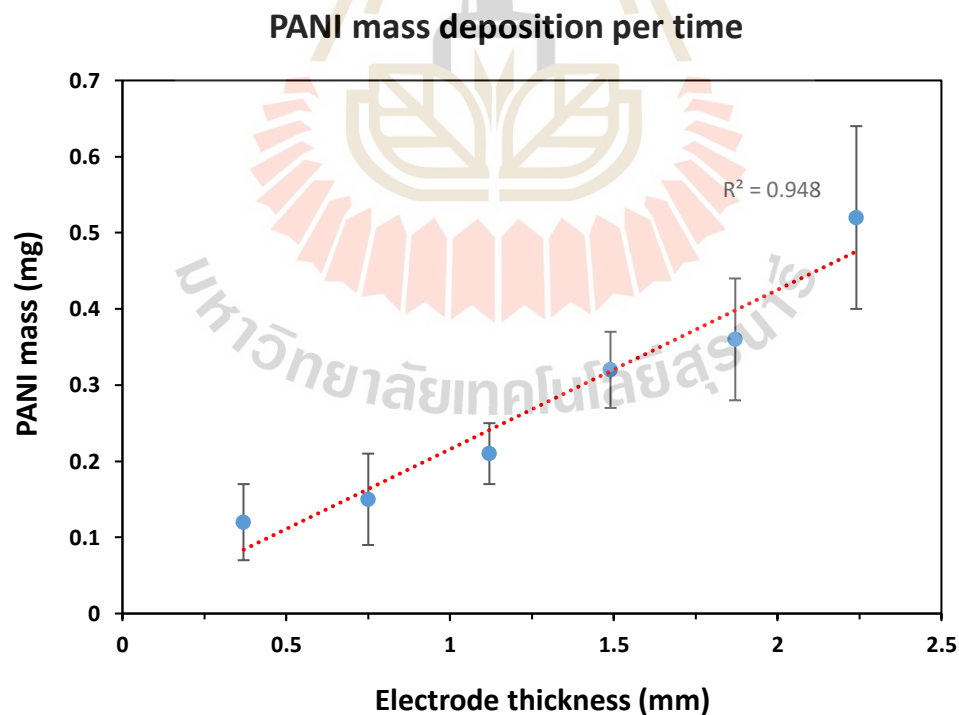


Figure 4.16 The relationship between 3D-printed electrode thickness and PANI mass in 1 deposition cycle.

4.4.3 Discussion

The synthesis of polyaniline (PANI) through chemical oxidative polymerization was successful, and its conductive properties were confirmed by coating PANI on a glass slide, a non-conductive material. After the coating, the glass slide became conductive and was tested using a direct circuit as a bridge. As shown in Figure 4.9, the results demonstrate that the LED is bright. XRD shows the broad peaks of amorphous PANI at about $2\theta = 20.65^\circ$ and 25.19° , corresponding with other work (Vadiraj *et al.*, 2015 and Srinivas *et al.*, 2012). In the SEM image in Figure 4.13, it was observed that PANI with a nanofiber network structure exhibits a highly complex arrangement. This unique structure leads to the formation of small nanoscale voids, thereby increasing the surface area of polyaniline. This discovery aligns with a study conducted by Haihui *et al.*, in 2005, which investigated the structure of polyaniline and its influence on supercapacitor performance. Their study found that the nanofiber network structure yields higher capacitance than particle and film structures.

When coating PANI on the 3D-printed electrode, it was observed that the number of deposition cycles impacts the thickness of the PANI film. Additionally, the electrode thickness correlates with the amount of PANI deposited, which is proportional to the surface area. Within the PANI film, a network of numerous nanofibers is present, with the thickest film observed at 5 deposition cycles. This unique structure is expected to contribute to the highest capacitive value, consistent with the findings of Haihui's work in 2005.

4.4.4 Summary

The electrical conductivity of PANI was tested by applying the synthesized material onto a glass slide and using it as an electrical bridge in a direct current circuit. X-ray diffraction (XRD) measurements were performed to identify diffraction peaks, and scanning electron microscopy (SEM) was used to observe its intrinsic characteristics. These tests confirmed the presence of the desired properties in polyaniline (PANI), the material intended for fabricating a supercapacitor electrode. The successful coating of PANI onto the surface of the 3D-printed electrode opens up possibilities for enhancing capacitance through the synergistic properties of rGO and PANI.

4.5 Studying the electrochemical properties of 3D-printed supercapacitor electrodes

4.5.1 3D-printed rGO supercapacitor electrode at fixed electrolyte soaking time

4.5.1.1 Cyclic voltammetry measurement

Studies of the electrochemical properties of the rGO 3D-printed electrode using cyclic voltammetry and galvanostatic charge/discharge were conducted. The CV curves of rGO were examined within a potential range from -0.9V to 0.4V with a scan rate of 5 mV/s in 3M KOH electrolyte using a three-electrode system at room temperature, as shown in Figure 4.17. Before the measurement, the electrode had to soak in the electrolyte. Generally, the soaking time for a conventional 2D electrode is about 6 to 12 hours. Therefore, the 3D electrode was soaked for 1 day to increase the likelihood of the electrolyte covering the 3D electrode surface.

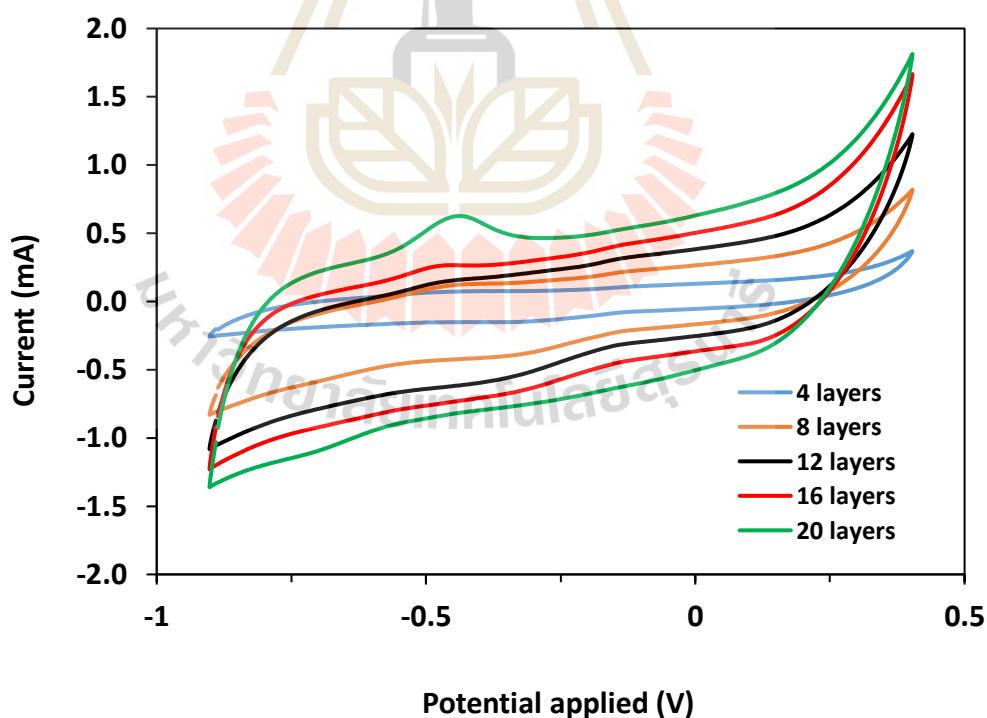


Figure 4.17 CV curve of 3D-printed rGO electrode of 4 layers, 8 layers, 12 layers, 16 layers, and 20 layers with potential -0.9V to 0.4V, scan rate 5 mV/s.

The comparative CV curve of 3D-printed rGO electrodes, consisting of 4 layers and 20 layers, is presented in Figure 4.18. In this CV curve, the 4 layers 3D-printed electrode exhibits an areal capacitance of 14.29 mF/cm², while the 20 layers 3D-printed electrode shows an areal capacitance of 67.63 mF/cm², as shown in Table 4.9 and Figure 4.19. These results indicate that the areal capacitance of the 20 layers 3D-printed electrode is approximately 4.7 times higher than that of the 4 layers 3D-printed electrode.

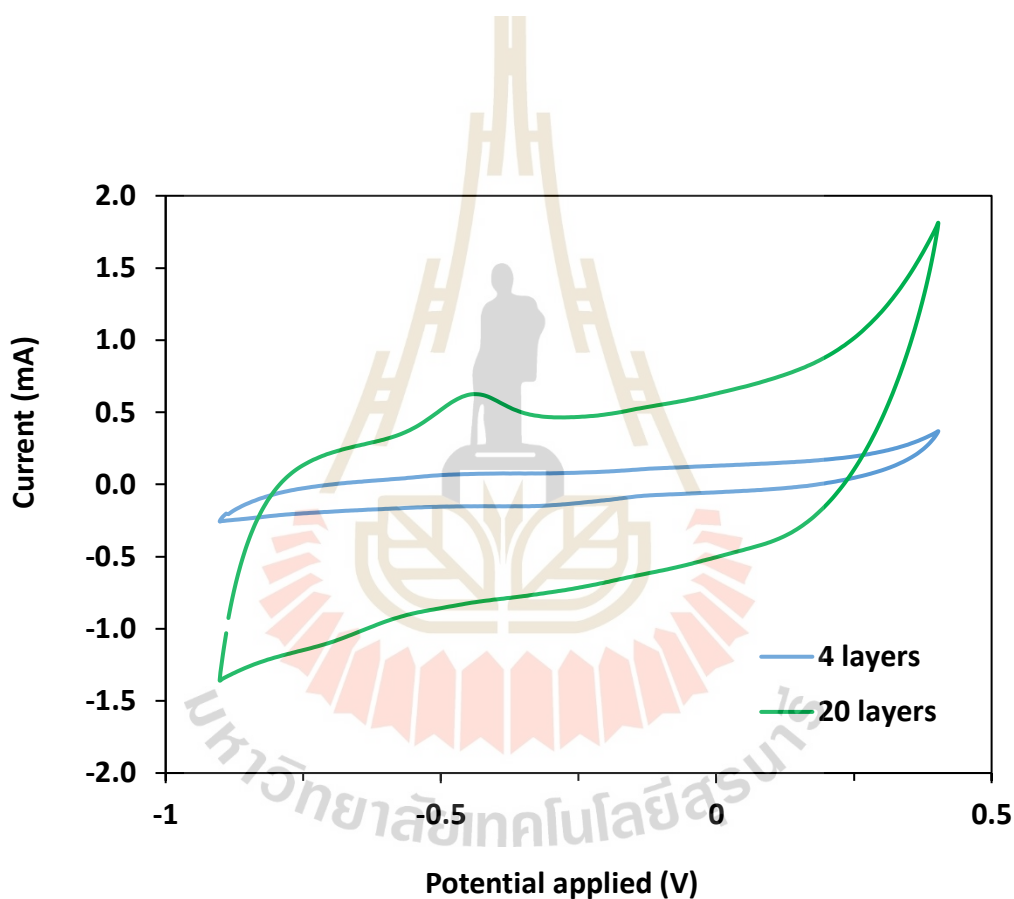


Figure 4.18 CV curve of 3D-printed rGO electrode of 4 layers and 20 layers with potential -0.9V to 0.4V, scan rate 5 mV/s.

Table 4.9 The areal capacitance of rGO 3D-printed electrodes from CV measurement.

Soaking day	Layers	mF/cm ²
1	4	14.29
	8	41.10
	12	52.30
	16	60.43
	20	67.63

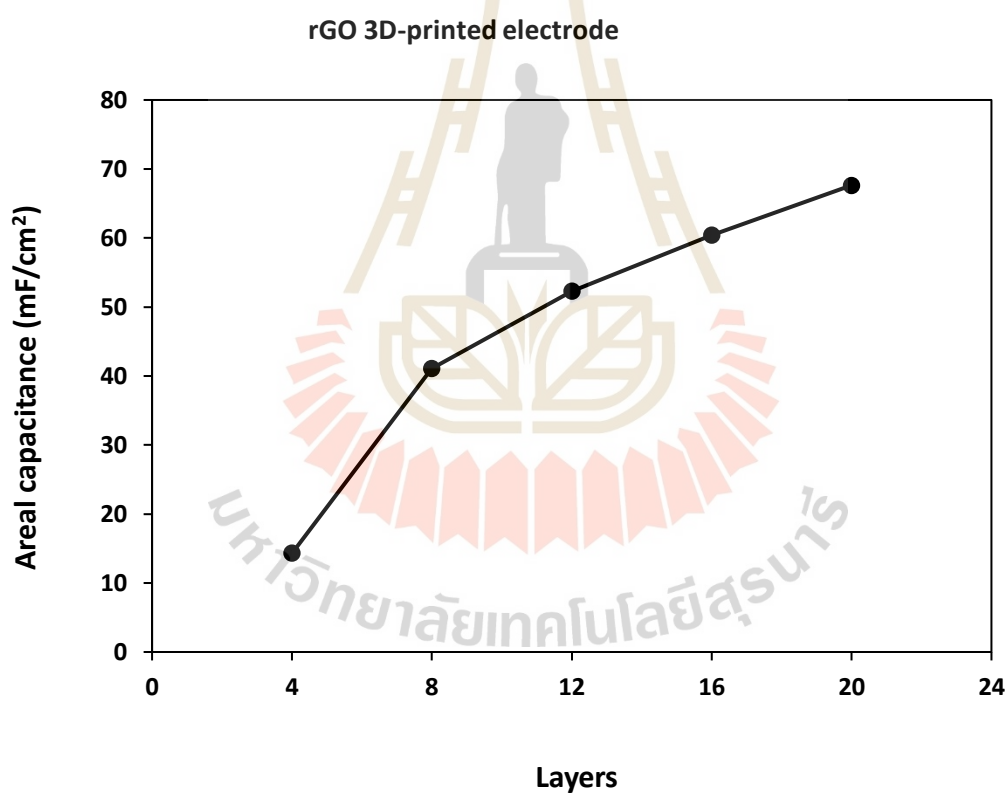


Figure 4.19 CV curve comparison capacitance of 3D-printed rGO electrode of 4 layers, 8 layers, 12 layers, 16 layers, and 20 layers with potential -0.9V to 0.4V, scan rate 5 mV/s.

4.5.1.2 Galvanostatic charge-discharge measurement

The comparative CV curve of 3D-printed rGO electrodes, consisting of 4 layers and 20 layers, is presented in Figure 4.18. In this CV curve, the 4 layers 3D-printed electrode exhibits an areal capacitance of 14.29 mF/cm², while the 20 layers 3D-printed electrode shows an areal capacitance of 67.63 mF/cm², as shown in Table 4.9 and Figure 4.19. These results indicate that the areal capacitance of the 20 layers 3D-printed electrode is approximately 4.7 times higher than that of the 4 layers 3D-printed electrode.

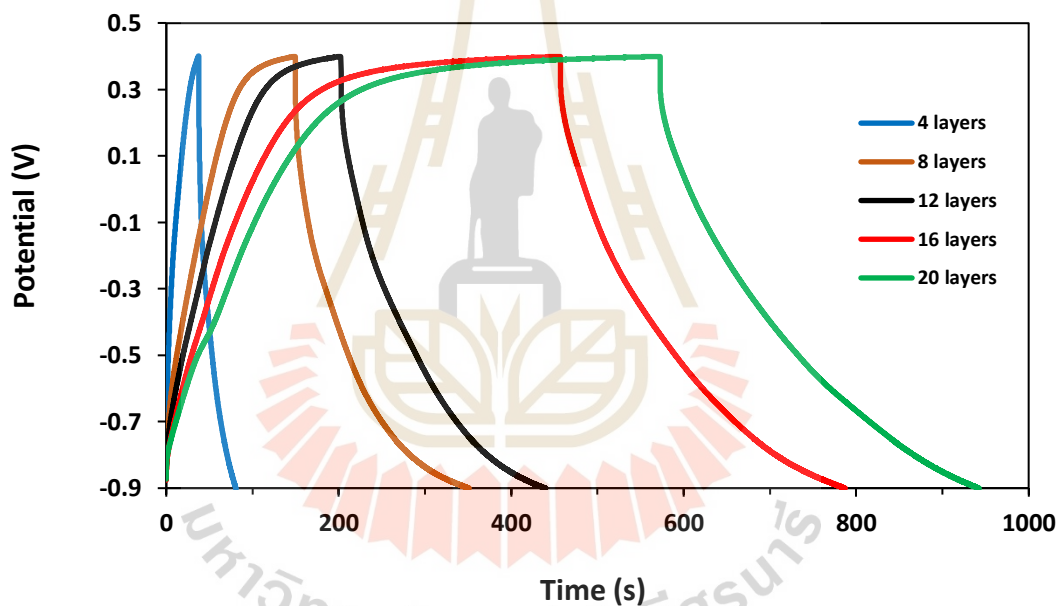


Figure 4.20 GCD curve of 3D-printed rGO electrode of 4, 8, 12, 16, and 20 layers at current density 1 mA/cm² and potential -0.9V to 0.4V.

Table 4.10 The areal capacitance of rGO 3D-printed electrodes from GCD measurement.

Soaking day	Layers	mF/cm ²
1	4	17.32
	8	80.95
	12	94.57
	16	131.23
	20	147.52

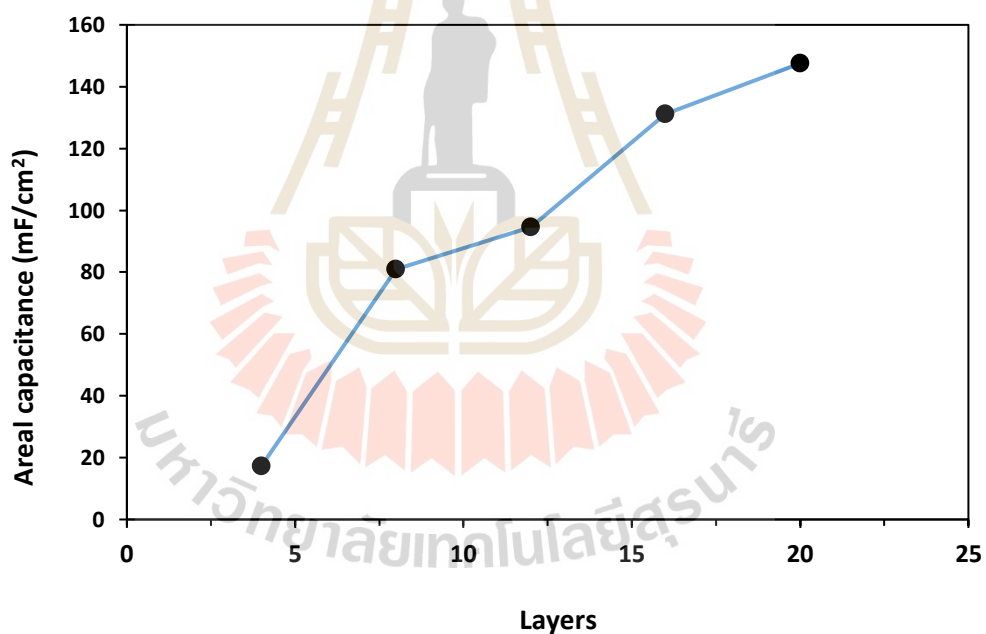


Figure 4.21 GCD curve comparison capacitance 3D-printed rGO electrode of 4, 8, 12, 16, and 20 layers at current density 1 mA/cm² and potential -0.9V to 0.4V.

4.5.1.3 Electrochemical impedance spectroscopy measurement

Electrochemical impedance spectroscopy (EIS) presents the behavior of 3D-printed electrodes as shown in Figure 4.22. The solution resistance (R_s), interpreted from the intercept at the Z' axis or the minimum value at high frequency, indicates that all samples have Z' values around 2.5 ohms, except for the 8 layers 3D-printed electrode, which has a Z' value around 3 ohms, as shown in Table 4.11. However, at low frequency, the Nyquist plot shows the slope from highest to lowest for the 4, 8, 12, 16, and 20 layers, respectively. The slope of the line in the low-frequency region measures Warburg impedance or diffusion resistance. These results indicate that the 4 layers 3D-printed electrode is the most accessible for ion adsorption onto the electrode surface.

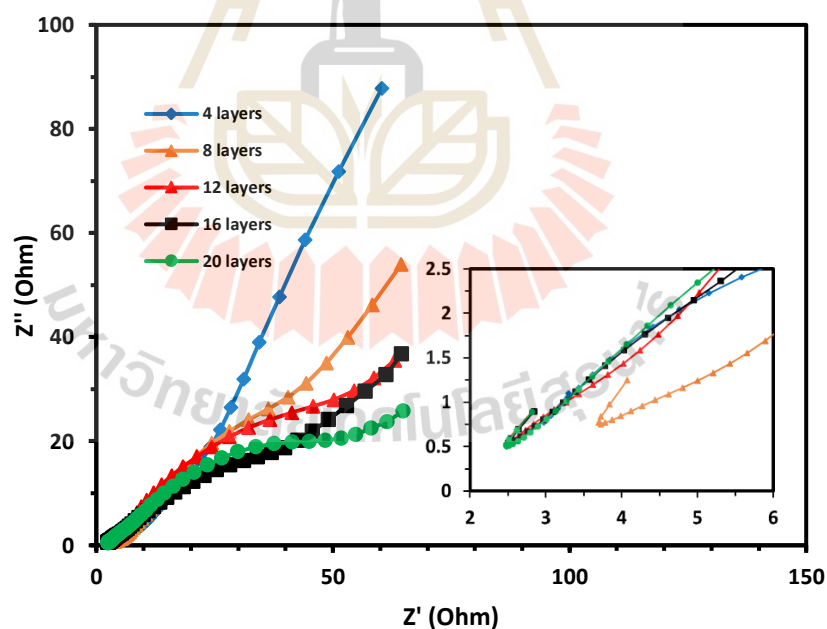


Figure 4.22 The Nyquist plot of a 3D-printed rGO electrode with 4, 8, 12, 16, and 20 layers that have been soaked in electrolyte for 1 day. The inset image shows this Nyquist at high frequency.

Table 4.11 The solution resistance (R_s) of 4, 8, 12, 16, and 20 layers 3D-printed rGO electrode.

Soaking time (day)	Layers	R_s (Ω)
1	4	3.05
	8	2.49
	12	2.47
	16	2.50
	20	2.48

4.5.1.4 Discussion

Based on experimental measurements of the areal capacitance of 3D-printed rGO electrodes at different layer counts, consistent results were obtained from CV and GCD measurements. Specifically, the areal capacitance values obtained at 4 layers were 14.29 mF/cm² (CV) and 17.32 mF/cm² (GCD). In contrast, the areal capacitance values obtained at 20 layers were 67.63 mF/cm² (CV) and 147.52 mF/cm² (GCD). The observed increase in areal capacitance from 4 to 20 layers in both measurements is proportional to the number of printed layers. This suggests that the enhanced areal capacitance may be attributed to the increased surface area of the printed electrode, which is likely the main contributing factor.

4.5.1.5 Summary

The electrochemical properties of rGO 3D-printed electrodes with 4, 8, 12, 16, and 20 layers were examined using CV, GCD, and EIS. All electrodes were soaked in 3M KOH for 1 day. The results showed that the areal capacitance increased with the electrode thickness. The thickness of the electrode directly influenced its surface area, which had a more significant impact than resistance, leading to a higher areal capacitance for the 20 layers 3D-printed electrode compared to the 4 layers 3D-printed electrode. However, the number of printing layers is limited because if the 3D electrode is too thick, it results in high resistance and weak mechanical stability.

4.5.2 3D-printed rGO supercapacitor electrode with vary electrolyte soaking time

4.5.2.1 Cyclic voltammetry measurement

The objective of this section was to examine the influence of electrolyte soaking time on areal capacitance. To achieve this, the experiments followed the same procedure outlined in section 4.5.1, with the only variation being the duration of electrolyte soaking. Specifically, the electrolyte soaking time was varied for 1, 2, 3, 4, and 11 days. The primary focus of this section was to analyze the relationship between different electrolyte soaking durations and their effect on areal capacitance. Figure 4.23 compares the CV curves of 8 layers rGO 3D-printed electrodes with electrolyte soaking times of 1, 2, 3, 4, and 11 days. The CV curves are almost the same, with an average areal capacitance of 31.16 ± 1.79 mF/cm², and the areal capacitance from CV is presented in Table 4.12 and Figure 4.24.

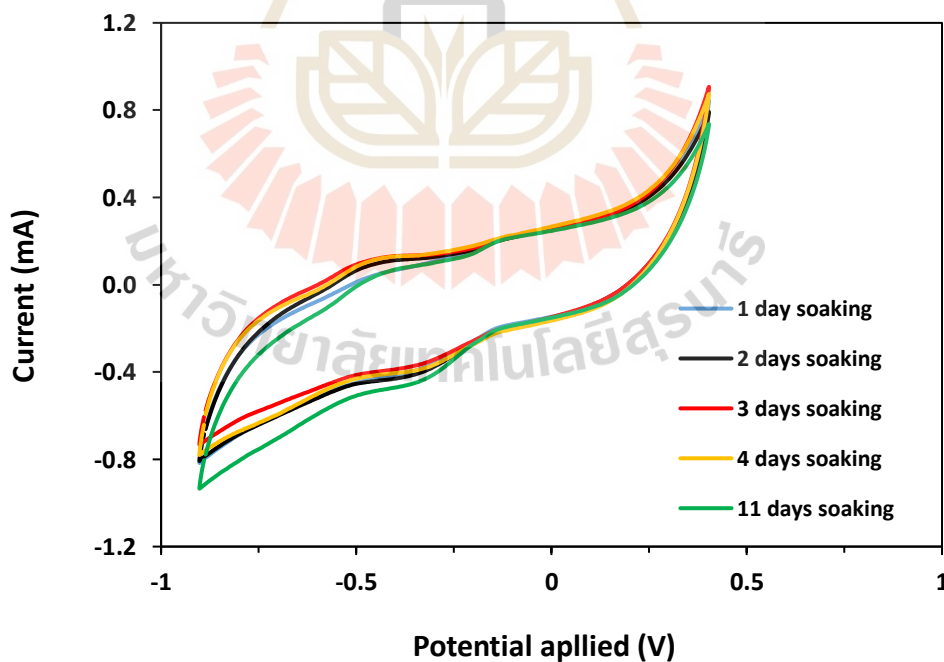


Figure 4.23 CV curve of 3D-printed rGO electrode of 8 layers, which vary the electrolyte soaking time with potential -0.9V to 0.4V, scan rate 5 mV/s.

Table 4.12 The areal capacitance of 8 layers rGO 3D-printed electrodes with varying soaking time from CV measurement.

Layers	Soaking day	mF/cm ²
8	1	30.62
	2	30.55
	3	28.60
	4	32.02
	11	34.00

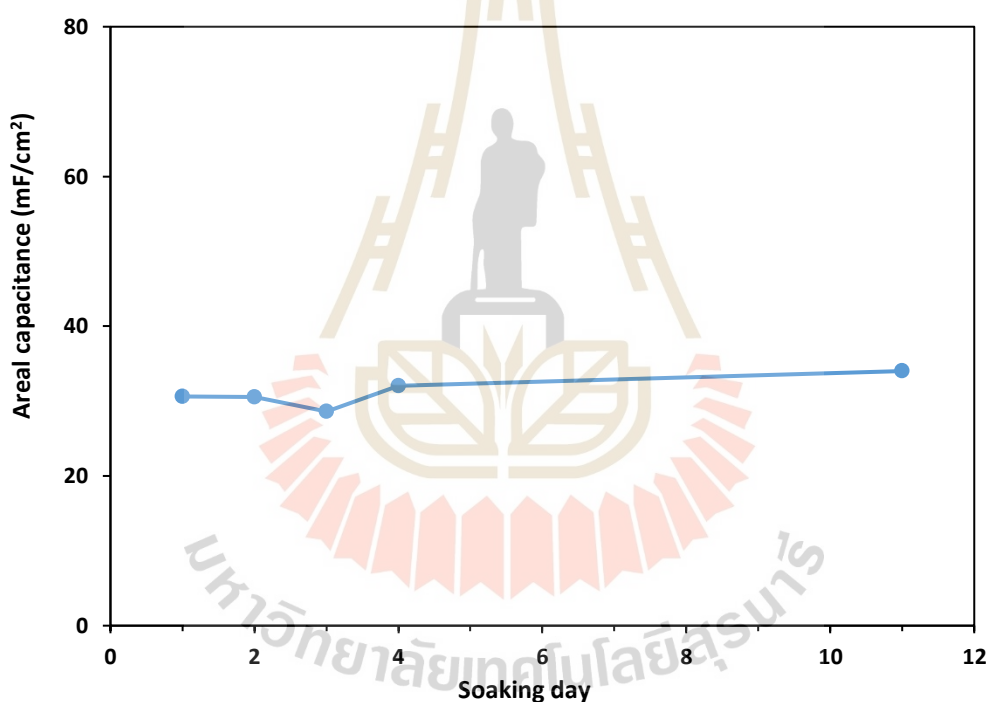


Figure 4.24 Comparison of CV curves for the areal capacitance of 8 layers rGO 3D-printed electrodes with varying electrolyte soaking times.

4.5.2.2 Galvanostatic charge-discharge measurement

The galvanostatic charge-discharge behavior of 8 layers 3D-printed electrodes was measured at a current density of 1 mA/cm² under electrolyte soaking times of 1, 2, 3, and 4 days. GCD curves are presented in Figure 4.25. The GCD curves for 1 and 4 days of soaking time are the same, and the GCD curves were used to

calculate the areal capacitance, as shown in Table 4.13 and Figure 4.26. The areal capacitance from GCD is an almost constant value with an average of 54.86 ± 6.82 mF/cm².

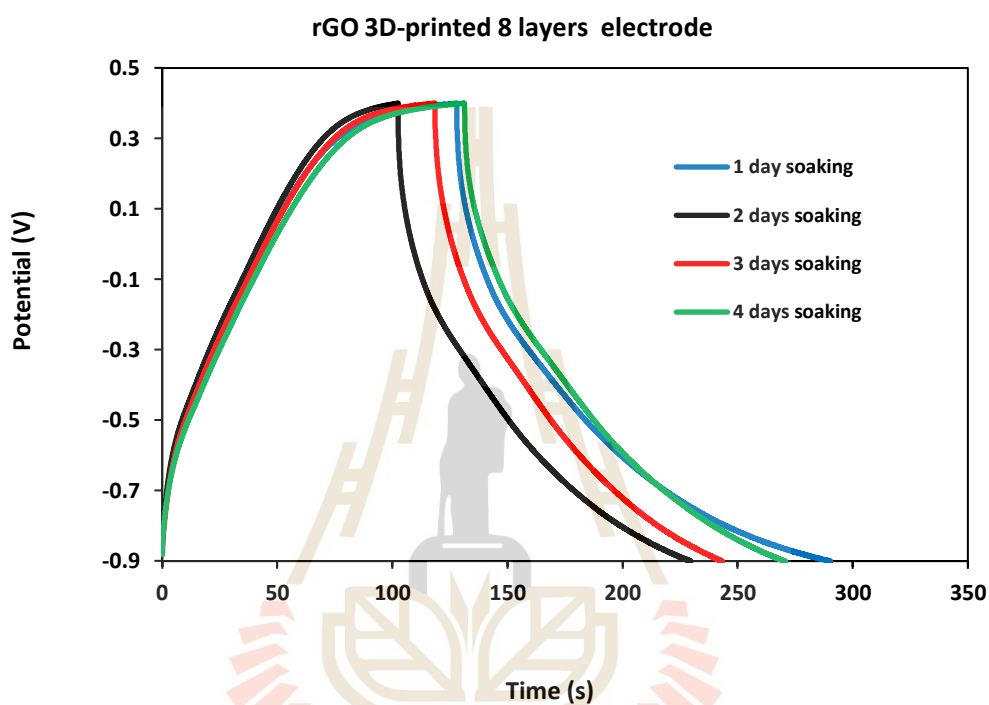


Figure 4.25 GCD curve of 8 layers 3D-printed electrodes was measured at a current density of 1 mA/cm^2 under the condition of electrolyte soaking time 1, 2, 3, and 4 days and potential -0.9V to 0.4V .

Table 4.13 The areal capacitance of 8 layers rGO 3D-printed electrodes with varying soaking time from GCD measurement.

Layers	Soaking day	mF/cm ²
8	1	64.37
	2	50.76
	3	49.20
	4	55.12

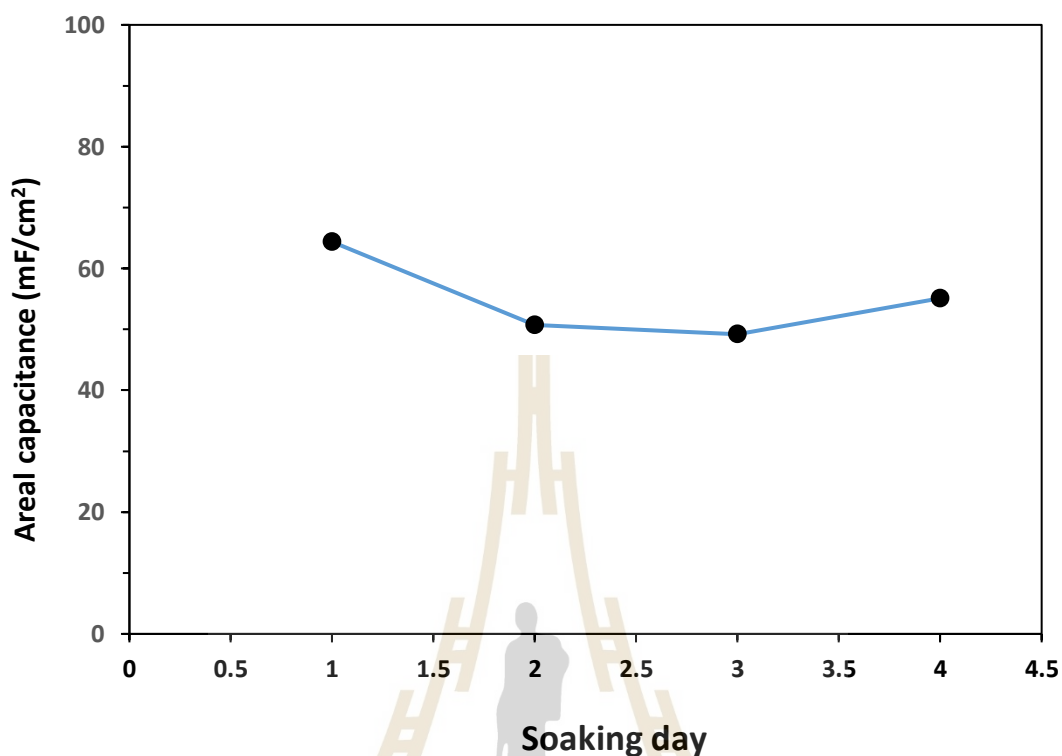


Figure 4.26 The comparison of GCD curves for the areal capacitance of 8 layers rGO 3D-printed electrodes with varying electrolyte soaking times.

4.5.2.3 Electrochemical impedance spectroscopy measurement

Electrochemical impedance spectroscopy (EIS) presents the behavior of 8 layers rGO 3D-printed electrodes as shown in Figure 4.27. The solution resistance (R_s), interpreted from the intercept at the Z' axis or the minimum value at high frequency, indicates that all samples have Z' values around 2.82 ± 0.19 ohms, except for the electrode soaked for 11 days, which has a Z' value around 3 ohms, as shown in Table 4.14. In Figure 4.27, the Nyquist plot of 2 and 11 days soaking time is not different at low frequencies; similarly, the curves for 1 and 4 days of electrolyte soaking are the same.

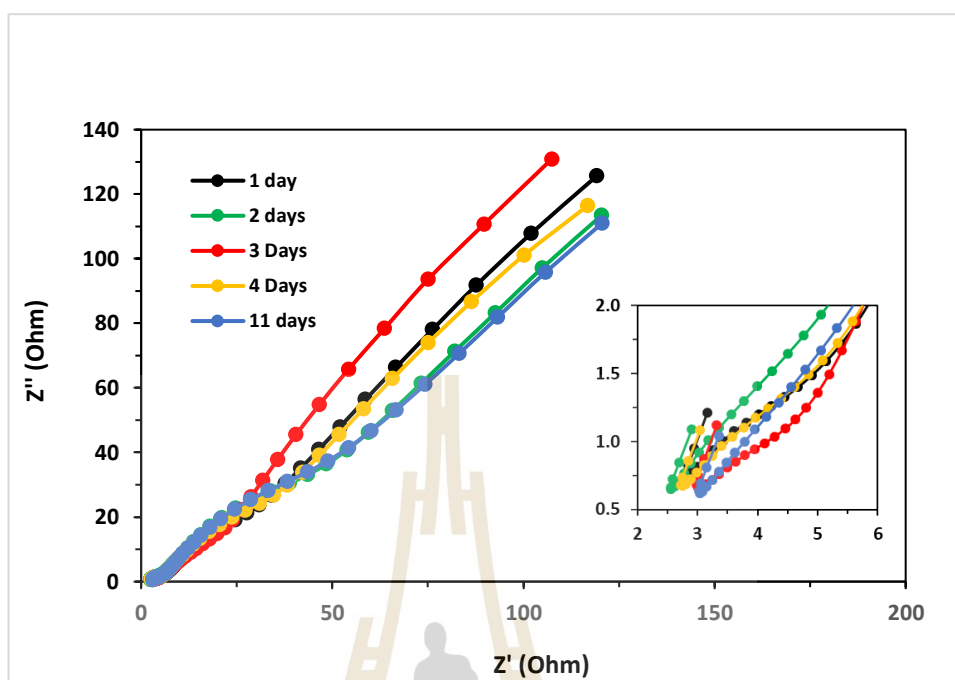


Figure 4.27 Nyquist plot of an 8 layers rGO 3D-printed electrode with varying electrolyte soaking times. The inset image shows this Nyquist at high frequency.

Table 4.14 The solution resistance (R_s) of 8 layers rGO 3D-printed electrode under the varying electrolyte soaking time.

	Soaking time (day)	R_s (Ω)
8 layers	1	2.82
	2	2.55
	3	2.99
	4	2.73
	11	3.02

4.5.2.4 Discussion

The experimental measurements of the areal capacitance for rGO 3D-printed electrodes, conducted under varying electrolyte soaking durations, revealed consistent CV and GCD measurements. Specifically, the areal capacitance value obtained from a 1 day soaking duration was 30.62 mF/cm², while that obtained from an 11-day soaking duration was 34.00 mF/cm², indicating a close resemblance

between the two. These results are also consistent with the EIS analysis, which showed similar characteristics in the Nyquist plot for the 2 and 11 days soaking times. Notably, the low-frequency range of the Warburg impedance, representing ion adsorption, overlapped with the CV and GCD results obtained earlier. It can be concluded that a 1-day soaking duration is sufficient for the 3D-printed electrode in the electrolyte. Additionally, the fact that the 3D-printed electrode can maintain stability for up to 11 days in the electrolyte demonstrates its durability.

4.5.2.5 Summary

The duration of electrolyte soaking for the 3D-printed electrode beyond 1 day does not affect the areal capacitance. However, to accurately measure the electrochemical properties of the 3D-printed electrode, it is recommended to soak it in the electrolyte for at least 1 day. This allows sufficient time for the electrolyte to penetrate and infiltrate the various layers of the 3D-printed electrode, ensuring optimal performance. This duration differs from the measurements conducted on conventional 2D electrodes, which are typically soaked for approximately 6 to 12 hours.

4.5.3 PANI deposition on rGO 3D-printed supercapacitor electrode

4.5.3.1 Maintain a consistent PANI deposition cycle and experiment with different electrode thicknesses.

4.5.3.1.1 Cyclic voltammetry measurement

Studies of the electrochemical properties of rGO/PANI 3D-printed electrodes using cyclic voltammetry and galvanostatic charge/discharge were conducted. The CV curves of rGO/PANI were examined within a potential range from -0.9V to 0.4V with a scan rate of 5 mV/s in 3M KOH electrolyte using a three-electrode system at room temperature. The sample with 2 PANI deposition cycles and varying electrode thicknesses is shown in Figure 4.28, and the areal capacitance is shown in Figure 4.29. In this experiment, the number of 3D printing layers varied from 4 to 24. The maximum layer number is limited by the ink filled in one syringe (10 ml size).

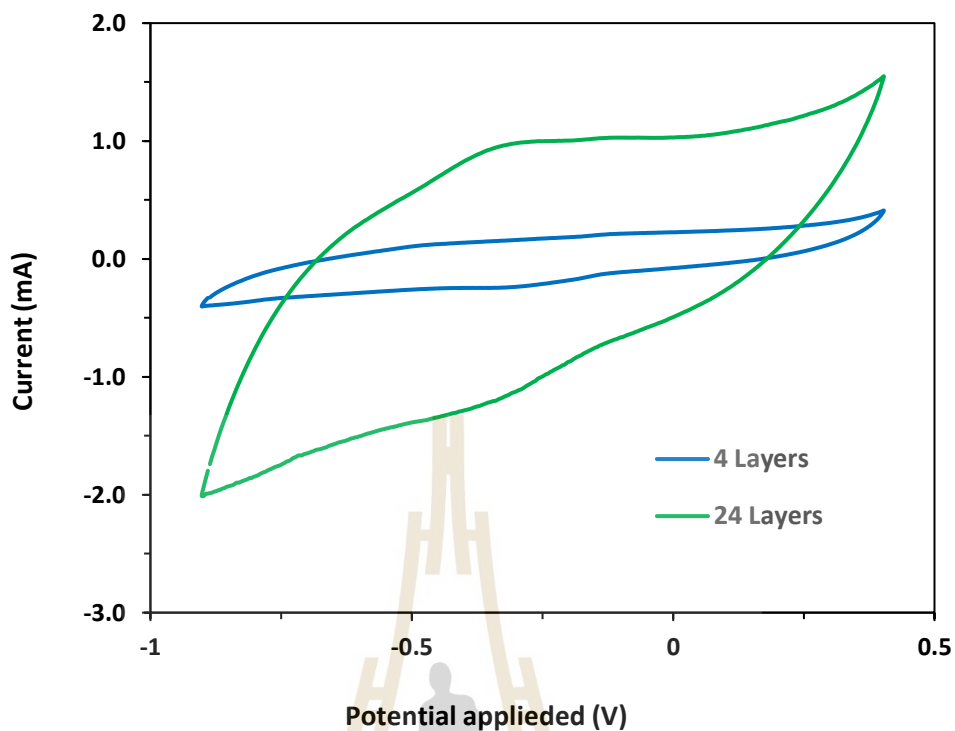


Figure 4.28 The comparison CV curve of rGO/PANI 3D-printed electrode of 4 layers and 24 layers 2 PANI deposition cycles with potential -0.9V to 0.4V, scan rate 5 mV/s.

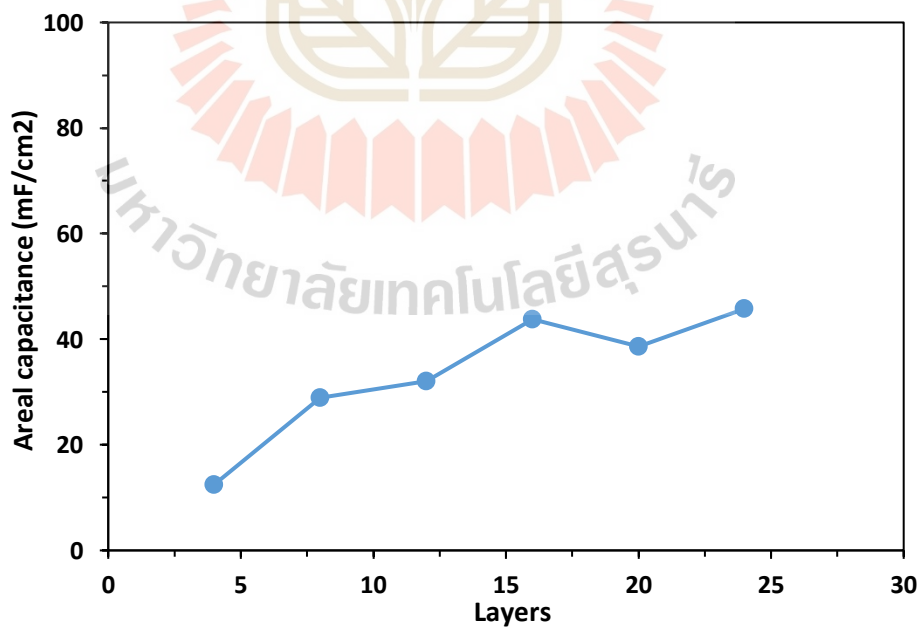


Figure 4.29 The comparison of CV curves for the areal capacitance of 2 PANI deposition cycles of rGO/PANI 3D-printed electrodes with varying the thickness.

4.5.3.1.2 Galvanostatic charge-discharge measurement

The galvanostatic charge-discharge behavior of 4, 8, 12, 16, 20, and 24 layers rGO/PANI 3D-printed electrodes with 2 PANI deposition cycles was measured at a current density of 1 mA/cm^2 . GCD curves are presented in Figure 4.30, and areal capacitance is shown in Figure 4.31.

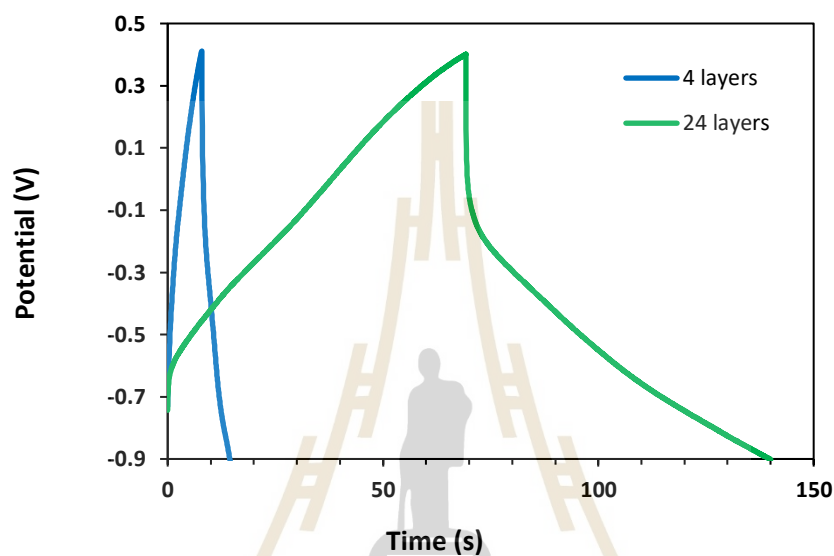


Figure 4.30 GCD curve of rGO/PANI 3D-printed electrode of 4 layers and 24 layers with 2 PANI deposition cycles were measured at a current density of 1 mA/cm^2 under potential -0.9V to 0.4V.

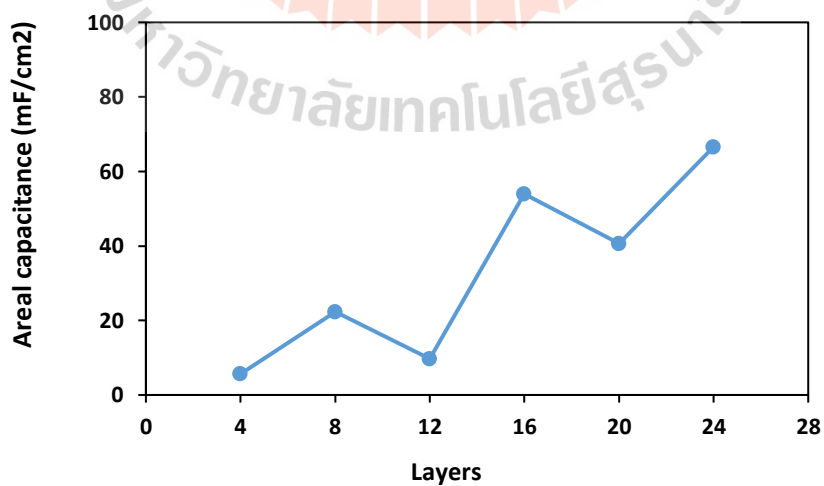


Figure 4.31 The comparison of GCD curves for the areal capacitance of 2 PANI deposition cycle of rGO/PANI 3D-printed electrodes with varying the thickness.

4.5.3.1.3 Electrochemical impedance spectroscopy (EIS) measurement

Electrochemical impedance spectroscopy (EIS) was used to study the behavior of 4, 8, 12, 16, 20, and 24 layers rGO/PANI 3D-printed electrodes with 2 PANI deposition cycles, as shown in Figure 4.32. The solution resistance (R_s), interpreted from the intercept at the Z' axis or the minimum value at high frequency, indicates that all samples have Z' values. Table 4.15 presents the solution resistance of the rGO/PANI 3D-printed electrodes with 8, 12, 16, 20, and 24 layers, which is about 2.60 ohms, except for the 4 layers sample.

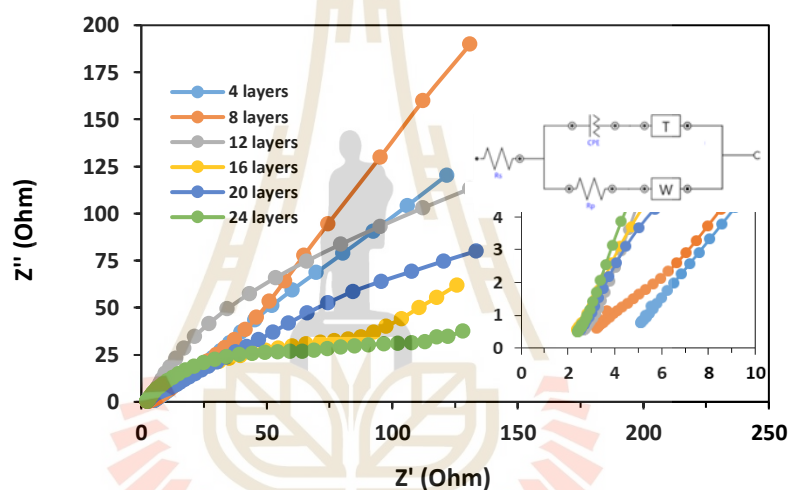


Figure 4.32 Nyquist plot of 8 layers rGO 3D-printed electrode which varying printed layer.

Table 4.15 The solution resistance (R_s) of 8 layers rGO 3D-printed electrode under the varying printed layer.

PANI deposition cycle	layer	R_s (Ω)	R_{CT} (Ω)
2	4	5.11	1.55
	8	3.22	1.28
	12	2.64	1.74
	16	2.38	10.3
	20	2.49	20.7
	24	2.39	86.2

All areal capacitance measurements from CV and GCD, maintaining a consistent PANI deposition cycle and experimenting with different electrode thicknesses, are presented in Figure 4.33 and Figure 4.34, respectively.

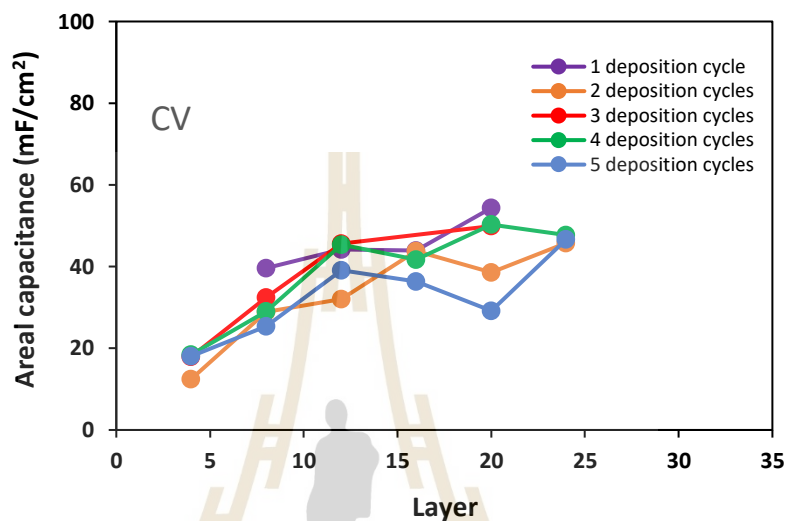


Figure 4.33 The comparison of CV curves for the areal capacitance of rGO/PANI 3D-printed electrodes with varying printed layer.

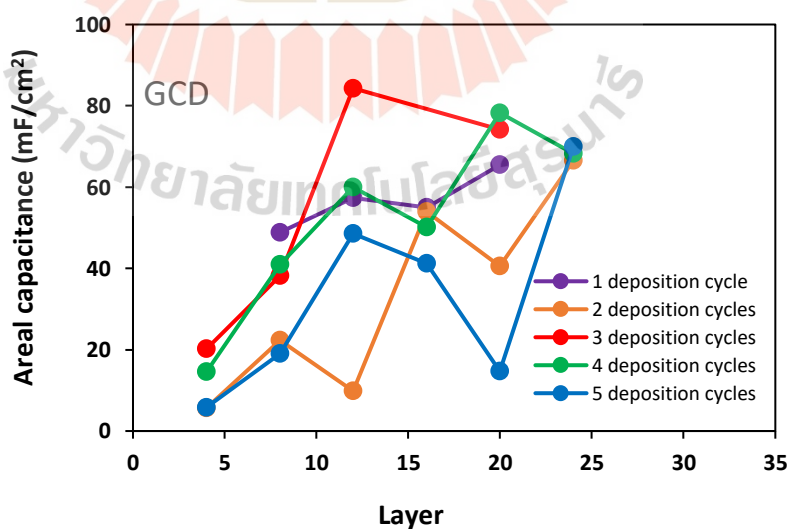


Figure 4.34 The comparison of GCD curves for the areal capacitance of rGO/PANI 3D-printed electrodes with varying printed layer.

4.5.3.1.4 Discussion

From the experimental measurements of CV and GCD to determine the areal capacitance of rGO/PANI 3D-printed electrodes under the specified PANI deposition cycle and varying thickness of the samples, it was found that the areal capacitance increased with the thickness of the 3D-printed electrode for every deposition cycle. The graph of the areal capacitance exhibited steep slopes at 4, 8, and 12 layers. Subsequently, the slope decreased at 16, 20, and 24 layers. This information can be compared with the graph obtained from the low-frequency region of the EIS measurements. The EIS graph showed a decreasing slope, with the lowest slope observed at 24 layers, as illustrated in Figure 4.32. Therefore, it can be observed that the resistance values are likely dependent on the thickness or number of layers of the electrodes and impact the areal capacitance.

4.5.3.1.5 Summary

When fixing the PANI deposition time and varying the thickness of the electrode by the number of layers from 4 to 24, it was observed that the areal capacitance increased with the electrode thickness. The highest capacitance values in this work were 54.33 mF/cm² for 20 layers and 1 PANI deposition cycle, as measured by CV, and 84.32 mF/cm² for 12 layers and 3 PANI deposition cycles, as measured by GCD.

4.5.3.2 Maintain a consistent electrode thickness and experiment with different PANI deposition cycle

4.5.3.2.1 Cyclic voltammetry measurement

Studies of the electrochemical properties of rGO/PANI 3D-printed electrodes using cyclic voltammetry and galvanostatic charge/discharge were conducted. The CV curves of rGO/PANI were examined within a potential range from -0.9V to 0.4V with a scan rate of 5 mV/s in 3M KOH electrolyte using a three-electrode system at room temperature. The sample with 8 layers and varying deposition cycles is shown in Figure 4.35, and the areal capacitance is shown in Figure

4.36. The PANI deposition cycle varied from 1 to 5 cycles because other work reported that deposition within 5 cycles shows a noticeable difference in the coated layer.

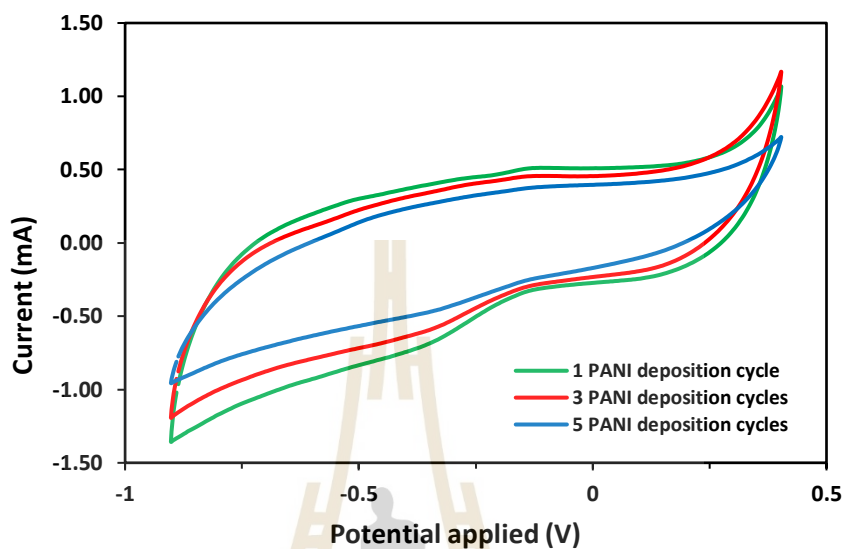


Figure 4.35 The comparison CV curve of an rGO/PANI 3D-printed electrode with 8 layers, 1, 3, and 5 PANI deposition cycles, potential -0.9V to 0.4V, and scan rate of 5 mV/s.

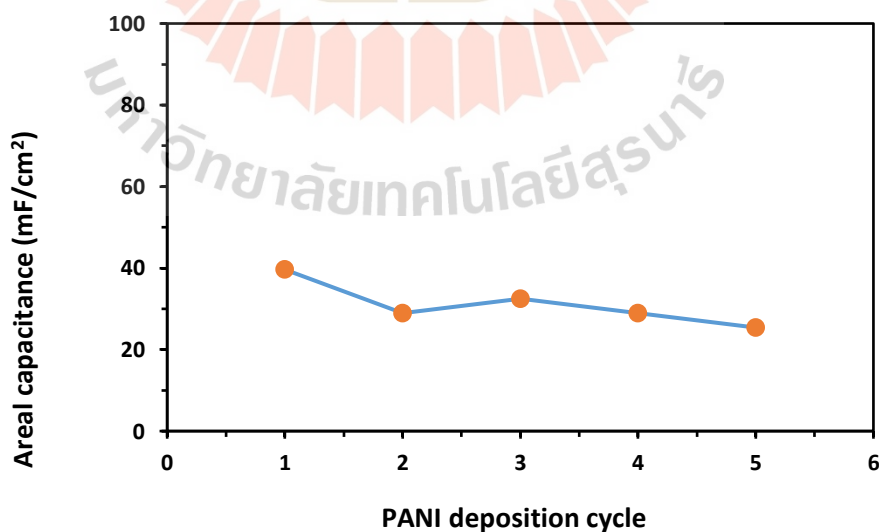


Figure 4.36 The comparison of CV curves for the areal capacitance of 8 layers rGO/PANI 3D-printed electrode with 1 to 5 PANI deposition cycles.

The CV curve in Figure 4.35 indicates that PANI deposition at 1 cycle offers the highest capacitance, which decreases as the deposition cycles increase to 3 and 5. This result correlates with the areal capacitance values shown in Figure 4.36, where an increase in PANI deposition cycles leads to a decrease in areal capacitance.

4.5.3.2.2 Galvanostatic charge-discharge measurement

The galvanostatic charge-discharge behavior of 8 layers rGO/PANI 3D-printed electrodes with various deposition cycles was measured at a current density of 1 mA/cm². GCD curves and areal capacitance are presented in Figure 4.37 and Figure 4.38.

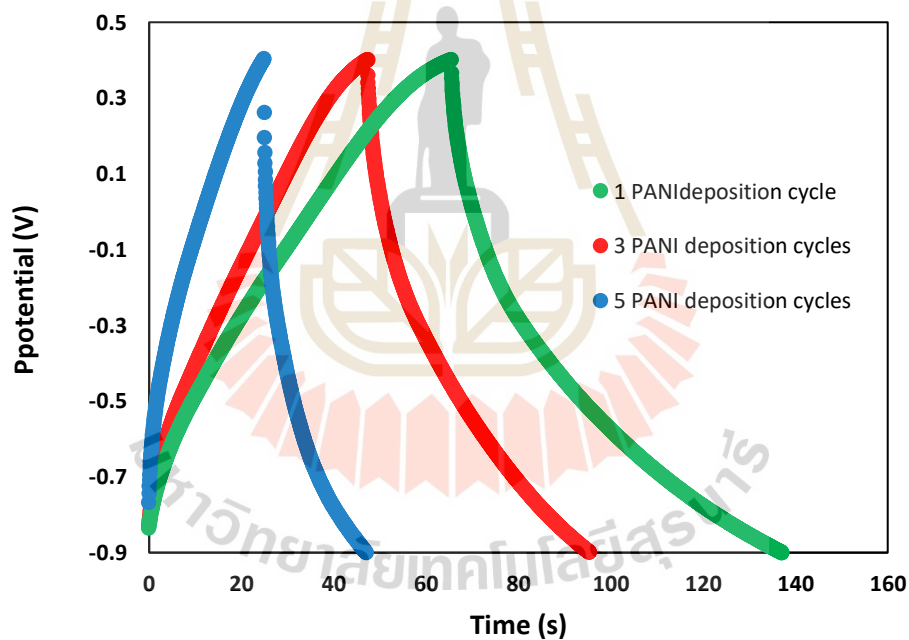


Figure 4.37 GCD curve of 8 layers rGO/PANI 3D-printed electrode with 1, 3, and 5 PANI deposition cycles was measured at a current density of 1 mA/cm² under potential -0.9V to 0.4V.

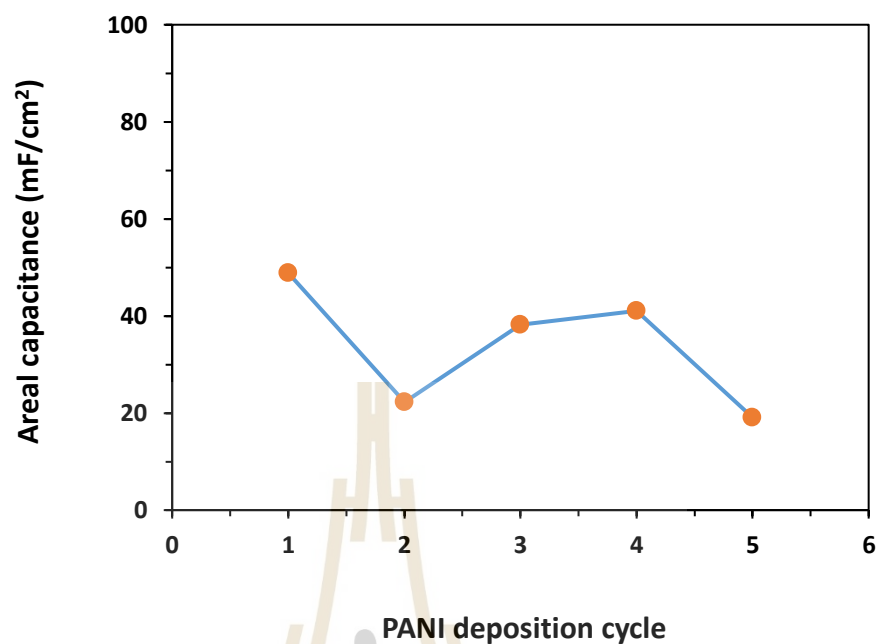


Figure 4.38 The comparison of GCD curves for the areal capacitance of 8 layers rGO/PANI 3D-printed electrode with 1, 2, 3, 4, and 5 PANI deposition cycles.

4.5.3.2.3 Electrochemical impedance spectroscopy (EIS) measurement

Electrochemical impedance spectroscopy (EIS) was used to study the behavior of 8 layers rGO/PANI 3D-printed electrodes with 1, 2, 3, 4, and 5 PANI deposition cycles, as shown in Figure 4.39. The solution resistance (R_s), interpreted from the intercept at the Z' axis or the minimum value at high frequency, indicates that all samples have Z' values. Table 4.16 presents the solution resistance of the 8 layers rGO/PANI 3D-printed electrodes with 1, 2, 3, 4, and 5 PANI deposition cycles, which is about 2.79 ± 0.25 ohms.

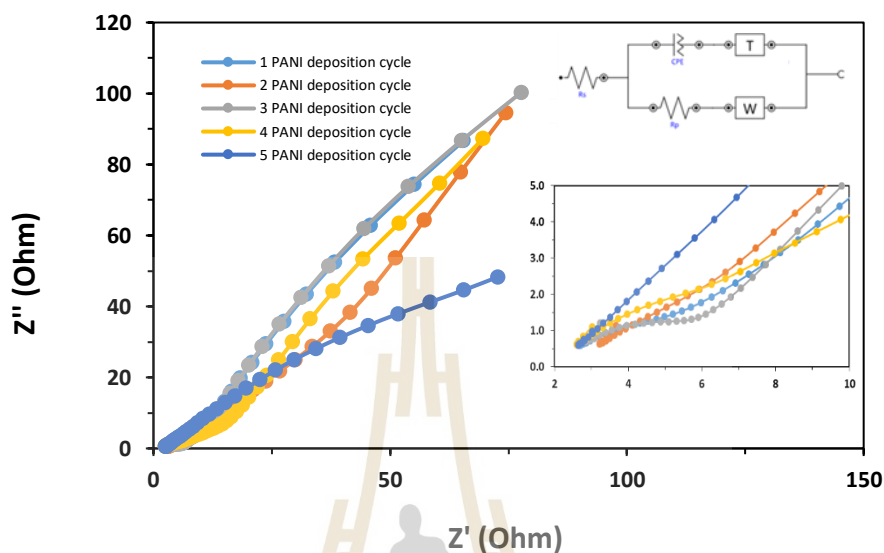


Figure 4.39 Nyquist plot of 8 layers rGO 3D-printed electrode with varying PANI deposition cycle.

Table 4.16 The solution resistance (R_s) of 8 layers rGO 3D-printed electrode under the varying PANI deposition cycle.

Printed layer	PANI deposition cycle	R_s (Ω)	R_{CT} (Ω)
8	1	2.66	7.59
	2	3.216	1.55
	3	2.84	6.42
	4	2.60	13.10
	5	2.64	28.10

All areal capacitance measurements from CV and GCD with a fixed PANI deposition cycle and varying electrode thickness are presented in Figure 4.40 and Figure 4.41, respectively. All areal capacitance data from CV and GCD are presented in Table 4.17 and Table 4.18, respectively.

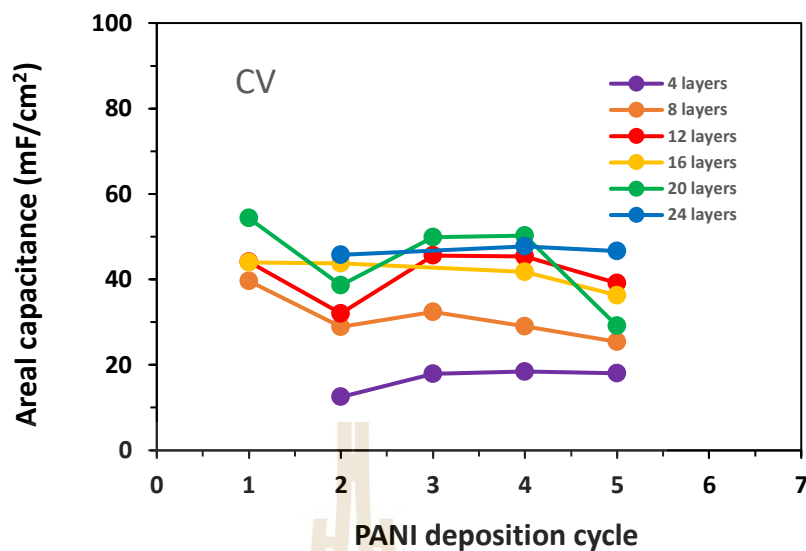


Figure 4.40 The comparison of CV curves for the areal capacitance of rGO/PANI 3D-printed electrodes. The 3D-printed electrode of 4 layers with deposition 1 cycle is not shown in the graph because this sample was cut and utilized for SEM cross-sectional analysis.

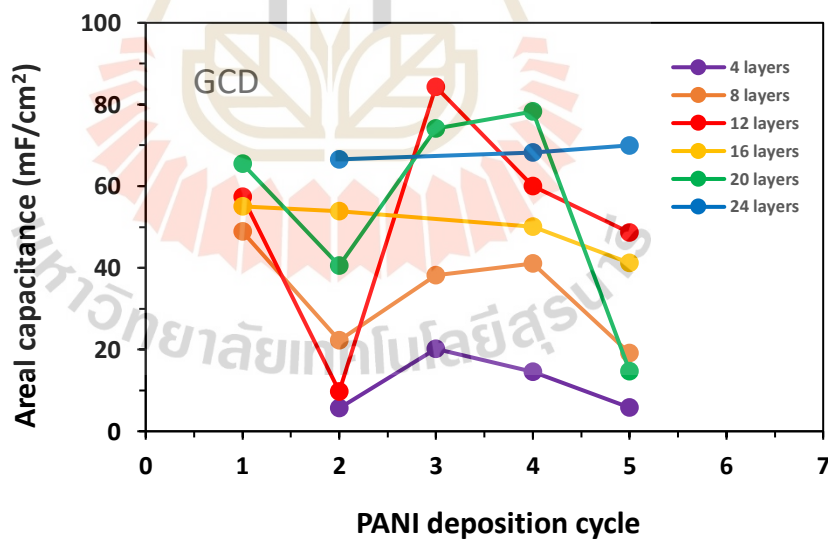


Figure 4.41 The comparison of GCD curves for the areal capacitance of rGO/PANI 3D-printed electrodes. The 3D-printed electrode of 4 layers with deposition 1 cycle and of 24 layers with deposition 1, 3 cycles are not shown in the graph because these samples were cut and utilized for SEM cross-sectional analysis.

Table 4.17 Areal capacitance from CV measurement at scan rate 10 mV/s, window potential: -0.9V to 0.4V, 3M KOH.

Printed layer	Areal capacitance of 1 PANI deposition (mF/cm ²)	Areal capacitance of 2 PANI deposition (mF/cm ²)	Areal capacitance of 3 PANI deposition (mF/cm ²)	Areal capacitance of 4 PANI deposition (mF/cm ²)	Areal capacitance of 5 PANI deposition (mF/cm ²)
4	*NA	12.49	17.95	18.46	18.06
8	39.64	28.92	32.42	28.99	25.40
12	44.16	32.06	45.58	15.38	39.15
16	43.98	43.82	**NA	41.74	36.30
20	54.33	38.62	49.91	50.27	29.12
24	*NA	45.76	*NA	47.72	46.65

*NA = Not available data because the electrode was cut and used for SEM cross section.

**NA = Not available data because the electrode is broken during experiment.

Table 4.18 Areal capacitance from GCD measurement at 1 mA/cm², window potential: -0.9V to 0.4V, 3M KOH.

Printed layer	Areal capacitance of 1 PANI deposition (mF/cm ²)	Areal capacitance of 2 PANI depositions (mF/cm ²)	Areal capacitance of 3 PANI depositions (mF/cm ²)	Areal capacitance of 4 PANI depositions (mF/cm ²)	Areal capacitance of 5 PANI depositions (mF/cm ²)
4	*NA	5.65	20.17	14.53	5.83
8	48.85	22.27	38.22	41.01	19.09
12	57.36	9.78	84.32	60.04	48.29
16	55.05	53.93	**NA	50.11	41.20
20	65.48	40.57	74.14	78.28	14.74
24	*NA	66.57	*NA	68.26	69.99

*NA = Not available data because the electrode was cut and used for SEM cross section.

**NA = Not available data because the electrode is broken during experiment.

4.5.3.2.4 Discussion

Based on the experimental results of increasing the number of PANI coatings on the 3D-printed substrate, it was observed that the areal capacitance decreased with an increasing number of coating cycles. This outcome contradicts the initial hypothesis and the reviewed data, which anticipated increased areal capacitance. Despite the apparent increase in the nanofiber network observed in the cross-sectional SEM image, confirming the trend observed with the number of coating cycles, this increase in the nanofiber network had a detrimental effect on the areal capacitance. We can compare this direct impact to the effect of EIS shown in Figure 4.38 and previous observations. Notably, the thicker electrode with 24 layers exhibits a distinct low-frequency or Warburg impedance region. Moreover, the RCT increased with thickness and a high number of deposition cycles. This indicates that the electrode with 24 layers exhibits the highest resistance, potentially contributing to the reduction in areal capacitance as observed in the cyclic voltammetry (CV) due to its influence on the shape of CV curves and the IR drop curve of galvanostatic charge-discharge (GCD).

When considering the causes of the resistance increase with an increasing number of PANI coating cycles, it can be attributed to the uneven adhesion of PANI in the first coating layer, which leads to the formation of gaps in specific areas. This phenomenon is visually supported by the SEM image depicted in Figure 4.42. Gaps can be observed in the first coating layer of PANI of all thicknesses within the 3D-printed structure. The presence of these gaps can be attributed to the inclusion of water in the PANI colloidal solution. However, during the drying process, the water completely evaporates, resulting in the formation of these gaps.

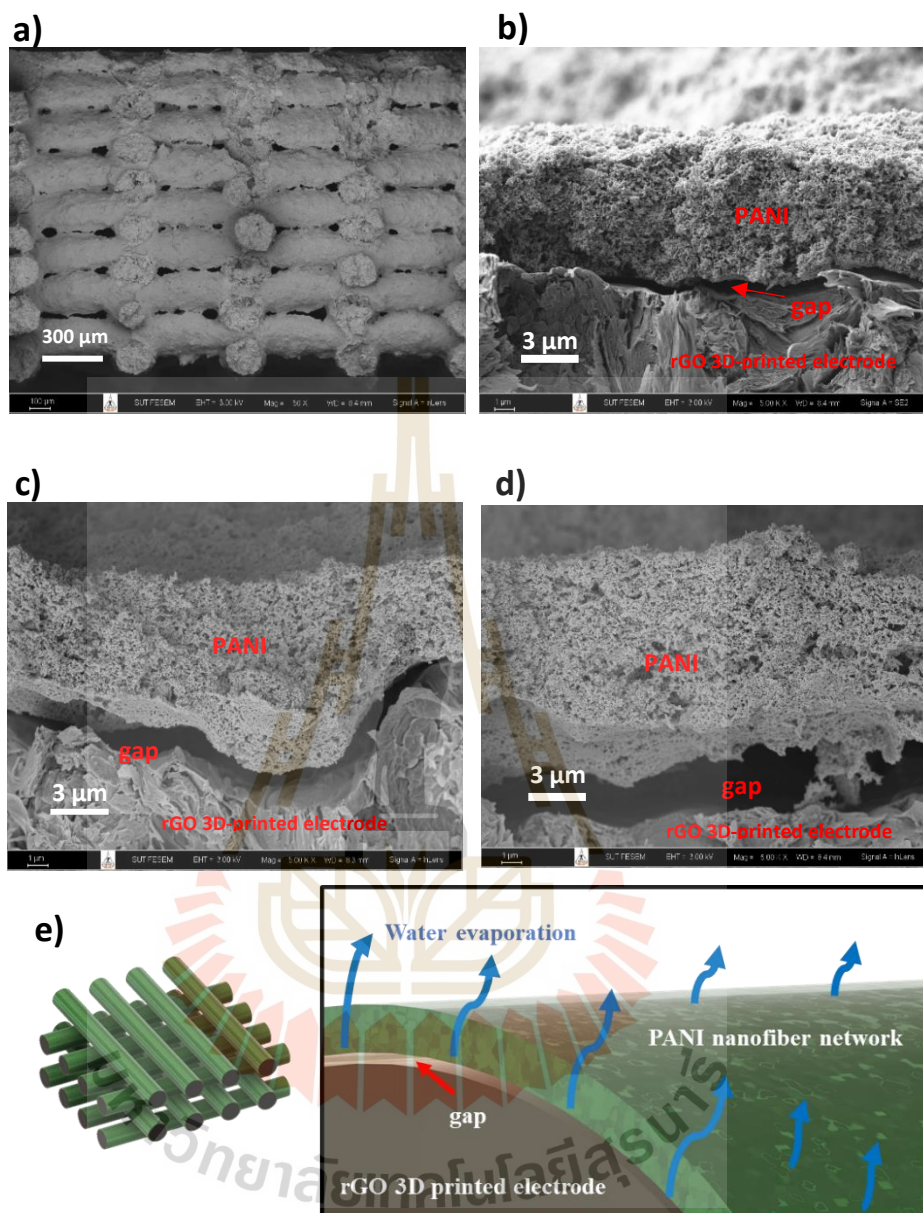


Figure 4.42 SEM of rGO/PANI 3D-printed electrode which the synthesis PANI is a colloid solution in water a) cross section SEM of 16 layers rGO 3D-printed electrode with magnification of 30X b), c), and d) is cross section SEM image at differences area of 16 layers rGO 3D-printed electrode with magnification of 5000X. e) The illustration of water evaporation from rGO 3D-printed electrode.

The hypothesis suggesting that water evaporation leads to gap formation is supported by the evidence presented in Figure 4.43, where NMP (N-Methyl-2-pyrrolidone) is used instead of water. In this case, the gaps that typically occur in the initial PANI coating layer disappear. It is evident from the figure that PANI and the surface of the rGO 3D-printed electrode exhibit closer adhesion to each other.

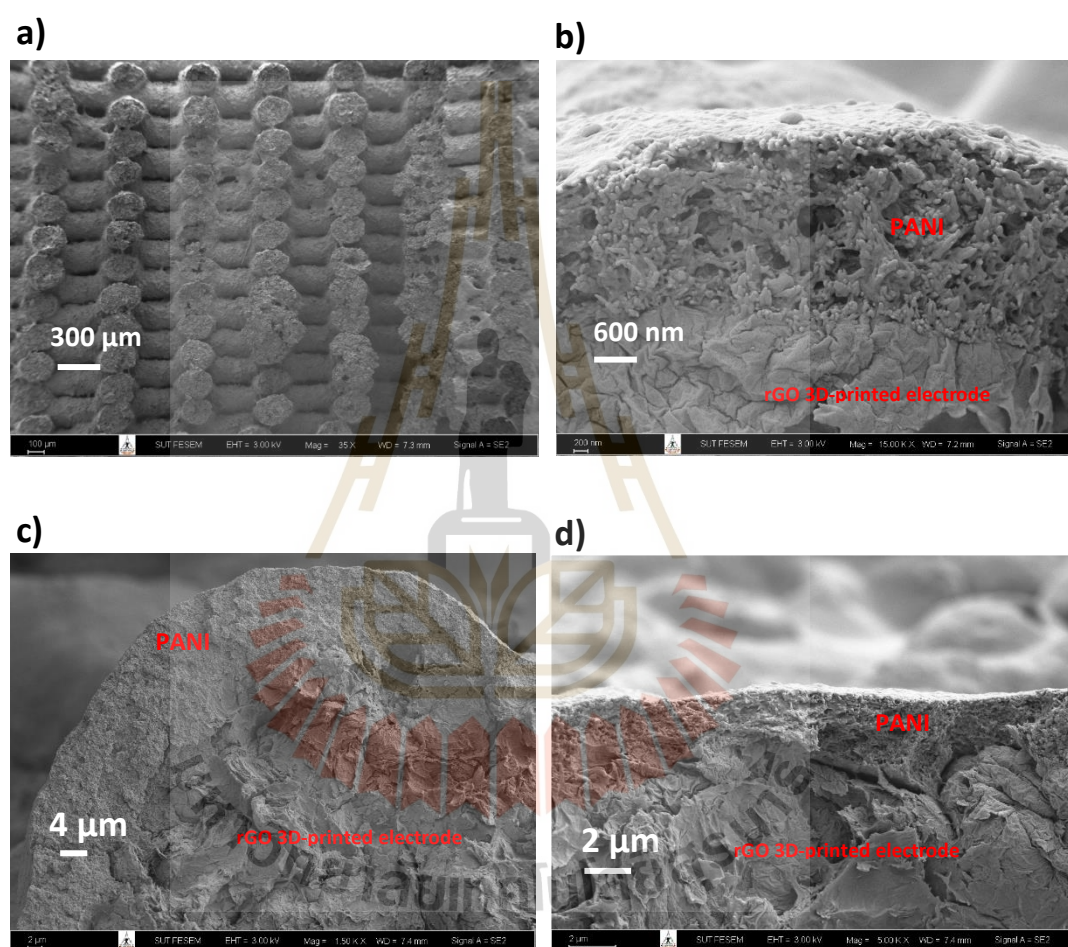


Figure 4.43 SEM of rGO/PANI 3D-printed electrode which the synthesis PANI is a colloid solution in NMP a) cross section SEM of 24 layers rGO 3D-printed electrode with magnification of 35X b), c), and d) is cross section SEM image at differences area of 16 layers rGO 3D-printed electrode with magnification of 15000X, 1500X, and 5000X, respectively.

From the experiments, the highest recorded value for areal capacitance was 84.32 mF/cm². This value was obtained from a dataset consisting of 12 layers of rGO/PANI 3D-printed electrodes, which were coated with PANI for 3 cycles. The areal energy density (EA) is 19.79 μWh/cm² and the power density (PA) is 672.81 μW/cm², which are calculated using the following equation:

$$E_A = \frac{1000}{2 \times 3600} C_A U^2$$

$$P_A = \frac{3600 \times E_A}{t}$$

Where C_A is the areal capacitance (F/cm²), U is the working voltage (V), and t is the discharge time (s) measured in the GCD.

4.5.3.2.5 Summary

In this experiment, it was observed that the areal capacitance decreased as the amount of PANI coating on the rGO 3D-printed electrode increased, indicating an increase in resistance, as discussed earlier. The highest value of areal capacitance was 84.32 mF/cm², accompanied by corresponding values of areal energy density (EA) of 19.79 μWh/cm² and power density (PA) of 672.81 μW/cm². These measurements were obtained from the 12 layers of rGO/PANI 3D-printed electrodes that underwent PANI coating for 3 cycles. In Section 4.5.1, the rGO 3D-printed electrode with a thickness of 20 layers demonstrated an areal capacitance of 145.52 mF/cm². The corresponding areal energy and power densities calculated were 34.16 μWh/cm² and 130.44 μW/cm², respectively. These calculated energy density and power density values are within the intermediate range compared to other studies. However, the power density value is relatively low.

CHAPTER V

CONCLUSION

The development of a three-dimensional printing system for energy storage aims to explore new methods of preparing novel electrodes for advanced research that go beyond traditional electrode preparation methods, fostering new ideas and innovative concepts.

Step 1: Develop a 3D printer for the fabrication of supercapacitor electrodes

The most suitable technique for this work is direct ink writing (DIW) using a pneumatic dispensing extruder, which has been specifically developed for this research. This 3D printing system effectively addresses the limitations of working with small quantities of materials in the laboratory, enhancing research capabilities. It offers the advantages of convenience and compatibility with various materials, such as powders and gels, including activated carbon, carbon black, and rGO powders, which were used in this study.

Step 2: Study and prepare high-viscosity ink for 3D-printed electrodes

Preparing ink that is compatible with three-dimensional printing is crucial for shaping the electrodes. In this case, successful ink preparation involves a specific powder material ratio of rGO to cellulose acetate (1:19) with a 5 wt% concentration of rGO. For ink preparation using a 10 ml syringe, the required amounts are 0.2g of rGO, 3.8g of cellulose acetate, and 16g (20 ml with a density of 0.791 g/mL at 25°C) of acetone as the solvent. This optimized ink preparation eliminates the need for freeze-drying the printed pieces, which is a significant advantage. Furthermore, this ink preparation method is applicable to different 3D printing setups, including printing on various substrates, as depicted in Figure 5.1.

Step 3: Investigate the printing parameters of 3D-printed supercapacitor electrodes

Determining the printing parameters is crucial for achieving high-quality prints. The optimal values can be found in Table 4.4 from the previous section, including printing speed, flow pressure, and nozzle diameter. Additionally, compensatory adjustments are necessary due to the approximately 25% model shrinkage after printing to ensure precise accuracy.

Step 4: Synthesize and coat PANI on 3D-printed supercapacitor electrodes

The successful synthesis of PANI using the chemical oxidative polymerization (COP) method and the resulting nanofiber network structure (with a diameter of 46.66 ± 5.50 nm) make it suitable for coating on rGO 3D-printed electrodes to study electrochemical properties. In addition, the XRD result confirmed the PANI broad peak corresponding to plane 200.

Step 5: Study the electrochemical properties of 3D-printed supercapacitor electrodes

Studying the electrochemical properties of 3D-printed supercapacitor electrodes confirms the hypothesis that these electrodes can enhance supercapacitor performance. The thickness of the rGO 3D-printed electrode significantly affects the areal capacitance due to the increased surface area. However, when PANI is coated on the rGO 3D-printed electrode, the areal capacitance decreases, and this reduction continues with each additional coating cycle. This phenomenon is likely due to the formation of gaps between the electrode surface and the PANI in the initial layer, which affects the resistance and efficiency of the electrode. The highest value of areal capacitance was 84.32 mF/cm^2 , accompanied by corresponding values of areal energy density (EA) of $19.79 \text{ } \mu\text{Wh/cm}^2$ and power density (PA) of $672.81 \text{ } \mu\text{W/cm}^2$, as presented with other works in Figure 5.2. The Ragone plot shows that the energy density value falls within the moderate range compared to other studies. However, the power density value is relatively low. This is likely attributed to factors associated with the formation of gaps between the electrode surface and the PANI nanofiber network.

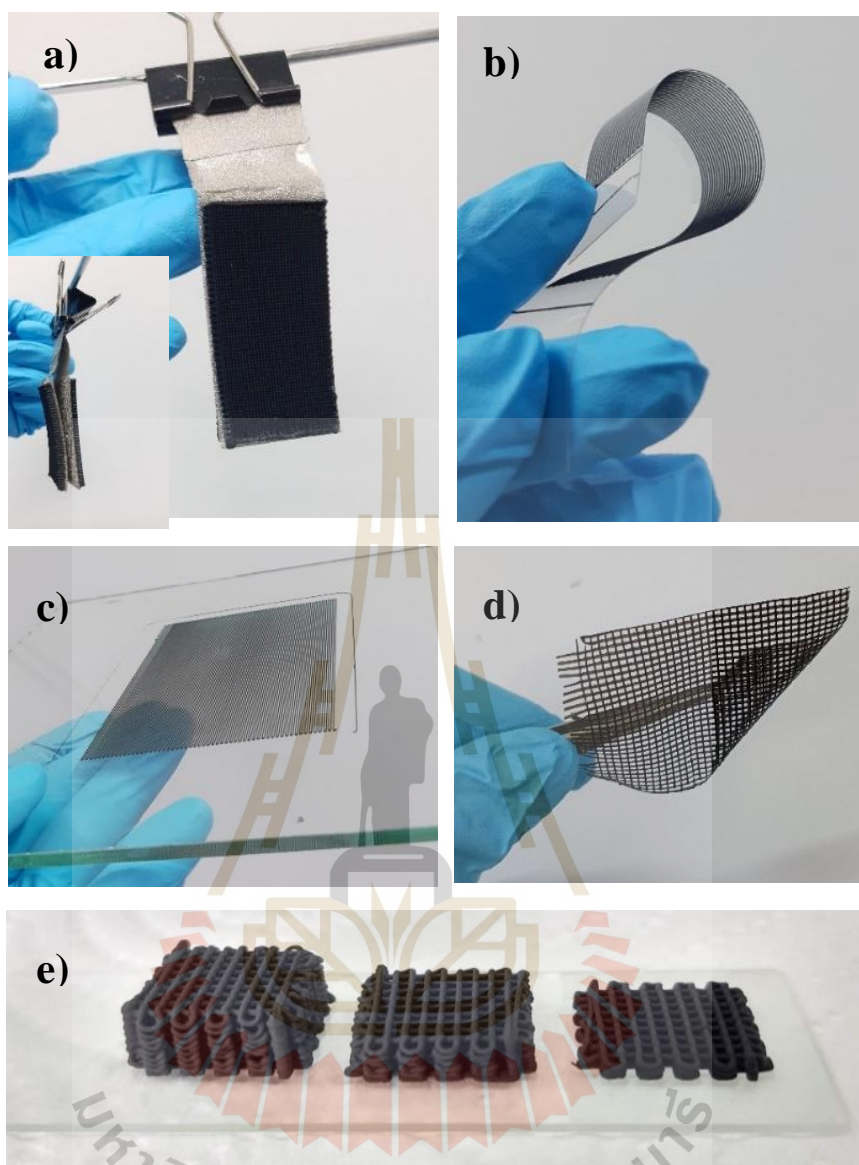


Figure 5.1 Example of ink print testing on the various substrates a) nickel foam, b) plastic sheet, c) glass, d) stand-alone sample, and e) glass slide.

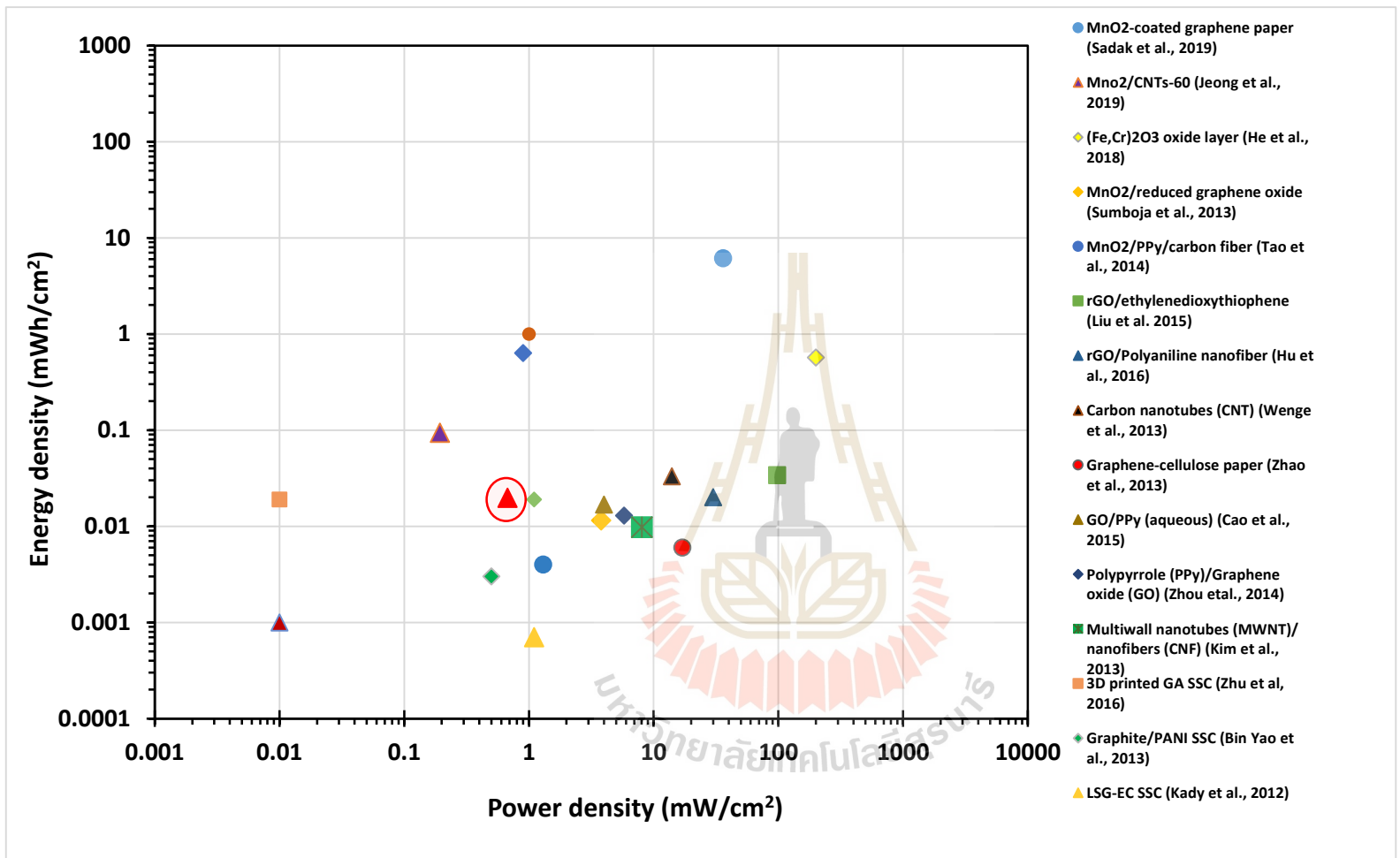


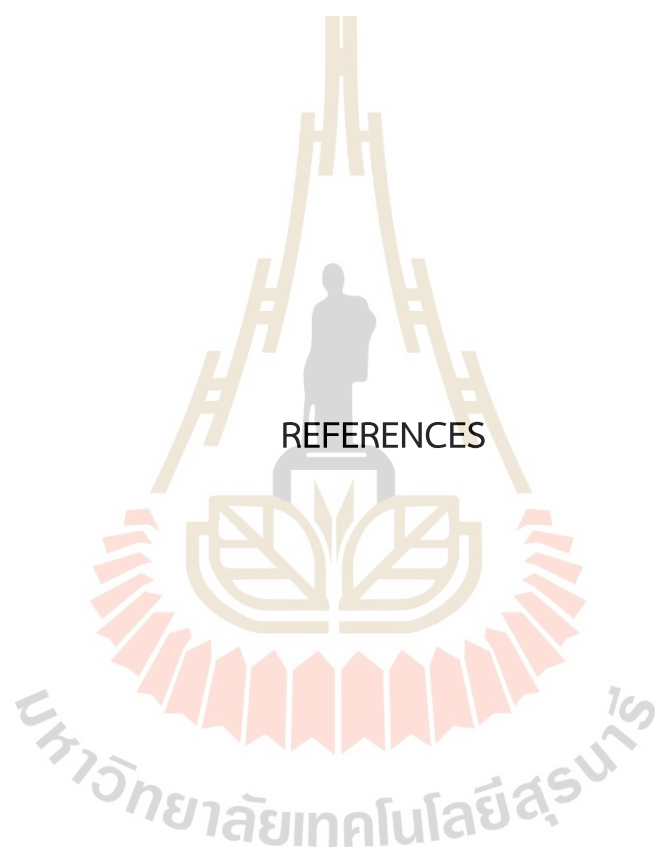
Figure 5.2 Ragone plot, comparing the areal power density versus the areal energy density in this study with other works in supercapacitor research field.

Future work

In future work, the focus will be on studying the method of coating PANI on the rGO 3D-printed electrode to minimize the gaps between the electrode surface and the PANI layer. This approach, newly discovered in this study, aims to reduce resistance and enhance the efficiency of the electrode. By investigating this coating technique, the goal is to optimize electrode performance and improve the overall performance of the supercapacitor.

Possibility/applications

This research work has provided insights into the factors influencing the trend of areal capacitance and has discovered a new concept that can potentially reduce the gap between the surface of the electrode and the PANI coating in the first layer. It is hoped that this method will improve the electrode's efficiency. Furthermore, in terms of device development, it can be extended to various future applications such as flow batteries, 3D electrode printing, 3D bio-printing, and ceramic 3D printing. These advancements are expected to stimulate the emergence of new and interesting research opportunities.



REFERENCES

REFERENCES

- Abdulwahhab, H., Leqaa, A., Omar, G., Shankar, Sehgal., Mustafa, A., Kuldeep, K., Safaa, A., Israa, K., Mustafa, M. and Ummal, A. (2022). A Review on Polyaniline: Synthesis, Properties, Nanocomposites, and Electrochemical Applications. *International Journal of Polymer Science*. 20(22).
- Achilleos, Demetra S. and Hatton, T. (2015). Surface design and engineering of hierarchical hybrid nanostructures for asymmetric supercapacitors with improved electrochemical performance. *Journal of Colloid and Interface Science*. 447, 282–301.
- Altin, S., Bulut, F. and Yasar, S. (2019). The production of a low cost printing device for energy storage systems and the application for supercapacitors. *Journal of Energy Storage*. 25(8), 100882.
- Abdelhamid, M. E., O'Mullane, A. P. and Snook, G. A. (2015). Storing energy in plastics: a review on conducting polymers & their role in electrochemical energy storage. *Royal Society of Chemistry Advances*. 5(15), 11611–11626.
- Babel, V. and Hiran, B. (2021). A review on polyaniline composites: synthesis, characterization, and applications. *Polymer Composites*. 42(7), 3142–3157.
- Balli, B., Şavk, Aysun. and Sen, F. (2019). Graphene and polymer composites for supercapacitor applications. *Nanocarbon and its Composites*. 1, 123–151.
- Bian, L., Luan, F., Liu, S. and Liu, X. (2012). Self-doped polyaniline on functionalized carbon cloth as electroactive materials for supercapacitor. *Electrochimica Acta*. 64, 17–22.
- Bavio, M. A., Acosta, G. and Kessler, T. (2014). Polyaniline and polyaniline-carbon black nanostructures as electrochemical capacitor electrode materials. *International Journal of Hydrogen Energy*. 39(16), 8582–8589
- Bin, Y., Swetha, C., Jing, Z., Wang, X., Fang, Q., Cheng, Z., Eric, B. D., Christopher, M. S., Marcus, A. W. and Yat, L. (2019). Efficient 3D Printed Pseudocapacitive Electrodes with Ultrahigh MnO₂ Loading. *Joule*. 3(2), 459-470.

- Cai, D., Huang, H., Wang, D., Liu, B., Wang, L., Liu, Y., Li, Q. and Wang, T. (2014). High-Performance Supercapacitor Electrode Based on the Unique ZnO@Co₃O₄ Core/Shell Heterostructures on Nickel Foam. *ACS Applied Materials and Interfaces*. 6(18), 15905–15912.
- Chen, W., Rakhi, R. B., Wang, Q., Hedhili, M. N. and Alshareef, H. N. (2014). Morphological and Electrochemical Cycling Effects in MnO₂ Nanostructures by 3D Electron Tomography. *Advanced Functional Materials*. 24(21), 3130-3143.
- Cheng, Z., Tianyu, L., Fang, Q., Yong-Jin, T. H., Eric, B. D., Joshua, D. K., Christopher, M. S., Marcus A. W. and Yat L. (2016). Supercapacitors Based on Three-Dimensional Hierarchical Graphene Aerogels with Periodic Macropores. *Nano Letters*. 16(6), 3448-3456.
- Choudhary, Ni., Li, C., Moore, J., Nagaiah, N., Zhai, L., Jung, Y., Thomas, J. (2017). Asymmetric Supercapacitor Electrodes and Devices. *Advanced Materials*, 1605336.
- Derakhshanfar, S., Mbeleck, R., Xu, K., Zhang, X., Zhong, W. and Xing, M. (2018). 3D bioprinting for biomedical devices and tissue engineering: A review of recent trends and advances. *Bioactive Materials*. 3(2), 144–156.
- Diggikar, Rahul S., Deshmukh, Shamkumar P., Thopate, Tukaram S. and Kshirsagar, Santosh R. (2019). Performance of Polyaniline Nanofibers (PANI NFs) as PANI NFs-Silver (Ag) Nanocomposites (NCs) for Energy Storage and Antibacterial Applications. *ACS Omega*. 4(3), 5741-5749.
- Dhawale, D., Vinu, A. and Lokhande, C. (2011). Table nanostructured polyaniline electrode for supercapacitor application. *Electrochimica Acta*. 56(25), 9482-9487.
- Dong, X. C., Xu, H., Wang, X. W., Huang, Y. X., Chan-Park, M. B., Zhang, H., Wang, L. H., Huang, W. and Chen, P. (2012). 3D Graphene–Cobalt Oxide Electrode for High-Performance Supercapacitor and Enzymeless Glucose Detection. *ACS Nano*. 6(4), 3206–3213.

- Du, F.-P., Wang, J.-J., Tang, C.-Y., Tsui, C.-P., Xie, X.-L. and Yung, K.-F. (2013). Enhanced electrochemical capacitance of polyaniline/graphene hybrid nanosheets with graphene as templates. *Composites Part B: Engineering*. 53, 376–381.
- Gupta, V. and Miura, N. (2005). Electrochemically deposited polyaniline Nanowire's network. *Electrochemical and Solid-State Letters*. 8(12), A630.
- Gladis, A. S., Khanin, N., Paiboon, S. and Jedsada M. (2020). Fabrication of Activated Carbon Pouch Cell Supercapacitor: Effects of Calendering and Selection of Separator-Solvent Combination. *Current Applied Science and Technology*. 20(1).
- Hanlu, L., Jixiao, W., Qingxian, C., Zhi, W., Fengbao, Z. and Shichang, W. (2009). Theoretical and experimental specific capacitance of polyaniline in sulfuric acid. *Journal of Power Sources*. 190(2), 578-586.
- He, Y., Chen, W., Li, X., Zhang, Z., Fu, J., Zhao, C. and Xie, E. (2012). Freestanding Three-Dimensional Graphene/MnO₂ Composite Networks As Ultralight and Flexible Supercapacitor Electrodes. *ACS Nano*. 7(1), 174–182.
- He, Y., Chen, W., Zhou, J., Li, X., Tang, P., Zhang, Z., Fu, J. and Xie, E. (2014). Constructed Uninterrupted Charge-Transfer Pathways in Three Dimensional Micro/Nano interconnected Carbon-Based Electrodes for High Energy-Density Ultralight Flexible Supercapacitors. *ACS Applied Materials and Interfaces*. 6, 210-218.
- Jin, Y., Li, H., He, Y. and Fu, J. (2015). Quantitative analysis of surface profile in fused deposition modeling. *Additive Manufacturing*. 8, 142–148.
- Jixiao, W., Junsheng, W., Xiaoyan, Z. and Zhi, W. (2007). Assembly of Polyaniline Nanostructures. *Macromolecular Rapid Communications*. 28, 84–87.
- Kim, H., Matteini, P. and Hwang, B. (2022). Mini Review of Reliable Fabrication of Electrode under Stretching for Supercapacitor Application. *Micromachines*. 13, 1470.
- Kong, D.-S., Wang, J.-M., Shao, H.-B., Zhang, J.-Q. and Cao, C.-n. (2011). Electrochemical Fabrication of a Porous Nanostructured Nickel Hydroxide Film Electrode with Superior Pseudocapacitive Performance. *Journal of Alloys and Compounds*. 509(18), 5611-5616.

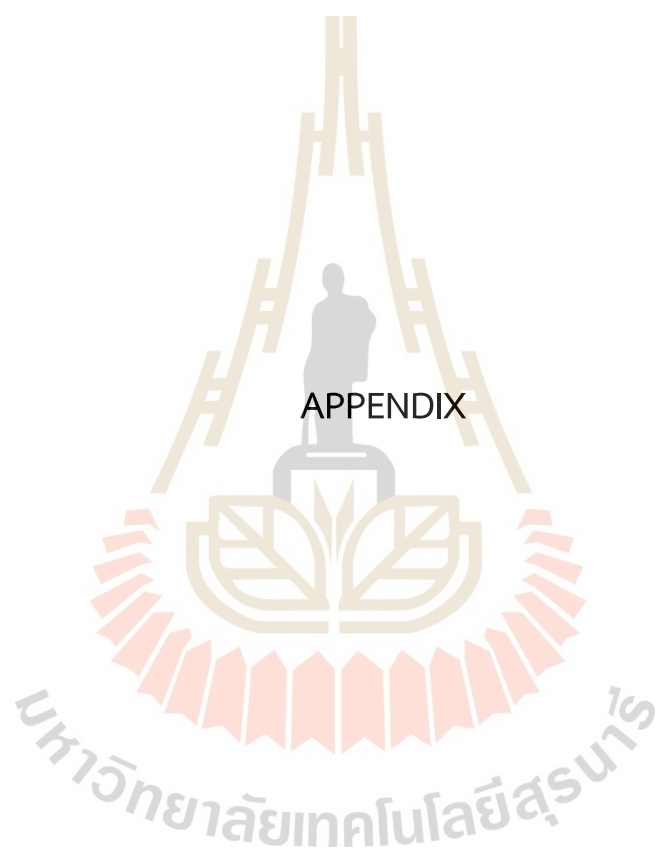
- Liu, J., Jiang, J., Bosman, M. and Fan, H. J. (2012). Three-dimensional tubular arrays of MnO_2 -NiO nanoflakes with high areal pseudocapacitance. *Journal of Materials Chemistry*. 22, 2419-2426.
- Liu, J., Jiang, J., Cheng, C., Li, H., Zhang, J., Gong, H. and Fan, H. J. (2011). Co_3O_4 Nanowire@ MnO_2 ultrathin nanosheet core/shell arrays: a new class of high-performance pseudocapacitive materials. *Advanced Materials*. 23(18), 2076-2081.
- Liu, Y., Cao, X., Jiang, D., Jia, D. and Liu, J. (2018). Hierarchical CuO nanorod arrays in situ generated on three-dimensional copper foam via cyclic voltammetry oxidation for high-performance supercapacitors. *Journal of Materials Chemistry A*. 6(22), 10474–10483.
- Lin, T.-W., Dai, C. S. and Hung, K. C. (2014). High Energy Density Asymmetric Supercapacitor Based on NiOOH/ Ni_3S_2 /3D Graphene and Fe_3O_4 / Graphene Composite Electrodes. *Scientific Reports*. 4(1), 7274.
- Lu, W., Hongmei, J., Shasha, W., Lijuan, K., Xuefan, J. and Gang, Y. (2013). Preparation of Fe_3O_4 with high specific surface area and improved capacitance as a supercapacitor. *Nanoscale*. 5(9), 3793-3799.
- Lu, X., Zhao, T., Ji, X., Hu, J., Li, T., Lin, X. and Huang, W. (2018). 3D printing well organized porous iron-nickel/polyaniline nanocages multiscale supercapacitor. *Journal of Alloys and Compounds*. 760, 78–83.
- Mahdavi, H. and Shahalizade, T. (2018). Investigation of the pseudocapacitive properties of polyaniline nanostructures obtained from scalable chemical oxidative synthesis routes. *Ionics*. 25(3), 1331–1340.
- Majumdar, D., Maiyalagan, T. and Jiang, Z. (2019). Recent Progress in Ruthenium Oxide-Based Composites for Supercapacitor Applications, *ChemElectroChem*. 6(17), 4343–4372.
- Manjunatha, C., Shwetha, K. P., Athreya, Y., Kumar, S. G. and Sudha, K. (2023). Perspective Supercapacitor-Powered Flexible Wearable Strain Sensors. *ECS Sensors Plus*. 2(1), 1

- Meher, S. K. and Rao, G. R. (2011). Ultralayered Co_3O_4 for High-Performance Supercapacitor Applications. *The Journal of Physical Chemistry C*. 115(31), 15646–15654.
- Niveditha, C. V., Aswini, R., Jabeen Fatima, M. J., Ramanarayan, R., Pullanjiyot, N. and Swaminathan, S. (2018). Feather like highly active Co_3O_4 electrode for supercapacitor application: A potentiodynamic approach. *Materials Research Express*. 5(6), 065501.
- Padmanathan, N. and Selladurai, S. (2013). Mesoporous MnCo_2O_4 spinel oxide nanostructure synthesized by solvothermal technique for supercapacitor. *Ionics*. 20(4), 479–487.
- Pal, B., Yang, S., Ramesh, S., Thangadurai, V. and Jose, R. (2019). Electrolyte selection for supercapacitive devices: A critical review. *Nanoscale Advances*. 1, 3087-3809.
- Palash Chandra Maity, Mudrika Khandelwal. (2016). Synthesis Time and Temperature Effect on Polyaniline Morphology and Conductivity. *American Journal of Materials Synthesis and Processing*. 1(4), 37-42.
- Park, Hyun-Woo., Kim., Taejoon., Huh., Jinyoung., Kang., Minjeong., Lee., Ji., Yoon and Hyeonseok. (2012). Anisotropic Growth Control of Polyaniline Nanostructures and Their Morphology-Dependent Electrochemical Characteristics. *ACS nano*. 6, 7624-33.
- Peng, H., Yao, B., Wei, X., Liu, T., Kou, T., Xiao, P., Zhang, Y. and Li, Y. (2019). Pore and Heteroatom Engineered Carbon Foams for Supercapacitors. *Advanced Energy Materials*. 9(19), 36-65.
- Rafiee, M., Farahani, R. D. and Therriault, D. (2020). Multi-Material 3D and 4D Printing: A Survey. *Advanced Science*. 7(12), 1-26.
- Sahoo, B. B., Kumar, N., Panda, H. S., Panigrahy, B., Sahoo, N. K., Soam, A. and Sahoo, P. K. (2021). Self-assembled 3D graphene-based aerogel with Au nanoparticles as high-performance supercapacitor electrode. *Journal of Energy Storage*. 43, 103-157.

- Santi, R. and Piyapong, A. (2019). Effect of Polyaniline content on the capacitance of Polyaniline/Carbon powder composite. *Journal of Physics: Conference Series*. 1380, 012140.
- Shacklette, L. and Han, C. (1993). Solubility and dispersion characteristics of polyaniline. *MRS Online Proceedings Library*. 328.
- Shuhua, Y., Yuanyue, L., Yufeng, H., Xiaopeng, Y., William, A. G III., Xiao, L. Z. and Bingqiang, C. (2018). Oxygen-Vacancy Abundant Ultrafine Co₃O₄/Graphene Composites for High-Rate Supercapacitor Electrodes. *Advanced science news*. 5, 1700659.
- Shaker, A. E., Mohamed, E. H., Moataz, M. S. and Mazhar B. T. (2015). Preparation and characterization of a pseudocapacitor electrode by spraying a conducting polymer onto a flexible substrate. *Journal of Taibah University for Science*. 10(2), 281-285.
- Shangwen, L., Wenbin, K., Shanwen, T. and Chuhong, Z. (2019). Highly concentrated graphene oxide ink for facile 3D printing of supercapacitors. *Nano Materials Science*. 1(2), 142–148.
- Shiraishi, S. (2003). Electric Double Layer Capacitors. *Carbon Alloys*. 447–457.
- Singh, A. P., Tiwari, N. K., Karandikar, P. B. and Dubey, A. (2015). Effect of electrode shape on the parameters of supercapacitor. *2015 International Conference on Industrial Instrumentation and Control (ICIC)*. 669–673.
- Sivaraman, P., Kushwaha, R., Shashidhara, K., Hande, V., Thakur, A., Samui, A. and Khandpekar, M. (2010). All solid supercapacitor based on polyaniline and crosslinked sulfonated poly[ether ether ketone]. *Electrochem Acta*. 55(7), 2451-2456.
- Srinivas, CH., Srinivasu, D., Kavitha, B., Narsimlu, N. and Siva Kumar, K. (2012). Synthesis and Characterization of Nano Size Conducting Polyaniline. *IOSR Journal of Applied Physics*. 1(5), 12-15.
- Tiankuo, C., Soyeon, P. and Kun, Fu. (2021). 3D printing-enabled advanced electrode architecture design. *Carbon Energy*. 3(3), 424-439.

- Toupin, M., Brousse, T. and Bélanger, D. (2004). Charge Storage Mechanism of MnO_2 Electrode used in Aqueous Electrochemical Capacitor. *Chemistry of Materials*. 16(16), 3184–3190.
- Ullah, A., Tashi., Kubo, A. and Harib, K. (2020). Tutorials for Integrating 3D Printing in Engineering Curricula. *Education Sciences*. 10(8), 194.
- Vadiraj, K. T. and Belagali, S. L. (2015). Characterization of Polyaniline for Optical and Electrical Properties, *IOSR Journal of Applied Chemistry*. 8(1), 53-56
- Weerasinghe, W., Vidanapathirana, K. P. and Perera, K. S. (2018). Performance evaluation of polyaniline-based redox capacitors with respect to polymerization current density. *AIMS Energy*. 6(4), 593-606.
- Wang, Z., Zhu, M., Pei, Z., Xue, Q., Li, H., Huang, Y. and Zhi, C. (2020). Polymers for supercapacitors: Boosting the development of the flexible and wearable energy storage. *Materials Science and Engineering: R: Reports*. 139,100520.
- Wu, Z. S., Winter, A., Chen, L., Sun, Y., Turchanin, A., Feng, X. and Mullen, K. (2012). Three-Dimensional Nitrogen and Boron Co-doped Graphene for High-Performance All-Solid-State Supercapacitors. *Advanced Materials*. 24, 5130-5137.
- Xia, X.-H., Tu, J.-P., Wang, X.-L., Gu, C.-D. and Zhao, X.-B. (2011). Mesoporous Co_3O_4 monolayer hollow-sphere array as electrochemical pseudocapacitor material. *Chemical Communications*. 47(20), 5786-5788.
- Yang, M., Hong, S. B. and Choi, B. G. (2015). Hierarchical core/shell structure of $\text{MnO}@$ polyaniline composites grown on carbon fiber paper for application in pseudocapacitors. *Physical Chemistry Chemical Physics*. 17(44), 29874-29879
- Yongbo, C., Sijie, X., Guanjie, L., Shasha, J., Xiangdong, G. and Xiaomin, L. (2019). 3D nanotube-structured $\text{Ni}@$ MnO_2 electrodes: Toward enhanced areal capacitance of planar supercapacitors. *Applied Surface Science*. 494, 29–36.
- Yong, Z., Hui, F., Xingbing, W., Lizhen, W., Aiqin, Z., Tongchi, X., Huichao, D., Xiaofeng, L. and Linsen, Z. (2009). Progress of electrochemical capacitor electrode materials: A review. *International Journal of Hydrogen Energy*. 34(11), 4889–4899.

- Yaseen, M., Humayun., Usman., Shah., Syed S., Shaista., Bakhtiar., Shah., Abbas. and Nasrullah. (2021). A Review of Supercapacitors: Materials Design, Modification, and Applications. *Energies*. 14(22), 7779.
- Yuan, C., Li, J., Hou, L., Lin, J., Pang, G., Zhang, L., Lian, L. and Zhang, X. (2013). Template-engaged synthesis of uniform mesoporous hollow NiCo₂O₄ sub-microspheres towards high-performance electrochemical capacitors. *Royal Society of Chemistry Advances*. 3(40), 18573-18578.
- Yuan, C., Li, J., Hou, L., Zhang, X., Shen, L. and Lou, X. W. D. (2012). Ultrathin Mesoporous NiCo₂O₄ Nanosheets Supported on Ni Foam as Advanced Electrodes for Supercapacitors. *Advanced Functional Materials*. 22(21), 4592-4597.
- Yu, Z., Tetard, L., Zhai, L. and Thomas, J. (2015). Supercapacitor electrode materials: nanostructures from 0 to 3 dimensions. *Energy & Environmental Science*. 8(3), 702–730.
- Zhai, T., Wang, F., Yu, M., Xie, S., Liang, C., Li, C. and Tong, Y. (2013). 3D MnO₂-graphene composites with large areal capacitance for high-performance asymmetric supercapacitors. *Nanoscale*. 5(15), 6790.
- Zhai, T., Lu, X., Wang, H., Wang, G., Mathis, T., Liu, T., Li, C., Tong, Y. and Li, Y. (2015). An Electrochemical Capacitor with Applicable Energy Density of 7.4 Wh/kg at Average Power Density of 3000 W/kg. *Nano Letters*. 15(5), 3189–3194.
- Zhang, X.S. (2009). Carbon-based materials as supercapacitor electrodes, *Chemical Society reviews*. 38, 2520-2531.
- Zhang, L., Huang, D., Hu, N., Yang, C., Li, M., Wei, H., Yang, Z., Su, Y. and Zhang, Y. (2017). Three-dimensional structures of graphene/polyaniline hybrid films constructed by steamed water for high-performance supercapacitors. *Journal of Power Sources*. 342, 1-8.
- Zhu, X., Sun, M., Zhao, R., Li, Y., Zhang, B., Zhang, Y., Lang, X., Zhu, Y. and Jiang, Q. (2020). 3D hierarchical self-supported NiO/Co₃O₄@C/CoS₂ nanocomposites as electrode materials for high-performance supercapacitors. *Nanoscale Advances*. 2, 2785-2791.



APPENDIX

APPENDIX PRESENTATION

List of poster presentations

Hemha, N. and Nuansing, W. (2022). Direct ink write 3D printing of carbon-based materials. **IEEE Magnetic Society Conference 2022 (Thailand Chapter)**. Bangkok, Thailand.

Hemha, N. and Nuansing, W. (2023). The fabrication of 3-dimensional supercapacitor by direct ink write 3D printing of carbon-based materials. **The 4th Materials Research Society of Thailand International Conference (MRS-Thailand 2023)**. Ubon Ratchathani, Thailand.



มหาวิทยาลัยเทคโนโลยีสุรนารี

16-18 November 2022

Session PP-28

Direct ink write 3D printing of carbon-based materials

Niwat Hemha^{1*}, Wiwat Nuansing^{1,2}

¹ School of Physics, Institute of Science Suranaree University of Technology, Thailand

² Center of Excellence on Advanced Functional Materials (CoE-AFM), Suranaree

University of Technology, Thailand

*Email: niwat6842@gmail.com

3D printing is one of additive manufacturing technology. It can create an object using a computer created design and printing of the digital model layer by layer. This allows designing and fabrication of complex objects. This research presents a 3D printing method used for fabrication of a conductive 3D printed object. The method is based on material extrusion and direct ink writing (DIW) techniques. Carbon-based materials such as activated carbon, graphene, and carbon nanotubes were used as active materials. In addition, cellulose acetate (natural fibers) was selected as a binder material. 3D printing inks were mixed between the carbon-based materials and the binder at various ratios. This study reveals an optimized printing condition of the DIW 3D printing. The 3D printed objects were characterized their physical and electrical properties. The results show potentially applications for electrode fabrication in an energy storage device. Moreover, our developed 3D printing method and the optimized printing condition can be applied for constructing magnetic materials.

Keyword: 3D printing, 3D printed electrode, energy storage, Cellulose acetate

S2_P8

The fabrication of 3-dimensional supercapacitor by direct ink write 3D printing of carbon-based materials

Niwat Hemha^{a*}, Wiwat Nuansing^{a,b}

^a School of Physics, Institute of Science Suranaree University of Technology, Thailand

^b Center of Excellence on Advanced Functional Materials (CoE-AFM), Suranaree University of Technology, Thailand

*Corresponding Author's E-mail: niwat6842@gmail.com

3-dimensional (3D) printing is one of additive manufacturing technology. It can create an object using a computer-created design and printing of the digital model layer by layer. This allows the designing and fabrication of complex objects. This research presents the advantage of 3D printing technology and the method for the fabrication of a 3D supercapacitor electrode. The method is based on material extrusion and direct ink writing (DIW) techniques. Carbon-based materials such as activated carbon, graphene, and carbon nanotubes were used as active materials meanwhile cellulose acetate (natural fibers) was selected as a binder material. 3D printing inks were mixed between the carbon-based materials and the binder at various ratios. The study reveals an optimized printing condition of DIW 3D printing. The 3D supercapacitor electrodes were characterized by their physical and electrical properties. 353 μm of diameter printed line and 282 μm of the pore space printed electrode stacked in Z-direction are the advantage of 3D printing technology. The fabrication of 3D supercapacitor by DIW can overcome the limitation of traditional 2-dimensional (2D) supercapacitor electrode by enhancing the active surface area in micro-scale. The results of this work show potential applications for electrode fabrication in an energy storage device. Moreover, our developed 3D printing method and the optimized printing condition can be applied to constructing other energy storage materials.

Keywords: 3D printing, 3D printed electrode, energy storage, Cellulose acetate

CURRICULUM VITAE

Name: Mr. Niwat Hemha
Date of birth: 24th June 1990
Place of birth: Nakhon Phanom, Thailand
Personal address: 53, 10 Kutakai, Plapak, Nakhon Phanom 48160, Thailand
Nationality: Thai
E-mail: niwat6842@gmail.com

Education

2009-2012 B.Sc. in Physics, Mahasarakham University,
Mahasarakham, Thailand

2012 – 2017 M.Sc. in Physics, Suranaree University of Technology,
Nakhon Ratchasima, Thailand

2017 – Present Currently enrolling in Ph.D. majoring in Physics, School of
Physics, Institute of Science, Suranaree University of
Technology, Nakhon Ratchasima, Thailand

มหาวิทยาลัยเทคโนโลยีสุรนารี